ADVERTIMENT. La consulta d’aquesta tesi queda condicionada a l’acceptació de les següents condicions d'ús: La difusió d’aquesta tesi per mitjà del servei TDX (www.tesisenxarxa.net) ha estat autoritzada pels titulars dels drets de propietat intel·lectual únicament per a usos privats emmarcats en activitats d’investigació i docència. No s’autoritza la seva reproducció amb finalitats de lucre ni la seva difusió i posada a disposició des d’un lloc aliè al servei TDX. No s’autoritza la presentació del seu contingut en una finestra o marc aliè a TDX (framing). Aquesta reserva de drets afecta tant al resum de presentació de la tesi com als seus continguts. En la utilització o cita de parts de la tesi és obligat indicar el nom de la persona autora.

ADVERTENCIA. La consulta de esta tesis queda condicionada a la aceptación de las siguientes condiciones de uso: La difusión de esta tesis por medio del servicio TDR (www.tesisenred.net) ha sido autorizada por los titulares de los derechos de propiedad intelectual únicamente para usos privados enmarcados en actividades de investigación y docencia. No se autoriza su reproducción con finalidades de lucro ni su difusión y puesta a disposición desde un sitio ajeno al servicio TDR. No se autoriza la presentación de su contenido en una ventana o marco ajeno a TDR (framing). Esta reserva de derechos afecta tanto al resumen de presentación de la tesis como a sus contenidos. En la utilización o cita de partes de la tesis es obligado indicar el nombre de la persona autora.

WARNING. On having consulted this thesis you’re accepting the following use conditions: Spreading this thesis by the TDX (www.tesisenxarxa.net) service has been authorized by the titular of the intellectual property rights only for private uses placed in investigation and teaching activities. Reproduction with lucrative aims is not authorized neither its spreading and availability from a site foreign to the TDX service. Introducing its content in a window or frame foreign to the TDX service is not authorized (framing). This rights affect to the presentation summary of the thesis as well as to its contents. In the using or citation of parts of the thesis it’s obliged to indicate the name of the author

VALIDATION AND GENERATION OF CURVED MESHES FOR HIGH-ORDER UNSTRUCTURED METHODS

Abel Gargallo-Peiró

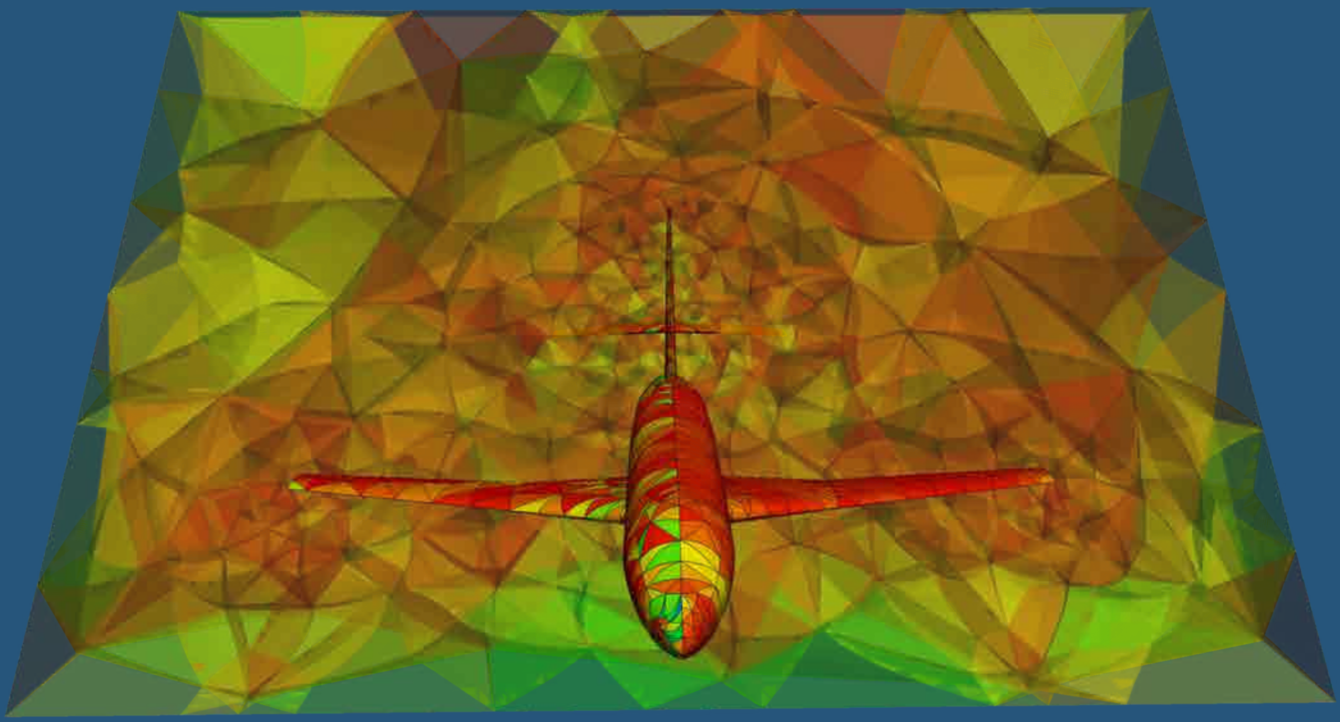

Doctoral Thesis
Barcelona, May 2014

VALIDATION AND GENERATION OF CURVED MESHES FOR HIGH-ORDER UNSTRUCTURED METHODS

Abel Gargallo-Peiró

UPC

Doctoral Thesis
Advisors: Xevi Roca and Josep Sarrate
Barcelona, May 2014

Departament de Matemàtica Aplicada III
Programa de Doctorat de Matemàtica Aplicada

A la familia que m'ha vist créixer,
i a la que haig de veure créixer jo.

ABSTRACT

Generation of curved meshes for high-order unstructured methods

Abel Gargallo-Peiró

In this thesis, a new framework to validate and generate curved high-order meshes for complex models is proposed. The main application of the proposed framework is to generate curved meshes that are suitable to perform finite element analysis with unstructured high-order methods. Note that the lack of a robust and automatic curved mesh generator is one of the main issues that has hampered the adoption of high-order methods in industry. Specifically, without curved high-order meshes composed by valid elements and that match the domain boundary, the convergence rates and accuracy of high-order methods cannot be realized. The main motivation of this work is to propose a framework to address this issue.

First, we propose a definition of distortion (quality) measure for curved meshes of any polynomial degree. The presented measures allow validating if a high-order mesh is suitable to perform finite element analysis with an unstructured high-order method. In particular, given a high-order element, the measures assign zero quality if the element is invalid, and one if the element corresponds to the selected ideal configuration (desired shape and nodal distribution). Moreover, we prove that if the quality of an element is not zero, the region where the determinant of the Jacobian is not positive has measure zero. We present several examples to illustrate that the proposed measures can be used to validate high-order isotropic and boundary layer meshes.

Second, we develop a smoothing and untangling procedure to improve the quality for curved high-order meshes. Specifically, we propose a global non-linear least squares minimization of the defined distortion measures. The distortion is regularized to allow untangling invalid meshes, and it ensures that if the initial configuration is valid, it never becomes invalid. Moreover, the optimization procedure preserves, whenever is possible, some geometrical features of the linear mesh such as the shape, stretching, straight-sided edges, and element size. We demonstrate through examples that the implementation of the optimization problem is robust and capable of handling situations in which the mesh before optimization contains a large number of invalid elements. We consider cases with polynomial approximations up to degree

ten, large deformations of the curved boundaries, concave boundaries, and highly stretched boundary layer elements.

Third, we extend the definition of distortion and quality measures to curved high-order meshes with the nodes on parameterized surfaces. Using this definition, we also propose a smoothing and untangling procedure for meshes on CAD surfaces. This procedure is posed in terms of parametric coordinates of the mesh nodes to enforce that the nodes are on the CAD geometry. In addition, we prove that the procedure is independent of the surface parameterization. Thus, it can optimize meshes on CAD surfaces defined by low-quality parameterizations.

Finally, we propose a new mesh generation procedure by means of an *a posteriori* approach. The approach consists of modifying an initial linear mesh by first, introducing high-order nodes, second, displacing the boundary nodes to ensure that they are on the CAD surface, and third, smoothing and untangling the resulting mesh to produce a valid curved high-order mesh. To conclude, we include several examples to demonstrate that the generated meshes are suitable to perform finite element analysis with unstructured high-order methods.

ACKNOWLEDGMENTS

This thesis has been erected using the bricks that so many people have kindly given to me.

First, I want to thank Pep for being a father as well as a director. Second, this thesis would not have been the same without Xevi. Although he had to move to Boston, he never left this thesis and he did always put all his energy to help me. I am the hand that drew the lines between the points that they showed to me. I have enjoyed this thesis, and all the time expended with both of you.

I also want to thank to Antonio Huerta, director of LaCàN, since many things are possible due to his long-term work and enthusiam. Together with him, I express my gratitude to Jaime Peraire for accepting me at AeroAstro at MIT and for his feedback in our research.

Among many other people, I need to thank to Eloi. You have thaught me a lot of things, and not all of them where new cool books.

Moreover, I feel really fortunate to have developed the thesis in LaCàN. I must thank to all the professors, researchers and support staff. Each person has taught me something in this journey. And with everyone's sand grains, we have created a nice environment to work in and we have sweetened life with all the fantastic cakes that we've cooked.

The thesis drove me to Boston for about 8 months, and I have to say that the time at MIT could not have been more profitable. Academically, I enriched myself, being able to breath the air of a different university, to talk with new researchers, to attend to different seminars... but it was not only an academic experience. During that time I had a nice vital experience, being able to meet a different country, a different city, and a lot of different people. I must thank all the new friends. I had a great time with you.

I also need to thank all the people that has influenced me to be here during all my academic and personal live. Teachers that I loved from school (Sant Miquel Arcàngel i Salesians Sarrià) have defined the basis of what I know. Professors from UPC that are not related to my PhD, but that where important to me. Old friends, and new friends. I do not write the names, but I know all of them.

And my family. My grandparents and my parents. They have all taught me about life. I owe them everything. My brother too, he beat me in this race and has become a doctor before me. He is my best friend, and I am proud of having him in my life.

Maite. I can just thank you to accept and support me unconditionally. You have taught me how to live and enjoy my life, and I enjoy it next to you.

I also need to thank Aimar. Finishing this thesis holding him in my arms has sweetened each review.

Thanks to you all.

Abel Gargallo-Peiró
Barcelona, May 2014

Contents

List of Figures

Chapter 1

Introduction

1.1 Motivation

During the last two decades, unstructured high-order methods (Szabo and Babuška, 1991; Schwab, 1998; Deville et al., 2002; Hesthaven and Warburton, 2007; Karniadakis and Sherwin, 2013) have experimented a remarkable attention from the computational methods community. One of the main features that attracted the attention to high-order methods is that if the exact solution of a *partial differential equation* (PDE) is smooth and without singularities in the domain, then the approximation obtained with a high-order method converges exponentially with the order of the approximating polynomial (Babuška et al., 1981; Szabo and Babuška, 1991). Therefore, it has been possible to show that high-order methods provide higher accuracy with lower computational cost than low-order methods in a wide range of applications (Vos et al., 2010; Cantwell et al., 2011b,a; Löhner, 2011; Yano et al., 2012; Kirby et al., 2012; Huerta et al., 2012, 2013; Löhner, 2013; Wang et al., 2013).

It is important to highlight that an implicit assumption so that the convergence rate for high-order methods is realized is that the geometry is also represented with high-order accuracy. Therefore, the boundary faces have to be curved to match the domain boundaries with the accuracy determined by the order of the solution approximation. To this end, element-wise polynomials of the same degree as the approximating polynomial (*iso-parametric*) can be also used to represent the curved elements. In this manner, the integrals on the control volumes are performed on elements that approximate the curved domain boundaries with the appropriate accuracy. Furthermore, it has been evidenced that curved elements allow reducing the spurious artifacts in the PDE solution approximation that arise in specific applications due to a linear approximation of the domain boundary (Bassi and Rebay, 1997; Barth, 1998; Dey et al., 1997; Luo et al., 2002; Xue and Demkowicz, 2005; Sevilla et al., 2011).

Despite the huge interest in the combination of unstructured high-order methods with curved meshes, two main issues have slowed down their adoption in industrial applications. First, the difficulty of developing high-order solvers that can compete with the robustness and simplicity of consolidated first-order and second-order industrial solvers. Second, the unavailability of industrial curved high-order mesh generators to provide, in a reliable and automatic manner, valid meshes that match the curved boundaries of a complex *computer-aided design* (CAD) model. Therefore, special attention has to be focused on developing automatic algorithms to generate curved high-order meshes.

The challenge in developing and implementing a robust and automatic curved high-order mesh generator arises from the requirements imposed by the unstructured high-order solver. Specifically, a curved high-order mesh is *valid* to perform finite element analysis with an unstructured high-order solver if:

i) Each physical element is the image of a regular straight-sided high-order master element. The mapping between the two elements must be differentiable, invertible and smooth (*diffeomorphism*), in order to allow the change of variables required to perform the control volume (area) integrals that appear in the formulation of 3D (2D) unstructured high-order methods.

ii) The mesh is curved close to the boundary in order to match the geometry and approximate it with high-order accuracy. In particular, we want a curved mesh in order to ensure that the error introduced in the solution by the inexact approximation of the geometry is smaller than the solution discretization error. Moreover, without a curved mesh that matches the boundary geometry, the properties from which high-order methods benefit cannot be realized.

iii) Each physical element has a shape close to a regular ideal configuration. In particular, if we define a mapping between the ideal element configuration and the physical configuration, the resulting mapping must have a smooth and well-conditioned Jacobian. If the Jacobian is ill-conditioned, the approximation accuracy is degraded and the solution may be polluted by the introduced error (Shewchuk, 2002).

iv) Each physical element has an adequate nodal high-order distribution inherited from the master element. Otherwise, since it is required to map the physical to the master element, the mapping between both elements will not be smooth or even valid. For instance, it is standard to use a point distribution that provides a quasi-optimal Lebesgue constant (Warburton, 2006; Hesthaven and Warburton, 2007).

1.2 Scope

The scope of this thesis is to generate valid unstructured curved high-order meshes for complex geometries. To this end, several initial decisions for the used approaches were considered. In this section, we describe and detail the reasoning behind this initial decisions. First, we assume that the complex geometry to discretize is represented by a CAD model. Moreover, we choose a hierarchical approach to generate conformal 3D (2D) curved high-order meshes by generating first the corresponding surface (curve) meshes. Finally, we focus on the generation of unstructured meshes by means of an indirect method (*a posteriori*) that curves an initial unstructured simplicial linear mesh to match the curved domain boundary.

1.2.1 Geometry representation: CAD model

In order to generate a mesh, first it is necessary to have a proper representation of the target geometry to discretize. We highlight that several geometry representations can be used:

- Triangular mesh. The boundary of the target volume is defined as a piece-wise linear approximation of the boundary surface.

- Implicit boundary. The surfaces (curves) that conform the boundary of the target 3D (2D) geometry are described by means of the union and intersection of implicit equations in terms of the physical coordinates of the points.

- CAD model. The 3D (2D) geometry is described in terms of vertices, parameterized curves, and parameterized surfaces that determine the boundary of the target volumes (surfaces).

Among the different existing representation techniques, in this thesis we focus on the generation of high-order meshes from CAD models. We do not consider geometries determined by a triangular mesh since it would limit the accuracy of the geometry representation to that of a piece-wise linear approximation and therefore, it would not be suitable for high-order methods. We discard implicit boundary representations since they are rarely used in industrial applications. On the contrary, CAD models are the preferred geometry representation in the design, analysis, and manufacturing stages of an industrial application.

In addition, CAD models provide some specific advantages for curved mesh generation. For instance, they facilitate the generation of high-order nodes that lie on the surfaces (curves) that limit the original 3D (2D) model. That is, in a CAD 3D (2D) model the surfaces (curves) are parameterized and therefore, the distribution of the high-order nodes can be obtained on the parameter space. Then, the nodes on the surfaces (curves) of the 3D (2D) model are obtained by using the available surface (curve) parameterization.

1.2.2 Strategy: hierarchical mesh generation

It is required that a mesh generation algorithm generates volume elements that are conformal with the surfaces, curves, and vertices that compose the domain boundary. According to the dimensional order in which the volume (3D) elements are accommodated to the surfaces (2D), curves (1D), and vertices (0D) of the domain there are two main mesh generation approaches:

- Top-down: creates a volume (surface) mesh first, and the surface, edge, and vertex meshes are extracted from the volume (surface) mesh boundary and accommodated to approximate the boundary of the initial 3D (2D) geometry representation.

- Bottom-up (*hierarchical*): first, for each vertex (0D) of the geometry a mesh point is generated. Second, each curve (1D) is meshed with segment elements that are bounded at the extremes by the vertex points (0D). Third, each surface

> (2D) is meshed with polygonal elements (*e.g.* triangles, quadrilaterals) that are bounded by the wire meshes (1D) that correspond to the boundary curves. Finally, each volume is meshed with polyhedral elements (*e.g.* tetrahedral, hexahedra) that are bounded by the shell meshes (2D) that correspond to the boundary surfaces.

In this thesis, we select a hierarchical approach in order to generate curved high-order meshes. The main reason is that hierarchical approaches, when compared with top-down approaches, generate discretizations of higher quality of the 3D (2D) domain boundary surfaces (curves). Recall that the quality of the boundary mesh is important since it is required that a curved high-order mesh reproduces the domain boundaries with the proper accuracy.

Moreover, the hierarchical approach simplifies the generation of conformal meshes for 3D (2D) assembly models. That is, meshes where adjacent 3D (2D) elements fully share either a face, an edge or a vertex. To obtain conformal meshes between adjacent volumes (surfaces) it is only needed to share the previously generate mesh on the boundary surfaces (curves). Note that in this thesis we focus on the generation of conformal meshes, since they can be used with both conformal and non-conformal solvers.

1.2.3 Method approach: *a posteriori* curved mesh generation

In this thesis, we have decided to pursue the development of an indirect method for curved mesh generation. That is, instead of considering generating directly curved high-order elements of a specific type, we have decided to curve an existent initial unstructured linear mesh (*a posteriori*). In this manner, the initial mesh can be composed by either tetrahedral (triangular) or hexahedral (quadrilateral) elements generated with any established 3D (2D) linear mesh generation procedure that provides control over the size and shape of the elements. Then, the *a posteriori* algorithm is only responsible to curve the elements to match the domain boundary while ensuring that the high-order elements are valid.

Several steps compose standard *a posteriori* approaches for curved mesh generation (Dey et al., 1997, 2001a; Luo et al., 2002, 2004; Shephard et al., 2005; Sherwin and Peiró, 2002; Persson and Peraire, 2009; Xie et al., 2012; Toulorge et al., 2013).

First, using an established linear mesh generator we obtain a linear mesh with the desired element size and shape. Second, the polynomial degree of the mesh is increased and the mesh is curved to match the geometry. In this step, tangled elements arise due to the intersection between the adjacent edges of an element. In particular, the determinant of the Jacobian of the element representation can vanish or become negative, invalidating the use of the mesh in a numerical simulation. Hence, it is necessary a final step to correct the inverted elements and generate a mesh composed by valid elements. In order to obtain a final valid mesh, different strategies can be followed. For instance, if the initial topology cannot accommodate the curved faces, the topology can be modified (Dey et al., 2001a; Luo et al., 2002, 2004). Alternatively, the nodes can be relocated in order to obtain a valid configuration (Sherwin and Peiró, 2002; Persson and Peraire, 2009; Xie et al., 2012; Toulorge et al., 2013). In this thesis, we assume that the linear mesher provides a mesh that has the topology necessary to reproduce the geometry. Therefore, we focus on developing a procedure to curve the high-order mesh to match the geometry and to relocate the nodes to ensure a valid final configuration.

1.2.4 Unstructured simplicial meshes

The application of the unstructured high-order methods in 3D simulations requires using meshes composed by polyhedral elements. In these applications the most common types are the tetrahedral (four triangular faces) and hexahedral (six quadrilateral faces) elements. Fast and robust approaches have been developed to automatically generate tetrahedral meshes for arbitrary domains: the advancing front technique (Löhner et al., 1985; Peraire et al., 1987, 1988; Löhner and Parikh, 1988), Delaunay based methods (Baker, 1987; George et al., 1988), and the Octree approach (Shephard and Georges, 1991; Yerry and Shephard, 1984). On the contrary, only a limited type of geometries can be automatically meshed with high-quality hexahedral meshes. According to it, in this thesis we focus on the generation of unstructured tetrahedral (triangular) meshes to exploit the potential geometrical flexibility (arbitrary domains) provided by 3D (2D) unstructured high-order methods.

As said, we are not focused in the generation of hexahedral (quadrilateral) meshes for 3D (2D) domains. Nevertheless, all the methods of this thesis have also been checked for hexahedral (quadrilateral) meshes, see Appendix D. Note that this has been possible since the proposed curved mesh generation algorithm is based on an *a* *posteriori* approach.

1.3 Goals and layout of this thesis

Although the extensive development of high-order methods, the generation of curved high-order meshes is still not automatic. In particular, the lack of a robust and generic procedure to generate curved high-order meshes that match the boundary geometry has hampered the adoption of unstructured high-order methods in industry.

The main goal of this thesis is to address this issue by proposing a new method to validate and generate unstructured curved high-order meshes of any polynomial degree from CAD geometries. To this end, we have considered the following intermediate goals:

- **Validation of curved high-order planar and volumetric meshes.** In order to use a high-order element in a numerical computation, it must be the image of a valid straight-sided master element through an element-wise invertible mapping. Moreover, the size and shape of the element must be close to an ideal configuration. Hence, to ensure that a mesh is suitable for performing finite element analysis with an unstructured high-order method, it is required to develop a technique to validate curved high-order elements.

  In Chapter 3, we focus on the development of a technique to quantify the distortion (quality) of a high-order mesh composed by curved elements. We pose the measures for high-order elements in terms of the Jacobian-based distortion measures for linear elements. The defined measures are valid for elements of any polynomial degree. The quality measure assigns zero value to an invalid high-order element, and value one if the element is ideal (has the desired shape and node distribution). Specifically, we prove that if the quality of an element is greater than zero, the region where the determinant is not positive has measure zero. Hence, they allow checking the validity of a high-order element for simulations performed with unstructured high-order methods. Moreover, we prove that the defined measures inherit the affine invariance properties of the Jacobian-based distortion (quality) measures for linear elements. Finally, we illustrate the behavior of the defined measures, and their applicability to determine the validity of isotropic and boundary layer meshes.

- **Optimization of a regularized distortion measure to smooth and untangle curved high-order planar and volumetric meshes.** To generate high-order meshes by means of an *a posteriori* approach, it is necessary to develop a technique to curve the inner elements of the mesh. The method has to fix the inversions and foldings that arise when the boundary faces of the mesh are curved to match the boundary geometry.

  In Chapter 4, we use the proposed point-wise distortion measure for high-order meshes to develop a robust smoothing and untangling algorithm to curve a given straight-sided high-order mesh. The method is able to repair and improve the quality of a given curved high-order mesh even when a high number of non-valid elements is present. Specifically, we propose a global non-linear least-squares minimization of a regularized measure of the mesh distortion. The proposed algorithm is able to:

  - repair invalid curved meshes (untangling),
  - ensure that initially valid configurations remain valid after transformation (consistency),
  - deal with arbitrary polynomial degrees (high-order), and
  - preserve some geometrical features of the initial linear mesh (size, stretching, straight-sided interior elements).

  We highlight that the unknowns of the optimization procedure are the coordinates of the interior mesh nodes. If the surface mesh is invalid or presents low-quality elements, we use the procedure presented in Chapter 5 to optimize the nodes on the exact CAD geometry and to obtain a valid curved high-order surface mesh.

- **Validation and generation of curved high-order meshes on CAD surfaces.** The meshes obtained with the curving methods have to be composed by valid high-order elements that approximate the curved boundaries of the initial CAD model. In this manner, the exponential convergence rates of high-order methods can be realized. In addition, the quality of a volume mesh is limited by the quality of the surface mesh. Note that if a boundary face is invalid, the adjacent 3D element will as well be invalid.

In Chapter 5, we present a technique to extend Jacobian-based distortion (quality) measures for planar linear elements to high-order elements of any polynomial degree with the nodes on the parameterized CAD surfaces. The resulting distortion (quality) measures are expressed in terms of the parametric coordinates of the nodes. These extended distortion (quality) measures can be used to check the quality and validity of a high-order surface mesh.

Moreover, we derive a simultaneous smoothing and untangling procedure for high-order surface meshes. This procedure is formulated as a non-linear least-squares minimization of the extended distortion measure. The minimization is performed in terms of the parametric coordinates of the nodes and therefore, the nodes always lie on the CAD surface. Moreover, we prove that both the defined distortion measure and the derived optimization procedure are independent of the surface parameterization. Hence, the proposed technique is well suited to optimize meshes on CAD geometries with low-quality parameterizations.

Finally, we derive an *a posteriori* approach to generate high-order meshes on CAD geometries. In particular, given a linear mesh on a parameterized surface, we increase the polynomial order of the elements on the parametric space and we use the proposed smoothing and untangling algorithm to obtain a valid and high-quality mesh on the physical space.

- **Curved mesh generation for high-order unstructured methods.** The ultimate goal of the techniques developed in this thesis is the generation of curved meshes suitable for finite element analysis with unstructured high-order methods. In a high-order simulation, it is mandatory that the boundary elements are curved to match the geometry. Without curved meshes that approximate the CAD geometry, the high-order accuracy cannot be fulfilled and the properties from which high-order methods benefit are lost.

  On the one hand, in Chapter 6, we detail a new *a posteriori* approach for generating curved high-order conformal meshes for CAD models. The main purpose of the generated meshes is to perform finite element analysis with any solver based on an unstructured high-order method. Therefore, it is required that the generated high-order mesh is composed of valid elements that are curved to approximate the boundaries of the domain. The proposed *a posteriori* approach to generate curved high-order meshes is composed of several steps.

First, we generate a linear mesh. Second, we increase the polynomial degree of the mesh and we curve it to match the boundary geometry. Note that this mesh can contain inverted elements in the curved boundary. Hence, the last step is to optimize the curved mesh using the smoothing and untangling procedure presented in Chapter 4.

On the other hand, we illustrate several applications where the high-order curved meshes generated with the proposed procedure have been used. We point out that we have validated that the meshes can be used in 2D and 3D applications, and for different problems: wave propagation, inviscid flow, and viscous flow simulations. We focus on three main computations:

1. *Generation of a triangular mesh of polynomial degree seven of the Barcelona harbor.* In Section 6.3.1, we generate a valid curved mesh of polynomial degree seven of the Barcelona harbor. The main application of this mesh is to solve a wave propagation problem in highly reflective coastal areas. We highlight that, for this simulation, having a high-order mesh is essential in order to reduce the dispersion error and obtain, and to capture small curved features of the geometry relevant to the computation.

2. *Generation of a tetrahedral mesh of polynomial degree four on the exterior domain of a Falcon aircraft.* In Section 6.3.2, we generate a mesh on the exterior domain of a Falcon aircraft to perform an inviscid flow computation. In order to fulfill the simulation requirements and obtain a reliable computation, it is necessary to generate a mesh of polynomial degree four that approximates with the desired precision the curved features of the geometry. We point out that to reach an steady state high-order solution of the Euler equations it is mandatory to have a curved high-order mesh that matches the boundary geometry.

   In Section 6.3.2.1, we describe the mesh generation process and we analyze the validity of the generated mesh. Finally, in Section 6.3.2.2 we illustrate the simulation computed with the generated mesh.

3. *Generation of boundary layer tetrahedral meshes for exterior domain viscous flow computations.* In Section 6.3.3, we present a method to convert an inviscid mesh into a viscous mesh with the desired boundary layer around the target CAD geometry. Starting from an inviscid mesh of the

desired polynomial degree, we propose a template to generate the desired boundary layer. Specifically, we extrude the mesh faces adjacent to the geometry, and we generate elements with the stretching specified by the user. Next, we use the optimization procedure proposed in Chapter 4 to ensure that the final mesh is valid. The obtained meshes are conformal and fully composed by tetrahedra. Hence, they can be used with any continuous and discontinuous Galerkin solver that features tetrahedral elements. To validate the proposed method, we illustrate a solution for the compressible Navier-Stokes equations for the steady-state flow around a sphere.

Chapter 2

State of the Art

In this chapter, we review the state of the art of the existent methods and strategies to generate high-order meshes. We consider three groups of references, that correspond to the main chapters of this thesis. First, in Section 2.1 we present the previous works devoted to validate high-order meshes. Next, in Section 2.2 we present an overview of the algorithms that have been developed to generate planar and volumetric high-order meshes. Finally, in Section 2.3 we review the techniques previously developed to validate and generate curved meshes on surfaces.

2.1 Validation of planar and volumetric high-order meshes

One of the main issues in mesh generation is to quantify the validity of a mesh for computational purposes. For linear elements, a wide range of quality measures have been developed (Field, 2000; Shewchuk, 2002). One of the most extended families of quality measures for linear elements are algebraic quality measures introduced in Knupp (2001a, 2003a). These measures allow determining the quality (distortion) of a linear element in terms of an affine mapping between an ideal element and the physical one. Specifically, the Jacobian matrix of this mapping is used to measure the deviation of the physical element with respect to the ideal one (distortion). Therefore, the value of the quality (distortion) measures is determined by the physical coordinates of the element vertices. However, this is an unresolved issue for high-order meshes. To address this issue, in this thesis we develop a technique that allows extending to high-order elements the set of Jacobian-based measures for linear elements presented in Knupp (2001a, 2003a). Below we review the previous developed approaches to quantify the validity and quality of curved meshes.

On the one hand, different techniques have been proposed to determine the validity of a high-order mesh by means of checking the positivity of the Jacobian mapping from the master to the physical element. Specifically, it has been studied how to detect non-positive Jacobian determinants for B-spline based mappings (Dey et al., 1997, 2001a; Luo et al., 2002, 2004; Shephard et al., 2005) and quadratic iso-parametric elements (Mitchell et al., 1971; Field, 1983; Baart and Mulder, 1987). Moreover, for higher polynomial degrees, Johnen et al. (2012, 2013) proposed to compute accurate bounds on Jacobian determinants of 2D and 3D curvilinear polynomial finite elements.

On the other hand, several approaches have been developed to quantify the quality of non-linear iso-parametric elements. For elements of quadratic degree, different definitions of distortion (quality) have been proposed for planar (Salem et al., 1997, 2001; Yuan et al., 1994; Knupp, 2009) and volumetric (Branets and Carey, 2005; Salem et al., 2001; George and Borouchaki, 2012) elements. We would like to highlight that we share a similar formulation to the one proposed by Branets and Carey (2005). However, their work is devoted to extending a particular distortion measure to quadratic elements, while our goal is to formulate a technique to extend any Jacobian based distortion measure to any polynomial degree. A different approach to extend Jacobian based disortion measures was previously proposed by Knupp (2009). The main difference is that we propose to integrate the distortion measure on the curved element, instead of computing the minimum, maximum or the mean on a set of sampling points. In addition, we also present numerical tests and mesh optimizations beyond the quadratic case. The main feature of the distortion and quality measures defined in this work (Roca et al., 2012; Gargallo-Peiró et al., 2014a) is that we propose the definition for elements of any polynomial degree. The proposed distortion is the $\mathcal{L}^2$-norm of the regularization of a given point-wise Jacobian-based measure. This definition allows detecting non-positive values of the Jacobian determinant of the master mapping for any polynomial degree. That is, if the quality is greater than zero, the master mapping is a local diffeomorphism on the integration points.

2.2 Generation of planar and volumetric high-order meshes

In this section, we present the previous works to generate and optimize high-order meshes. First, we review the main works on generation by an *a posteriori* procedure of an initial linear mesh. Second, we present the main approaches to curve high-order meshes and ensure that the resulting mesh is valid and matches the boundary geometry.

2.2.1 Generation by an *a posteriori* approach

The standard approach to generate curved meshes is to use an *a posteriori* procedure (Dey et al., 1997, 2001a; Luo et al., 2002, 2004; Luo, 2005; Shephard et al., 2005; Sherwin and Peiró, 2002; Persson and Peraire, 2009; Xie et al., 2012; Toulorge et al., 2013). The main idea is to modify an initial unstructured linear mesh to obtain a high-order mesh composed by curved elements that approximate the domain boundaries. These *a posteriori* procedures can be divided in three main groups depending on the technique used to curve the mesh and match the domain boundary. The first group of methods refine, coarsen, and deform the elements, according to a set of heuristics, until a final valid mesh is properly adapted to the curved features of the geometry (Dey et al., 2001a; Luo et al., 2002, 2004; Luo, 2005; Sherwin and Peiró, 2002). The second group of methods use a high-order continuous Galerkin method to solve a Lagrangian solid mechanics analogy of the curving meshing problem. Specifically, the mesh curving has been formulated as a non-linear elasticity problem (Persson and Peraire, 2009) and as a linear elasticity problem (Nielsen and Anderson, 2002; Oliver, 2008; Xie et al., 2012). In this group of methods, the initial solid configuration corresponds to mesh composed by straight-sided elements. Then, the final configuration is obtained by imposing the displacements that correspond to the curved domain boundaries and solving the corresponding Lagrangian solid mechanics problem. The final group of methods optimize the node location of the nodes according to a goal function that enforces that the obtained elements are properly curved (George and Borouchaki, 2012; Roca et al., 2012; Gargallo-Peiró et al., 2013a; Remacle et al., 2013; Toulorge et al., 2013; Gargallo-Peiró et al., 2014a).

The main challenge of any *a posteriori* mesh curving method is to repair those invalid or low-quality elements that can arise from curving the boundary of the initial straight-sided mesh. Specifically, to repair those elements that have straight faces that intersect the new curved faces. Once the invalid or low-quality elements have been detected, it is required to repair them by means of topological and node relocation techniques. Note that topological modifications are not enough to repair those elements that have been detected to be invalid. To address this issue, it is required to relocate the inner high-order nodes (smoothing) while the nodes on the curved boundary remain fixed. This smoothing capability is required by the three groups of curved meshing methods. Note that this work corresponds to the third group, since we relocate the coordinates of the inner nodes by means of an optimization-based approach.

2.2.2 Curving high-order meshes

In order to curve a high-order mesh in the *a posteriori* process and obtain a valid mesh is necessary to relocate the high-order nodes. A node relocation technique can be formulated in two distinct manners. On the one hand, it can be formulated as a single problem where the unknowns are the coordinates of all the inner nodes (global formulation). On the other hand, several problems can be formulated where the unknowns are just one or few inner nodes (local formulation). The main benefit of a global formulation is that the number of iterations to solve the problem is smaller than for a local formulation. However, local formulations require less computational and memory resources at each iteration. Note that all the curving methods that use a Lagrangian solid mechanics analogy correspond to a global formulation (Persson and Peraire, 2009; Xie et al., 2012). On the contrary, optimization-based methods have been formulated globally (a single objective function) or locally (one objective function for each single node). For instance, for linear elements there exist several local (Freitag and Plassmann, 2000; Freitag and Knupp, 2002; Escobar et al., 2003) and global (Jiao et al., 2011; Knupp, 2001b, 2003b; López et al., 2008; Garimella et al., 2004; Sastry et al., 2012b; Gargallo-Peiró et al., 2014) approaches. For high-order meshes, similar relocation methods have also been derived. On the one hand, in Roca et al. (2012) we presented local method to optimize high-order meshes. On the other hand, several methods to optimize the high-order nodes location according to a global objective function have been proposed (George and Borouchaki, 2012; Gargallo-Peiró et al., 2013a; Remacle et al., 2013; Toulorge et al., 2013; Gargallo-Peiró et al., 2014a). Note that stating a global formulation allows to choose if the implementation is global or local. Therefore, if necessary, the implementation of a global formulation can be benefited from the advantages of a local formulation. For instance, coloring for parallelization, optimizing localized sets of nodes, and dealing with large meshes with a reduced memory footprint. Specifically, a global method can be casted to a local implementation by using a non-linear Gauss-Seidel solver, as we proposed in Gargallo-Peiró et al. (2014). In this work, we detail this local implementation to optimize high-order meshes, see in Appendix B.

One important requirement, is that the node relocation technique penalizes the appearance of invalid elements. In this manner, the method can enforce that once all the mesh elements are valid, they remain valid (consistency). This is of major importance to ensure valid meshes in applications where the domain presents non-convex boundaries, and when large deformations of the domain boundaries are performed during the simulation. Several works have addressed explicitly this issue for linear (Escobar et al., 2003; Gargallo-Peiró et al., 2014; Sastry et al., 2012a) and for high-order (Persson and Peraire, 2009; Roca et al., 2012; Remacle et al., 2013; Toulorge et al., 2013; Gargallo-Peiró et al., 2013a, 2014a) elements. In all the cases, this guarantee is given by a non-linearity that creates vertical asymptotes in the limit of the feasible region (null determinant). These asymptotes ensure that if the nodes are in the feasible region (positive determinant), they cannot be driven to an invalid configuration (zero or negative determinant). However, at the same time, these asymptotes prevent these techniques to repair the invalid elements (untangle).

Optimization procedures are specially suited to overcome the described drawbacks. Among the reviewed optimization formulations, there are two consistent untangling techniques specialized in curving high-order meshes. On the one hand, a technique to define a regularized distortion and quality measure for high-order planar and surface elements applied to generate curved meshes is proposed in Roca et al. (2012) and Gargallo-Peiró et al. (2013a). This technique is based on the extension to high-order elements of the definition of quality and distortion measure for linear elements presented in Knupp (2001a, 2003a). The optimized distortion features a non-linearity that creates a vertical asymptote that prevent feasible configurations to become unfeasible (consistency). Moreover, it is regularized to enforce that unfeasible configurations (tangled) become valid (untangle). Specifically, the regularization of the reciprocal of the determinant presented in Escobar et al. (2003) and Gargallo-Peiró et al. (2014) is used in order to allow untangling inverted elements. On the other hand, in Remacle et al. (2013) and Toulorge et al. (2013) it is proposed to optimize a function that penalizes small values of the Jacobian determinants based on the parameter-dependent log-barrier method presented in Sastry et al. (2012a).

Note that both untangling techniques presented in Escobar et al. (2003) and Sastry et al. (2012a) for linear elements depend on a parameter that needs to be determined. In this work, we propose to unequivocally determine the value of the untangling parameter, originally presented in Escobar et al. (2003), in an element-wise manner from the ideal mesh configuration. Therefore, the element-wise untangling parameter remains constant during the untangling process and the derivatives of the objective function do not depend on its value. When a valid configuration is obtained, we set this element-wise parameter to zero. According to the discussion above, here we present a global node relocation technique based on the minimization of non-linear and regularized distortion measure that untangles in a consistent manner curved and high-order meshes. The technique proposed in this work to generate high-order meshes is presented in Roca et al. (2012) for planar triangle meshes and in Gargallo-Peiró et al. (2014a) for tetrahedral meshes.

2.3 Validation and generation of high-order meshes on surfaces

In this section, we present the framework of generation and optimization of high-order meshes on surfaces. Note that to generate high-order meshes by an *a posteriori* process it is required to relocate the nodes to curve the mesh to fit the geometry. However, special attention must be focused on the surface case, since the nodes of the mesh need to be constrained to ensure that they lie on the exact geometry. Hence, we divide this section in two parts. First, we review a wide range of techniques on the optimization of linear meshes on surfaces. Second, we focus on the specific existing works to generate surface high-order meshes.

2.3.1 Optimization of linear meshes on surfaces

Several relocation techniques for surface linear meshes have been previously developed. These techniques can be classified into two groups, depending on whether the nodes are relocated indirectly or directly on a surface representation. On the one hand, indirect relocation methods compute an ideal location of the nodes. However, the resulting node locations can be off the surface. Therefore, an additional step to relocate the nodes on, or close to, the surface is required (Escobar et al., 2006, 2011; Frey and Borouchaki, 1998; Jiao et al., 2011; Vartziotis et al., 2008; Zhang et al., 2009; Leng et al., 2012). In particular, Escobar et al. (2006, 2011) present a simultaneous untangling and smoothing method for triangular surface meshes. They use, for each surface node, a local projection plane where the patch around the node is smoothed. Then, the new node location is projected back close to the original triangulation. On the other hand, direct relocation methods obtain an ideal location of the nodes on the surface. To this end, the mesh optimization is expressed in terms of the parametric coordinates of an approximated representation of the original surface (Garimella et al., 2004; Garimella and Shashkov, 2004; Shivanna et al., 2010). In particular, Shivanna et al. (2010) presents two methods for the smoothing and untangling of quadrilateral meshes defined on underlying triangulated surfaces. The first is based on the optimization of the mesh on local parametric spaces, and the second is based on the projection of the advancing directions on the discrete surface. In Gargallo-Peiró et al. (2014) we also formulated a smoothing and untangling optimization technique for linear elements in terms of the parametric coordinates of the nodes. However, we use the original CAD representation instead of a smooth representation of an initial triangulation. Moreover, the proposed method was independent of the surface parameterization, well suited then to optimize meshes on low-quality parameterizations.

It is worth noting that in geometry processing optimization approaches have been used to reparameterize triangular surface meshes (Mullen et al., 2008). Then, the obtained parameterization can be used to remesh the discrete representation of the initial surface (Alliez et al., 2005, 2003). On the contrary, we want to use the initial continuous parameterization of the CAD surface and not a piecewise linear approximation. In particular, our objective is to generalize for high-order elements the technique presented in Gargallo-Peiró et al. (2014), that is independent of the parameterization, avoiding the requirement of reparameterizing to obtain a high-quality mesh on a low-quality parameterization of the initial CAD surface. Finally, we highlight that for linear elements, all the reviewed smoothing and untangling methods except reference Gargallo-Peiró et al. (2014) use an approximated representation of the geometry of the model.

2.3.2 Validation and generation of high-order meshes on surfaces

Similar to the linear case, a high-quality curved surface mesh is a basic prerequisite to generate high-quality curved volumetric mesh. Therefore, specific procedures have been developed to generate curved meshes on the boundaries surfaces. These procedures can also be classified according to the same three groups than for planar and volumetric meshes, Section 2.2.1.

In the first group (Dey et al., 2001b; Luo et al., 2004; Luo, 2005; Jiao and Wang, 2012; Clark et al., 2013) topological operations, such as edge deletion or edge and face swapping, are first applied in order to adapt the mesh topology to the curved surfaces. Then, edge nodes and inner face nodes are relocated. For instance, reference Dey et al. (2001b) deals with quadratic elements, and proposes to relocate the mid-edge nodes to enforce that the tangent vectors at the vertices of the boundary tetrahedral faces verify a given criterion. Later, references Luo et al. (2004) and Luo (2005) extended topology modification techniques to higher order degrees, and proposed a method to curve the inner edges of the surface mesh according to their distance to the geometry curves. A similar approach based on topological operations and node relocation is also used in Jiao and Wang (2012) and Clark et al. (2013) to generate a curved high-order surface mesh when the exact CAD representation is not available and the geometry is approximated by a triangulation.

In the second group, reference Sherwin and Peiró (2002) proposes a method to generate surface meshes by means of solving a linear elasticity problem. In particular, the surface parameterization is used to write the elastic problem in terms of the parametric coordinates of the surface nodes, leading to a non-linear minimization problem.

The third group of methods presents two alternatives to generate surface meshes by means of optimization procedures. On the one hand, reference Xie et al. (2012) formulates a local optimization approach that uses the surface geodesics to compute the location of surface nodes. The proposed algorithm requires an additional projection step to ensure that the inner face nodes lie on the exact physical surface. On the other hand, references Remacle et al. (2013) and Toulorge et al. (2013) propose a global optimization method for high-order tetrahedral meshes that constrains the displacements of the surface nodes using the surface parameterization. In order to avoid tangled elements a log-barrier approach (Sastry et al., 2012a) is used to penalize small values of the determinant of the Jacobian.

A crucial step in the *a posteriori* process is to detect invalid elements. As it has been previously highlighted, for planar and volumetric high-order elements several approaches have been proposed to detect the validity of the mapping (Mitchell et al., 1971; Dey et al., 1997, 2001a; Luo et al., 2002, 2004; Shephard et al., 2005; Field, 1983; Baart and Mulder, 1987; Johnen et al., 2013), and to define suitable quality measures (Salem et al., 1997, 2001; Yuan et al., 1994; Knupp, 2009; Branets and Carey, 2005; Salem et al., 2001; George and Borouchaki, 2012; Roca et al., 2012; Gargallo-Peiró et al., 2013a, 2014a). However, we are not aware of any other work related to the definition quality measures for curved high-order meshes on parameterized surfaces. Herein, we present a new technique to extend the Jacobian-based distortion measures for planar linear triangles presented in Knupp (2001a, 2003a), to high-order nodal elements of any polynomial degree on parameterized surfaces. Specifically, we define the distortion and quality measures as the deviation of the physical high-order element with respect to an ideal triangle, as it is proposed in Roca et al. (2012) and Gargallo-Peiró et al. (2014a) for planar and volumetric curved high-order elements. Similarly to our previous work for linear elements (Gargallo-Peiró et al., 2014), the developed measures are expressed in terms of the parametric coordinates of the mesh nodes and are independent of the surface parameterization.

In this work, we generate nodal high-order meshes from CAD geometries by means of an *a posteriori* procedure. In particular, we propose a global non-linear least-squares optimization based on the minimization of the defined distortion measure. However, when the linear mesh is curved to match the geometry, invalid (tangled) elements can appear. To overcome this drawback, the distortion measure is regularized according to Escobar et al. (2003) and Gargallo-Peiró et al. (2014), penalizing inverted element configurations. Moreover, since the distortion measure for high-order elements is independent of the surface parameterization, we obtain a method that generates untangled (valid) and smoothed (high-quality) curved high-order meshes from the exact CAD representation regardless of the quality of its parameterization.

Chapter 3

Distortion and quality measures for high-order planar and volumetric meshes

In the last decades several computational methods have been widely used to solve partial differential equations (PDE) in applied sciences and engineering. Some of these methods allow the use of unstructured meshes, such as the finite element method (FEM), the finite volume method (FVM), and the discontinuous Galerkin method (DG). The unstructured methods have been proven to be very successful to solve PDE in complex domains (geometry flexibility). To solve a PDE with these methods, an unstructured mesh of the domain is generated. Then, a linear system is created by assembling the contributions of each mesh element to the system matrix. These contributions can be computed by integrating directly in the physical element or by changing the variable and integrating in a master element.

To apply the master element approach, it is required to use a differentiable, invertible and smooth mapping (diffeomorphism) from the master element to the mesh element. Hence, the mapping has to be expressed by means of differentiable functions and the mesh elements have to be valid (non-folded) and present high-quality (regular shape). If one element is invalid then the determinant of the mapping Jacobian presents non-positive values. These non-positive determinant values invalidate the change of variable, and therefore, the obtained solution. Moreover, if one element has low quality then the element is distorted respect a regular element. Thus, the approximation accuracy is degraded and the solution may be polluted by the introduced error (Shewchuk, 2002). In summary, quality measures have to be used to assess the validity and quality of a given mesh.

The main contribution of this work is to present a technique that allows extending any Jacobian based quality measure for linear elements to high-order elements of any polynomial degree. Similarly to the linear elements technique, we measure the deviation of the physical element respect an ideal element. Specifically, we integrate the selected Jacobian based distortion measure in the curved element. Then, the quality measure for high-order elements is defined as the inverse of this distortion measure. The resulting quality inherits some of the properties of the original linear quality measures, Section 3.2. We also check that the proposed measure detects non-valid and low-quality elements for different initial Jacobian based quality measures, Section 3.3.1.

The rest of the chapter is organized as follows. Following, in Section 3.1, we review the preliminary work and we state the notation used in this chapter. In Section 3.2 we present the definition of distortion and quality measures for high-order simplicial elements. Next, in Section 3.3.1 we study the behavior of the presented quality measures. Finally, in Section 3.3.2, we detail present several examples in order to asses the defined distortion and quality measures.

3.1 Preliminaries and notation

In this section, we first review the definition of Jacobian-based distortion measures for linear elements. In addition, we present the notation required for high-order elements and we introduce the different sets of elements that we will require in order to define the proposed distortion measures.

3.1.1 Distortion and quality measures for linear elements

We start by reviewing the distortion measures for linear elements presented in Knupp (2001a, 2003a). Consider a linear tetrahedron in the initial configuration, E^I, having the desired shape and size, and the corresponding linear tetrahedron in the physical space, E^P. To measure the deviation between these two elements, we consider the unique affine mapping, $\boldsymbol{\phi}_E$, from E^I to E^P, see Figure 3.1. The mapping $\boldsymbol{\phi}_E$, can be

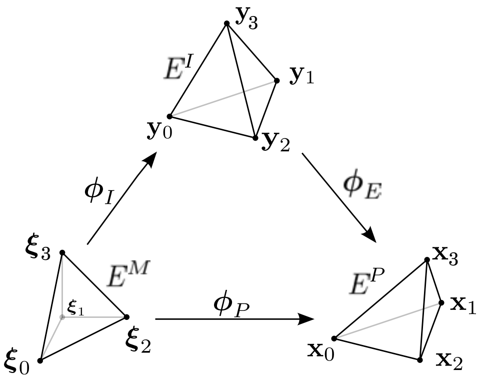

Figure 3.1: Mappings between the master, ideal and physical linear elements.

easily expressed in terms of two additional mapping, $\boldsymbol{\phi}_P$ and $\boldsymbol{\phi}_I$, between the master element E^M and the initial, E^I, and physical element, E^P, respectively. Thus, $\boldsymbol{\phi}_E$ is determined by the composition

$$\boldsymbol{\phi}_E : E^I \xrightarrow{\boldsymbol{\phi}_I^{-1}} E^M \xrightarrow{\boldsymbol{\phi}_P} E^P.$$

Since $\boldsymbol{\phi}_E$ is affine, its Jacobian, $\mathbf{D}\boldsymbol{\phi}_E$, is constant. Note that the Jacobian of $\boldsymbol{\phi}_E$ encodes the deviation of the translation-invariant features of the physical element with respect to the ideal one. Hence, several distortion measures of the physical element can be defined in terms of $\mathbf{D}\boldsymbol{\phi}_E$. These distortion measures, herein denoted by η, quantify the deviation of one or several features (shape, size, skewness, degeneracy,...) of the physical element with respect to the ideal one in the scale range $[1, \infty)$. These measures assign $\eta = 1$ to the ideal element, and tend to ∞ as the element features degenerate. The corresponding quality measure is defined as

$$q := \frac{1}{\eta} \in [0, 1]. \tag{3.1}$$

For the remaining of this work, we use two different distortion measures. On the one hand, we use the shape distortion measure presented in Knupp (2001a):

$$\eta(\mathbf{D}\boldsymbol{\phi}_E) \quad = \quad \frac{\|\mathbf{D}\boldsymbol{\phi}_E\|^2}{d\ |\sigma|^{2/d}}, \tag{3.2}$$

where d is the spatial dimension, $\|\cdot\|$ is the Frobenius norm, and $\sigma = \det(\mathbf{D}\boldsymbol{\phi}_E)$. This distortion measure quantifies the deviation of the shape of the physical element with respect to the ideal shape. On the other hand, we consider the Oddy measure presented in Oddy et al. (1988):

$$\eta(\mathbf{D}\boldsymbol{\phi}_E) = \frac{3\left(\|\mathbf{D}\boldsymbol{\phi}_E^T\,\mathbf{D}\boldsymbol{\phi}_E\|^2 - \frac{1}{3}\|\mathbf{D}\boldsymbol{\phi}_E\|^4\right)}{d\ \sigma^{4/d}}, \tag{3.3}$$

that evaluates the condition number of the metric tensor defined by the element. We note that these distortion measures are invariant to translation and rotations, equal 1 when the ideal and physical elements only differ by a scale factor, and tend to ∞ as E^P becomes degenerate.

To deal with inverted elements ($\sigma \leq 0$), and specially to untangle meshes in the optimization procedure, we use the regularization of the determinant σ proposed in Escobar et al. (2003). This regularization can be applied to Jacobian-based distortion measures where the determinant of the Jacobian appears in the denominator. Specifically, we replace σ in Equations (3.2) and (3.3) by

$$\sigma_\delta(\sigma) = \frac{1}{2}\left(\sigma + \sqrt{\sigma^2 + 4\delta^2}\right), \tag{3.4}$$

where δ is a numerical parameter that has to be determined (Escobar et al., 2003; Gargallo-Peiró et al., 2014). In Section 4.2.2 we detail an automatic procedure to compute the parameter δ for optimization purposes.

In this manner, we consider the regularized distortion measures,

$$\eta_\delta(\mathbf{D}\boldsymbol{\phi}_E) = \frac{\|\mathbf{D}\boldsymbol{\phi}_E\|^2}{d\ |\sigma_\delta|^{2/d}}, \tag{3.5}$$

$$\eta_\delta(\mathbf{D}\boldsymbol{\phi}_E) = \frac{3\left(\|\mathbf{D}\boldsymbol{\phi}_E^T\,\mathbf{D}\boldsymbol{\phi}_E\|^2 - \frac{1}{3}\|\mathbf{D}\boldsymbol{\phi}_E\|^4\right)}{d\ \sigma_\delta^{4/d}}. \tag{3.6}$$

It is important to point out that without the proposed regularization, η has an asymptote when $\sigma = 0$ (where an element becomes non-valid). Note that it is required to regularize σ to remove this asymptote and therefore, allow to the optimization procedure recovering from the non-valid configuration (tangled). The modified determinant σ_δ is always greater or equal than zero. Moreover, for $\delta > 0$, $\sigma_\delta(\sigma)$ is a strictly increasing function, such that $\sigma_\delta(0) = \delta$ and that tends to 0 when σ tends to $-\infty$. Specifically, η_δ is a smooth function with no asymptotes and it is always defined. For small values of δ, the minimum of η_δ is close to the valid minimum of η_0.

To assign quality zero for degenerated elements (negative σ), we compute the limit of η_δ when δ tends to zero. Therefore, for quality evaluation, we use the following distortion measure:

$$\eta_0 := \lim_{\delta \to 0} \eta_\delta. \tag{3.7}$$

We point out that the image of η_0 is also $[1,\infty)$. For valid elements, the limit is defined, and hence, η_0 is equal to η. Thus, the minimum of η_0 is 1. When the element is not valid ($\sigma \leq 0$), then the limit is not defined. Moreover, the limit of σ_δ is

$$\sigma_0 := \lim_{\delta\to 0} \sigma_\delta = (\sigma + |\sigma|)/2. \tag{3.8}$$

Hence, when a positive σ tends to zero, σ_δ tends to zero, and η_0 to infinity and therefore, q tends to zero.

3.1.2 High-order mesh: function spaces and inner products

Analogously to the linear case, for each high-order element we set its corresponding ideal, E^I. In our approach, E^I will always be a straight-sided high-order element that will represent the desired shape of the physical element. It is important to point out that we allow each element to have a different ideal element. Therefore, we define the ideal mesh as the set of ideal elements such that

$$\mathcal{M}_I = \bigcup_{e=1}^{n_E} E_e^I, \tag{3.9}$$

where n_E is the number of elements.

Given the mesh $\mathcal{M}_I$, we consider the spaces of scalar functions

$$\begin{aligned} \mathcal{U}_E &:= \{u \in \mathcal{P}^p(E^I)\}, \\ \mathcal{U} &:= \{u \in \mathcal{C}^0(\mathcal{M}_I) \mid u_{|_{E^I}} \in \mathcal{U}_E,\ \forall E^I \in \mathcal{M}_I\}, \end{aligned} \tag{3.10}$$

and the space of vector functions

$$\begin{aligned} \boldsymbol{\mathcal{U}}_{\boldsymbol{E}} &:= \{\mathbf{u} \in \left[\mathcal{P}^p(E^I)\right]^d\}, \\ \boldsymbol{\mathcal{U}} &:= \{\mathbf{u} \in \left[\mathcal{C}^0(\mathcal{M}_I)\right]^d \mid \mathbf{u}_{|_{E^I}} \in \boldsymbol{\mathcal{U}}_{\boldsymbol{E}},\ \forall E^I \in \mathcal{M}_I\}, \end{aligned} \tag{3.11}$$

where $\mathcal{P}^p(E^I)$ is the space of polynomials of degree p on the element E^I.

Next, we define the inner product of two scalar functions on $\mathcal{M}_I$ as

$$\langle f, g\rangle_{\mathcal{M}_I} := \sum_{e=1}^{n_E} \langle f_{|_{E_e^I}}, g_{|_{E_e^I}}\rangle_{E_e^I}, \tag{3.12}$$

expressed in terms of the inner product of two scalar functions in the element E^I,

$$\langle f, g\rangle_{E^I} := \int_{E^I} f(\mathbf{y})\ g(\mathbf{y}) \mathrm{d}\mathbf{y}. \tag{3.13}$$

The norms corresponding to these inner products are

$$\|f\|_{\mathcal{M}_I} := \sqrt{\langle f, f\rangle_{\mathcal{M}_I}}, \tag{3.14}$$

$$\|f\|_{E^I} := \sqrt{\langle f, f\rangle_{E^I}}. \tag{3.15}$$

3.1.3 High-order mesh: representation

Given a physical curved high-order element, E^P, and fixed it corresponding straight-sided high-order ideal element, E^I, E^P can be expressed as

$$E^P = \boldsymbol{\phi}_E(E^I), \tag{3.16}$$

where $\boldsymbol{\phi}_E$ in $\boldsymbol{\mathcal{U}}_{\boldsymbol{E}}$ is the high-order mapping between E^I and E^P. Moreover, the physical element can be expressed through a high-order master element E^M by means of the two representation mappings $\boldsymbol{\phi}_P$ from E^M to E^P and $\boldsymbol{\phi}_I$ from E^M to E^I. Hence, Equation (3.16) can be re-written as:

$$E^P = \boldsymbol{\phi}_E(E^I) = \boldsymbol{\phi}_P \circ \boldsymbol{\phi}_I^{-1}(E^I). \tag{3.17}$$

According to Equation (3.16), we have that each physical element is the image of an ideal element. Thus, we can assume that the physical mesh is the image of the ideal mesh by a mapping ϕ_h in $\boldsymbol{\mathcal{U}}$. We define the mapping ϕ_h element by element as:

$$\phi_{h|_{E_e^I}} := \boldsymbol{\phi}_{E_e},$$

where $\boldsymbol{\phi}_{E_e}$ is the high-order mapping between E_e^I and E_e^P. Specifically, each physical element can be written as:

$$E_e^P = \phi_h(E_e^I) = \phi_{h|_{E_e^I}}(E_e^I) = \boldsymbol{\phi}_{E_e}(E_e^I).$$

Hence, the physical mesh is defined as

$$\mathcal{M}_P = \bigcup_{e=1}^{n_E} E_e^P.$$

Remark 3.1. *We choose E^I as a valid straight-sided element. That is, $\boldsymbol{\phi}_I$ is an invertible affine mapping and therefore, a global diffeomorphism. Thus, we can use the change of variable determined by $\boldsymbol{\phi}_I$ to compute the inner product as:*

$$\langle f, g\rangle_{E^I} := \int_{E^M} f(\boldsymbol{\phi}_I(\boldsymbol{\xi}))\; g(\boldsymbol{\phi}_I(\boldsymbol{\xi}))\; |\det \mathbf{D}\boldsymbol{\phi}_I(\boldsymbol{\xi})|\; d\boldsymbol{\xi}. \tag{3.18}$$

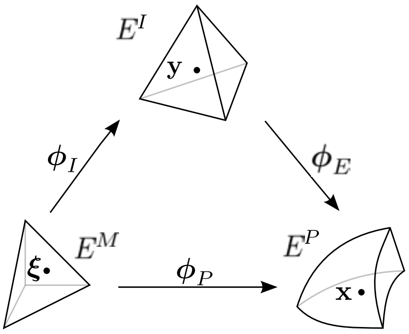

Figure 3.2: Mappings between the master, ideal and physical high-order elements.

To compute this integral, we have to use a numerical quadrature that ensures that polynomials of degree $6p-3$ *are integrated exactly. Specifically, the quadrature uses* $(q+1)(q+2)/2$ *integration points for triangles, and* $(q+1)(q+2)(q+3)/6$ *for tetrahedra, where* $q = 3p-2$*, as specified in Huerta et al. (2012, 2013).*

3.2 Distortion and quality measures for high-order simplicial elements

This section is divided in two parts. First, we present the definition of distortion and quality measure for a high-order simplicial element of any polynomial degree. Next, we present several properties of the proposed definitions.

3.2.1 Definitions

Given an ideal element $E^I \subset \mathbb{R}^d$, and a physical element $E^P \subset \mathbb{R}^d$, we want to characterize the validity of E^P in terms of E^I. Note that E^P can be computed as the image of E^I by means of the mapping $\boldsymbol{\phi}_E$ in $\boldsymbol{\mathcal{U}_E}$, see Equation (3.16). We define the quality of the element E^P in terms of the the mapping $\boldsymbol{\phi}_E$. Note that, similar to the linear case, this mapping encodes the deviation of the physical element with respect to the ideal one. Since $\boldsymbol{\phi}_E$ is non-linear for high-order elements, we need a distortion measure for non-linear mappings. To this end, given a distortion measure for linear elements η, we define:

Definition 3.1. The *regularized point-wise distortion measure* of $\boldsymbol{\phi}_E$ at a point $\mathbf{y}$ in E^I is,

$$\mathrm{M}_\delta \boldsymbol{\phi}_E(\mathbf{y}) := \eta_\delta(\mathbf{D}\boldsymbol{\phi}_E(\mathbf{y})). \tag{3.19}$$

Note that the distortion M for a non-linear mapping $\boldsymbol{\phi}_E$ is casted to evaluate a regularized distortion measure η_δ for linear mappings, see Section 3.1.1. Therefore, it is well defined since the Jacobian $\mathbf{D}\phi$ at a given point is a linear mapping.

Now, we can define the corresponding regularized distortion measure for a high-order element, and for a high-order mesh:

Definition 3.2. The *regularized distortion measure for a high-order element* is

$$\eta_{\delta,E} := \frac{\|\mathrm{M}_\delta \boldsymbol{\phi}_E\|_{E^I}}{\|1\|_{E^I}}, \tag{3.20}$$

where $\|1\|_{E^I}$ is the measure of the ideal element.

Definition 3.3. The *regularized distortion measure for a high-order mesh* is

$$\eta_{\delta,\mathcal{M}} := \frac{\|\mathrm{M}_\delta \boldsymbol{\phi}_E\|_{\mathcal{M}_I}}{\|1\|_{\mathcal{M}_I}}, \tag{3.21}$$

where $\|1\|_{\mathcal{M}_I}$ is the measure of the ideal mesh.

Remark 3.2. *The presented distortion measures are always defined (even for inverted elements), since they are defined in terms of a regularized Jacobian-based distortion measure.*

Next, we define the distortion and quality measures for a high-order element:

Definition 3.4. The *point-wise distortion measure* of $\boldsymbol{\phi}_E$ at a point $\mathbf{y}$ in E^I is,

$$\begin{aligned} \mathrm{M}\boldsymbol{\phi}_E(\mathbf{y}) &:= \lim_{\delta\to 0} \mathrm{M}_\delta \boldsymbol{\phi}_E(\mathbf{y}) = \lim_{\delta\to 0} \eta_\delta(\mathbf{D}\boldsymbol{\phi}_E(\mathbf{y})) \\ &\overset{Eq.(3.7)}{=} \eta_0(\mathbf{D}\boldsymbol{\phi}_E(\mathbf{y})). \end{aligned} \tag{3.22}$$

Now, we can define the corresponding distortion and quality measures for a high-order element:

Definition 3.5. The *distortion measure for a high-order element* is

$$\eta_E := \lim_{\delta\to 0} \eta_{\delta,E} \overset{Eq.(3.20)}{=} \lim_{\delta\to 0} \frac{\|\mathrm{M}_\delta \boldsymbol{\phi}_E\|_{E^I}}{\|1\|_{E^I}}, \tag{3.23}$$

where $\|1\|_{E^I}$ is the measure of the ideal element.

Definition 3.6. The *quality measure for a high-order element* is:

$$q_E := \lim_{\delta \to 0} \frac{1}{\eta_{\delta,E}}. \tag{3.24}$$

Similarly, we can state the corresponding distortion and quality measures for a high-order mesh.

Definition 3.7. The *distortion measure for a high-order mesh* is

$$\eta_{\mathcal{M}} := \lim_{\delta \to 0} \eta_{\delta,\mathcal{M}} \overset{Eq.(3.21)}{=} \lim_{\delta \to 0} \frac{\|\mathrm{M}_{\delta} \boldsymbol{\phi}_E\|_{\mathcal{M}_I}}{\|1\|_{\mathcal{M}_I}}, \tag{3.25}$$

where $\|1\|_{\mathcal{M}_I}$ is the measure of the ideal mesh.

Definition 3.8. The *quality measure for a high-order mesh* is:

$$q_{\mathcal{M}} := \lim_{\delta \to 0} \frac{1}{\eta_{\delta,\mathcal{M}}}. \tag{3.26}$$

Remark 3.3. *The distortion measures for a high-order element and a high-order mesh are not defined (diverge) if an element is inverted. Reciprocally, the corresponding quality measures are zero if the element is not valid.*

Remark 3.4. *The presented measures can be extended to determine the distortion and quality for other types of representations for curved elements . For instance, changing the element representation in Section 3.1.2 from triangles/tetrahedra to quadrilaterals/hexahedra ($\boldsymbol{\mathcal{U}_E}$ determined by a base defined as the tensor product of 1D polynomials), all the presented definitions are straight forward extended to quadrilaterals and hexahedra. Specifically, for hexahedra, changing the function spaces in Section 3.1.2 from a polynomial representation to NURBS or B-splines, the proposed definitions are extended to the isogemetrical analysis (Hughes et al., 2005; Höllig et al., 2012). Moreover, changing also the representation of the physical element in terms of the ideal, Section 3.1.3, the quality measures can be applied for the homotopy based representation for tetrahedral elements bounded by NURBS used in NEFEM (Sevilla et al., 2011).*

3.2.2 Properties

In this section, we analyze the properties of the high-order distortion and quality measures presented in Definitions 3.5, 3.6, 3.7, and 3.8. First, we detail a set of properties that guarantee that the measures are well-defined. Second, we proof that the defined measures preserve some features of the original Jacobian-based distortion measure for linear elements.

3.2.2.1 Well-defined measures

To guarantee that the proposed measures are well defined, first we show that the measures for high-order elements are consistent with the existing Jacobian-based measures for linear elements. Second, we show that they have the same image range than in the linear case. Finally, we proof that the high-order measures guarantee that if an element has positive quality, only a region of measure zero can have non-positive Jacobian.

Lemma 3.1 (Consistency)**.** *For the linear tetrahedral case, $p = 1$, the distortion measure η_E for a high-order element is equivalent to the Jacobian distortion measure η_0 for linear elements.*

Proof. Since $\boldsymbol{\phi}_E$ is affine, $\mathbf{D}\boldsymbol{\phi}_E$ is constant on E^I. Hence,

$$\begin{aligned}
\eta_E^2 &= \lim_{\delta\to 0} \frac{\|\mathrm{M}_\delta \boldsymbol{\phi}_E\|_{E^I}^2}{\|1\|_{E^I}^2} \\
&= \lim_{\delta\to 0} \left(\frac{1}{\|1\|_{E^I}^2} \int_{E^I} {\eta_\delta}^2(\mathbf{D}\boldsymbol{\phi}_E(\mathbf{y}))\mathrm{d}\mathbf{y} \right) \\
&= \lim_{\delta\to 0} {\eta_\delta}^2(\mathbf{D}\boldsymbol{\phi}_E) = {\eta_0}^2(\mathbf{D}\boldsymbol{\phi}_E).
\end{aligned}$$

□

Lemma 3.2 (Distortion range)**.** *The distortion measure for high-order elements, η_E maintains the image range of the respective distortion measure for linear elements, η_0.*

Proof. First, we point out that a distortion measure for linear mappings η_0 has image $[1, \infty)$. On the one hand, if we consider an element where the region $R = \{\mathbf{y} \in E^I \mid \det \mathbf{D}\boldsymbol{\phi}_E(\mathbf{y}) \le 0\}$ has non-null measure, the element distortion is divergent.

On the other hand, if the measure of R is null, we can apply the Lebesgue's monotone convergence theorem, re-written for completeness in Remark 3.5. First, since $\sigma_{\delta_1}(\sigma) > \sigma_{\delta_2}(\sigma)$ for $\delta_1 > \delta_2$, we highlight that η_δ is an increasing succession as δ decreases, see Equations (3.4) and (3.6). Next, we take a numerable succession of functions, $\{\eta_{\delta_n}\}_{n\to\infty}$, being $\delta_n = \frac{1}{n}$. Note that, almost everywhere, $\{\eta_{\delta_n}\}_{n\to\infty}$ converges point-wise to η_0, and is dominated by η_0. Then, by Lebesgue's monotone convergence theorem, see Remark 3.5, η_0 is measurable, and:

$$\begin{aligned}
\eta_E &= \lim_{\delta\to 0}\frac{1}{\|1\|_{E^I}}\left(\int_{E^I}{\eta_\delta}^2(\mathbf{D}\boldsymbol{\phi}_E(\mathbf{y}))\ \mathrm{d}\mathbf{y}\right)^{\frac{1}{2}}\\
&= \frac{1}{\|1\|_{E^I}}\left(\int_{E^I}{\eta_0}^2(\mathbf{D}\boldsymbol{\phi}_E(\mathbf{y}))\ \mathrm{d}\mathbf{y}\right)^{\frac{1}{2}}\\
&\overset{\eta_0\geq 1}{\geq} \frac{1}{\|1\|_{E^I}}\left(\int_{E^I}1^2\ \mathrm{d}\mathbf{y}\right)^{\frac{1}{2}} = 1.
\end{aligned}$$

In particular, if the element is the ideal, the Jacobian is the identity, and hence, $\eta_0 = 1$ on E^I, see Knupp (2001a, 2003a). Consequently, for the ideal element we have that η_E is exactly one. This way, we have that $\mathrm{Im}(\eta_E) = [1,\infty)$.

□

Remark 3.5 (Lebesgue's monotone convergence theorem)**.** *Let* (X,Σ,μ) *be a measure space. Let* $\{f_n\}$ *be a point-wise non-decreasing sequence of* $[0,\infty]$*-valued* $\Sigma-$*measurable functions, i.e. for every* $k\geq 1$ *and every* x *in* X*,*

$$0 \leq f_k(x) \leq f_{k+1}(x).$$

Next, set the point-wise limit of the sequence $\{f_n\}$ *to be* f*. That is, for every* x *in* X*,* $f(x) := \lim_{k\to\infty} f_k(x)$*. Then* f *is* $\Sigma-$*measurable and*

$$\lim_{k\to\infty}\int f_k\,\mathrm{d}\mu = \int f\,\mathrm{d}\mu.$$

Moreover, if the sequence $\{f_k\}$ *satisfies the assumptions* $\mu-$*almost everywhere, one can find a set* $N\subset\Sigma$ *with* $\mu(N)=0$ *such that the sequence* $\{f_n(x)\}$ *is non-decreasing for every* $x\notin N$*. The result remains true because for every* k*,*

$$\int f_k\,\mathrm{d}\mu = \int_{X\setminus N} f_k\,\mathrm{d}\mu, \quad \textit{and} \quad \int f\,\mathrm{d}\mu = \int_{X\setminus N} f\,\mathrm{d}\mu,$$

provided that f *is* $\Sigma-$*measurable.*

Corollary 3.1 (Quality range)**.** The quality measure for high-order elements, q_E, maintains the image range of the respective quality measures for linear elements, q.

Proof. Note that q_E, Equation (3.24), directly inherits the image range of q from Lemma 3.2 and from its definition in terms of η_E.

□

In particular, let q be a quality measure for linear elements with image range $[0,1]$. Then, q_E is a quality measure for high-order elements with image range $[0,1]$. Note that Lemma 3.2 and Corollary 3.1 also apply to the distortion and quality measures for high-order meshes.

Proposition 3.1 (Element distortion validation)**.** *If the distortion measure for high-order elements η_E is defined, then the region $R = \{\mathbf{y} \in E^I \mid det\, \mathbf{D}\boldsymbol{\phi}_E(\mathbf{y}) \leq 0\}$ has measure zero.*

Proof. We can write $\eta_{\delta,E}$ as

$$\eta^2_{\delta,E} = \frac{\|\mathrm{M}_\delta \boldsymbol{\phi}_E\|^2_{E^I}}{\|1\|^2_{E^I}} = \frac{\left(\|\mathrm{M}_\delta \boldsymbol{\phi}_E\|^2_{E^I\setminus R} + \|\mathrm{M}_\delta \boldsymbol{\phi}_E\|^2_R\right)}{\|1\|^2_{E^I}}.$$

Note that the limit of the regularized distortion $\mathrm{M}_\delta \boldsymbol{\phi}_E(\mathbf{y})$ is not defined when $\sigma = \det \mathbf{D}\boldsymbol{\phi}_E(\mathbf{y}) \leq 0$. Hence the norm on $E^I \setminus R$ is always defined, but it is not so for R. Now, we consider the integral on R:

$$\begin{aligned} \|\mathrm{M}_\delta \boldsymbol{\phi}_E\|^2_R &= \lim_{\delta \to 0} \int_R \mathrm{M}_\delta \boldsymbol{\phi}^2_E(\mathbf{y}) \; \mathrm{d}\mathbf{y} \\ &= \lim_{\delta \to 0} \int_R \eta^2_\delta(\mathbf{D}\boldsymbol{\phi}_E(\mathbf{y})) \; \mathrm{d}\mathbf{y}. \end{aligned}$$

Since the limit is not defined for this region, the integral $\|\mathrm{M}_\delta \boldsymbol{\phi}_E\|^2_R$ is only defined if the measure of R has measure zero. Hence, η_E is defined only if R has measure zero.

□

Corollary 3.2 (Element quality validation)**.** If the quality measure for high-order elements q_E is not zero, then R has measure zero.

Proof. By means of Definition 3.6, q_E is zero if and only if η_E is not defined. By Proposition 3.1, if η_E is defined, the measure of R is zero. Consequently, if $q_E > 0$, the measure of R is zero too. □

Corollary 3.3 (Mesh distortion validation)**.** If the distortion measure for high-order meshes $\eta_{\mathcal{M}}$ is defined, then the region $R_{\mathcal{M}} = \{\mathbf{y} \in \mathcal{M}_I \mid \det \mathbf{D}\phi_h(\mathbf{y}) \leq 0\}$ has measure zero.

Proof. Following the reasoning of Proposition 3.1. □

Corollary 3.4 (Mesh quality validation)**.** If the quality measure for high-order meshes $q_{\mathcal{M}}$ is not zero, then $R_{\mathcal{M}}$ has measure zero.

Proof. Following the reasoning of Corollary 3.2. □

3.2.2.2 Invariance preservation

In this section, we show that the measure for high-order elements preserves the invariance under affine mappings of the selected Jacobian-based measure. In order to proof the next proposition, we underline that we can re-write the representation mapping $\boldsymbol{\phi}_E$ in $\boldsymbol{\mathcal{U}_E}$ using a high-order basis $\{B_i\}_{i=1,\ldots,n_p}$ of degree p, that we choose to be a partition of the unity, and a set of n_p control points with coordinates $\mathbf{b}_i$ in $\mathbb{R}^d$, for $i = 1, \ldots, n_p$. Then, the high-order mapping from $\boldsymbol{\phi}_E$, can be expressed as:

$$\begin{array}{rccl} \boldsymbol{\phi}_E : & E^I \subset \mathbb{R}^d & \longrightarrow & E^P \subset \mathbb{R}^d \\ & \mathbf{y} & \longmapsto & \mathbf{x} = \boldsymbol{\phi}_E(\mathbf{y}) = \displaystyle\sum_{i=1}^{n_p} B_i(\mathbf{y})\ \mathbf{b}_i. \end{array} \tag{3.27}$$

Proposition 3.2 (Affine invariant measures)**.** *If η is invariant under an affine mapping ψ, then η_E is also invariant under ψ.*

Proof. The affine mapping ψ can be written as $\psi(\mathbf{x}) := \mathbf{A}\mathbf{x} + \mathbf{t}$, where $\mathbf{A}$ is the linear mapping, and $\mathbf{t}$ is the translation vector. Rewriting $\boldsymbol{\phi}_E$ in terms of a polynomial base that is partition of the unity, Equation (3.27), we prove that the transformation of the high-order element by the mapping ψ is the representation mapping for the control points $\psi(\mathbf{b}_i),\ i = 1, \dots, n_p$:

$$\begin{aligned}
&\psi(\boldsymbol{\phi}_E(\mathbf{y}; \mathbf{b}_1, \dots, \mathbf{b}_{n_p})) \\
&\qquad = \mathbf{A} \cdot \boldsymbol{\phi}_E(\mathbf{y}; \mathbf{b}_1, \dots, \mathbf{b}_{n_p}) + \mathbf{t} \\
&\qquad = \sum_{i=1}^{n_p} \mathbf{A}\mathbf{b}_i B_i(\boldsymbol{\phi}_I^{-1}(\mathbf{y})) + \mathbf{t} \\
&\qquad \overset{(*)}{=} \sum_{i=1}^{n_p} \mathbf{A}\mathbf{b}_i B_i(\boldsymbol{\phi}_I^{-1}(\mathbf{y})) + \sum_{i=1}^{n_p} \mathbf{t} B_i(\boldsymbol{\phi}_I^{-1}(\mathbf{y})) \\
&\qquad = \sum_{i=1}^{n_p} (\mathbf{A}\mathbf{b}_i + \mathbf{t}) B_i(\boldsymbol{\phi}_I^{-1}(\mathbf{y})) \\
&\qquad = \boldsymbol{\phi}_E\left(\mathbf{y}; \psi(\mathbf{b}_1), \dots, \psi(\mathbf{b}_{n_p})\right),
\end{aligned}$$

where in $(*)$ we use that B_i is a partition of unity. Thus, the Jacobian for the transformed element is

$$\begin{aligned}
&\mathbf{D}\left(\boldsymbol{\phi}_E(\mathbf{y}; \psi(\mathbf{b}_1), \dots, \psi(\mathbf{b}_{n_p}))\right) \\
&\qquad = \mathbf{D}\left(\mathbf{A}\boldsymbol{\phi}_E(\mathbf{y}; \mathbf{b}_1, \dots, \mathbf{b}_{n_p}) + \mathbf{t}\right) \\
&\qquad = \mathbf{A} \cdot \mathbf{D}\boldsymbol{\phi}_E(\mathbf{y}; \mathbf{b}_1, \dots, \mathbf{b}_{n_p}).
\end{aligned}$$

Finally, we can prove the invariance of η_E under ψ:

$$\begin{aligned}
&\eta_E^2(\psi(\mathbf{b}_1), \dots, \psi(\mathbf{b}_{n_p})) \\
&= \lim_{\delta \to 0} \frac{1}{\|1\|_{E^I}} \int_{E^I} \eta_\delta^2(\mathbf{D}\boldsymbol{\phi}_E(\mathbf{y}; \psi(\mathbf{b}_1), \dots, \psi(\mathbf{b}_{n_p}))) \, \mathrm{d}\mathbf{y} \\
&= \lim_{\delta \to 0} \frac{1}{\|1\|_{E^I}} \int_{E^I} {\eta_\delta}^2(\mathbf{A} \cdot \mathbf{D}\boldsymbol{\phi}_E(\mathbf{y}; \mathbf{b}_1, \dots, \mathbf{b}_{n_p})) \, \mathrm{d}\mathbf{y} \\
&\overset{(\diamond)}{=} \lim_{\delta \to 0} \frac{1}{\|1\|_{E^I}} \int_{E^I} {\eta_\delta}^2(\mathbf{D}\boldsymbol{\phi}_E(\mathbf{y}; \mathbf{b}_1, \dots, \mathbf{b}_{n_p})) \, \mathrm{d}\mathbf{y} \\
&= \eta_E^2(\mathbf{b}_1, \dots, \mathbf{b}_{n_p}),
\end{aligned}$$

where in $(\diamond)$ we use that η is invariant under ψ.

□

Corollary 3.5 (Invariance preservation)**.** If a Jacobian based distortion and quality measures for linear elements fulfil any of the following properties:

- translation-free,

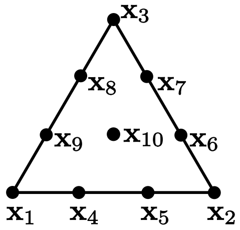

Figure 3.3: Triangle of polynomial degree three.

- scale-free,
- rotation-free,
- symmetry-free,

then the proposed high-order distortion and quality measures, Definitions 3.5 and 3.6, also hold the same properties.

Proof. Since q_E is defined as the inverse of η_E, we only have to prove the previous properties for η_E, Equation (3.23). All the *translations, scalings, rotations, symmetries*, and their compositions are affine mappings. Therefore, by Proposition 3.2, we have that η_E inherits the invariance of η under translation, scaling, rotation or symmetry.

□

3.3 Results

In this section, we present two examples in order to illustrate the applications of the proposed quality measures. First, we illustrate the behavior of the defined distortion and quality measures for a triangle of polynomial degree three. Second, we show that the defined measures allow checking the validity of high-order tetrahedral meshes. The proposed algorithm has been implemented in C++ in the meshing environment EZ4U (Roca et al., 2010, 2007).

3.3.1 Behavior of the high-order quality measure

In this section, we illustrate the behavior of the proposed quality measure for high-order elements. We consider a triangle of polynomial degree three and, using Equation

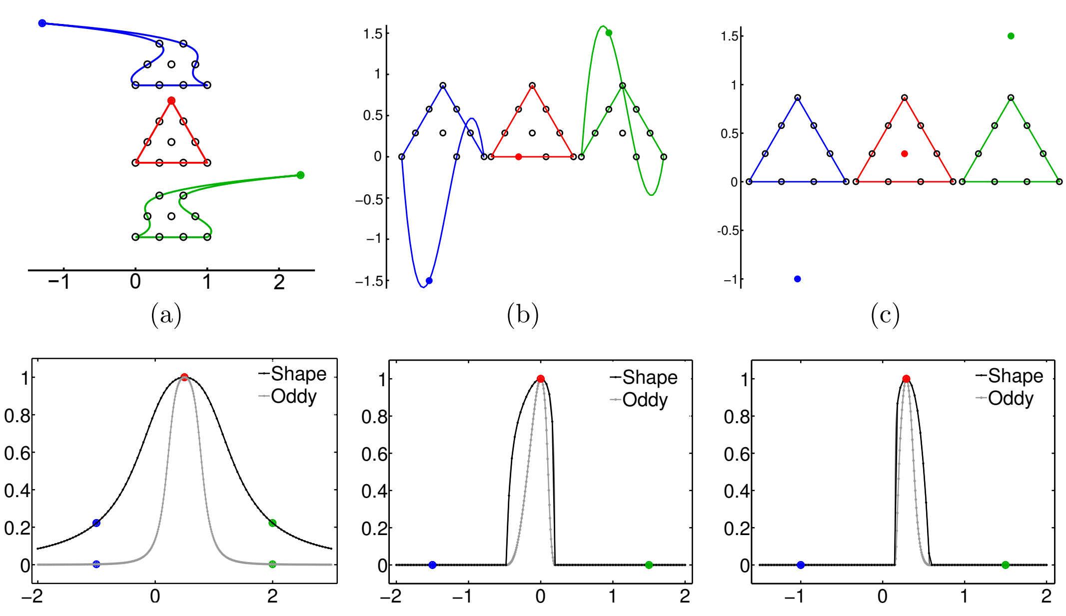

(a) (b) (c)

(d) (e) (f)

Figure 3.4: Configurations and high-order qualities for the three tests of a triangle of polynomial degree three in an equispaced distribution. (a) and (d) vertex node $\mathbf{x}_3$ moves on the x direction, (b) and (e) edge node $\mathbf{x}_4$ moves on the y direction; and (c) and (f) face node $\mathbf{x}_{10}$ moves on the y direction.

Free node	Location 1 (bue)	Location 2 (red)	Location 3 (green)
$\mathbf{x}_3$	$\left(-1, \sqrt{3}/2\right)$	$\left(1/2, \sqrt{3}/2\right)$	$\left(2, \sqrt{3}/2\right)$
$\mathbf{x}_4$	$(1/3, -3/2)$	$(1/3, 0)$	$(1/3, 3/2)$
$\mathbf{x}_{10}$	$(1/2, -1)$	$\left(1/2, \sqrt{3}/6\right)$	$(1/2, 1.5)$

Table 3.1: Locations of the free node for displacements restricted to one direction.

(3.23), we compute the distortion measure for the shape and Oddy distortion measures, presented in Equations (3.2) and (3.3), respectively. Then, we use the defined quality measure for high-order elements, see Equation (3.24), to evaluate the validity of the element configurations.

We apply three tests to a triangle of polynomial degree three with nodes located in two configurations. On the one hand, we consider an equispaced node configuration,

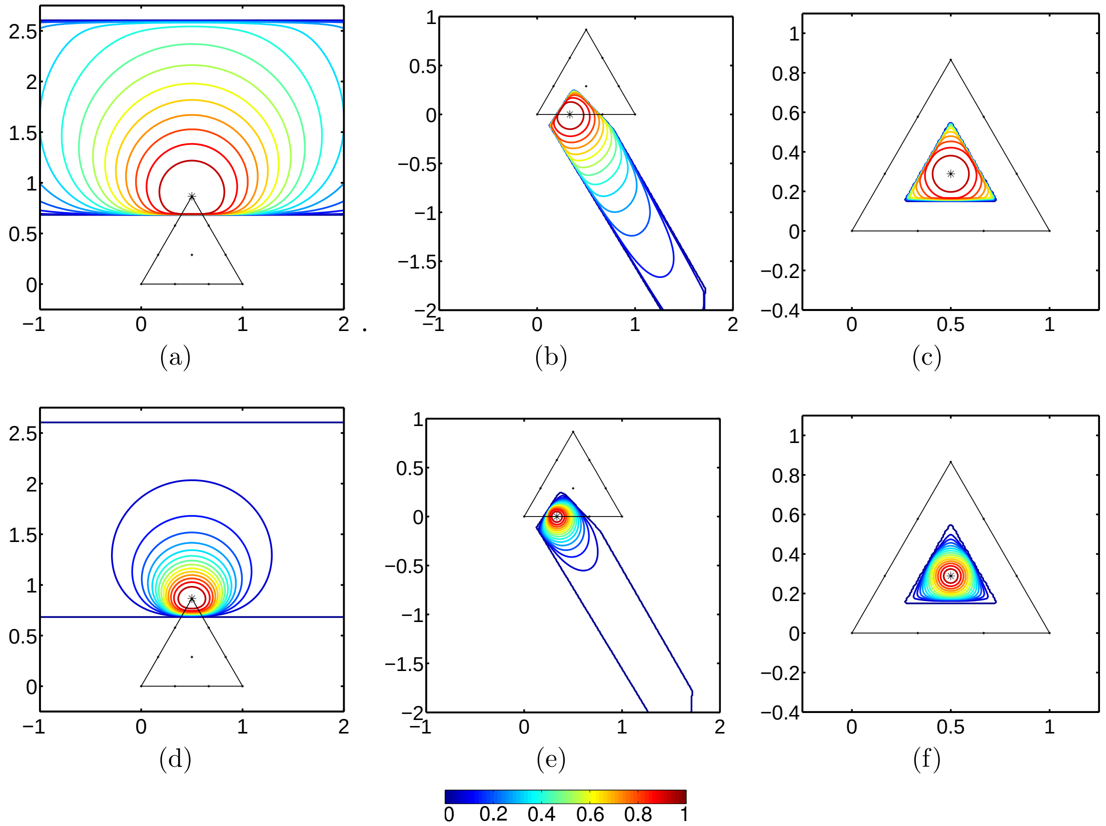

Figure 3.5: Level sets for the three high-order quality measures (in rows: shape and Oddy) of a triangle of polynomial degree three with an equispaced distribution when the free node is: (a,d) the vertex node $\mathbf{x}_3$; (b,e) the edge node $\mathbf{x}_4$; and (c,f) the face node $\mathbf{x}_{10}$.

see Figure 4:

$$\mathbf{x}_1 = (0,0)\,, \mathbf{x}_2 = (1,0)\,, \mathbf{x}_3 = \left(\tfrac{1}{2}, \tfrac{\sqrt{3}}{2}\right), \mathbf{x}_4 = \left(\tfrac{1}{3}, 0\right),$$
$$\mathbf{x}_5 = \left(\tfrac{2}{3}, 0\right), \mathbf{x}_6 = \left(\tfrac{5}{6}, \tfrac{\sqrt{3}}{6}\right), \mathbf{x}_7 = \left(\tfrac{2}{3}, \tfrac{\sqrt{3}}{3}\right),$$
$$\mathbf{x}_8 = \left(\tfrac{1}{3}, \tfrac{\sqrt{3}}{3}\right), \mathbf{x}_9 = \left(\tfrac{1}{6}, \tfrac{\sqrt{3}}{6}\right), \mathbf{x}_{10} = \left(\tfrac{1}{2}, \tfrac{\sqrt{3}}{6}\right).$$

On the other hand, we consider a triangle with nodes located on a distribution that provides a quasi-optimal Lebesgue constant (Warburton, 2006; Hesthaven and Warburton, 2007). In each test we consider a free node (keeping the rest of nodes fixed in the original location) and compute the quality of the high-order element in terms of the location of this node. The free nodes are: the vertex node $\mathbf{x}_3$, the edge node $\mathbf{x}_4$, and the face node $\mathbf{x}_{10}$. First, to visualize the configuration of the high-order triangle

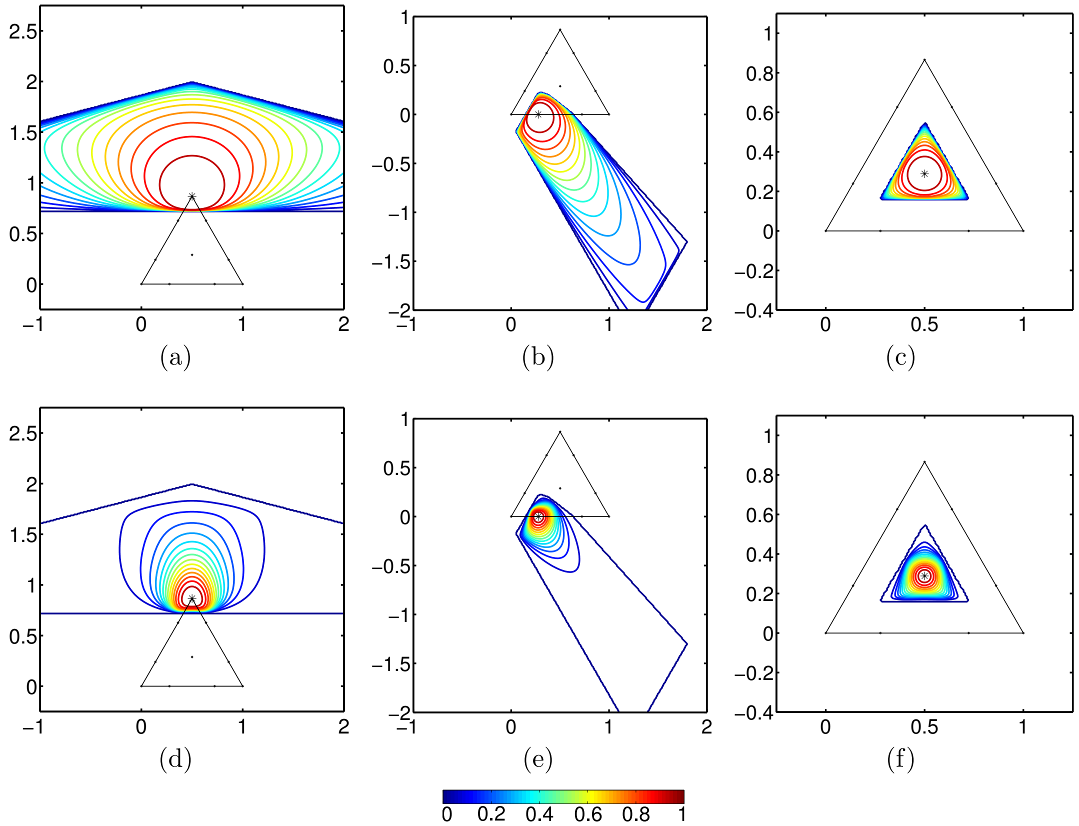

Figure 3.6: Level sets for the two high-order quality measures (in rows: shape and Oddy) of a triangle of polynomial degree three with a distribution that provides a quasi-optimal Lebesgue constant, when the free node is: (a,d) the vertex node $\mathbf{x}_3$; (b,e) the edge node $\mathbf{x}_4$; and (c,f) the face node $\mathbf{x}_{10}$.

and to analyze in detail the behavior of each high-order quality measure, in Figure 3.4 we restrict the displacement of the free nodes to one direction:

- vertex node $\mathbf{x}_3 = \left(x_3, \sqrt{3}/2\right)$ moves along the x direction, $x_3 \in [-2, 3]$;
- edge node $\mathbf{x}_4 = (1/3, y_4)$ moves along the y direction, $y_4 \in [-2, 2]$;
- face node $\mathbf{x}_{10} = (1/2, y_{10})$ moves along the y direction, $y_{10} \in [-3/2, 2]$.

In each column of Figure 3.4 we illustrate the behavior elements and of both qualities in terms of each free node. In the first row, we display the configuration of the high-orde elements for three different positions of the free node. In the second row, we include the value of the shape and Oddy quality measures.

Second, in Figure 3.5 we show the contour plots of the previous high-order qualities for each test when the free nodes are allowed to move in $\mathbb{R}^2$. As expected, we realize that the two high-quality measures have similar behavior. Moreover, both of them define the same feasible region. However, the Oddy high-order quality is more strict and tends to zero faster than the shape quality measure. In these tests, the high-order quality measure detects all the non-valid configurations. Specifically, it detects tangled elements due to crossed edges or folded areas. Several conclusions can be drawn from Figure 3.4. From Figures 3.4(a), 3.4(b), and 3.4(c) we realize that moving away a node from its ideal location induces oscillations in the representation of the high-order element. Hence, tangled elements can appear, see for instance Figures 3.4(a), and 3.4(b). From Figures 3.4(d), 3.4(e), and 3.4(f) we first realize that the defined measure properly detects when the high-order element folds and gets tangled. In Figures 3.4(e) and 3.4(f) all the measures detect the same tangling positions, where the quality achieves the zero value. Moreover, in all cases, the two measures detect the proper ideal configurations, with quality equals to 1. Finally, Figures 3.4 and 3.5 show that vertex nodes have larger feasible regions than edge or face nodes. Moreover, the edge nodes have larger feasible regions than the face ones.

To conclude, in Figure 3.6 we show the behavior of the quality measure when the triangle has nodes located on the second proposed distribution. We can observe that the behavior of the defined measures is the same than in the equispaced case presented in Figure 3.5. Specifically, both measures detect the same feasible regions and the same ideal configuration. Note that the overall behavior of the defined measures is the same independently of the selected configuration. However, each node distribution defines different feasible regions. Nevertheless, we point out that for computational purposes we will always use the non-equispaced distribution, since it provides a quasi-optimal Lebesgue constant (Warburton, 2006; Hesthaven and Warburton, 2007).

3.3.2 Applications

One of the main applications of distortion (quality) measures is to check if a mesh is valid to perform a numerical simulation. Specifically, a quality measure has to properly detect if an element is non-valid (and assign 0 value). Moreover, the measure has to penalize the deviation of the element with respect to the target ideal (and assign value 1 to the ideal). By Lemma 3.2, the distortion for high-order elements, η_E, has image $[1, \infty)$. In particular, it has value 1 when the element is ideal, and tends to ∞

Table 3.2: Shape quality statistics for a hollow sphere (relative quality). The mesh is composed by 160 elements.

p	#nodes	Mesh	Figure	Min.Q.	Max.Q.	MeanQ.	Std.Dev.	#inv
2	302	Initial	3.7(a)	0.00	0.97	0.51	0.40	59
		Smoothed	3.7(d)	0.91	0.99	0.98	0.02	0
4	2042	Initial	3.7(b)	0.00	0.97	0.81	0.28	16
		Smoothed	3.7(e)	0.95	1.00	0.99	0.01	0
6	6502	Initial	3.7(c)	0.00	0.96	0.81	0.27	15
		Smoothed	3.7(f)	0.95	1.00	0.99	0.01	0

Table 3.3: Shape quality statistics for a hollow sphere (absolute quality). The mesh is composed by 160 elements.

p	#nodes	Mesh	Figure	Min.Q.	Max.Q.	MeanQ.	Std.Dev.	#inv
2	302	Initial	3.7(a)	0.00	0.92	0.46	0.36	59
		Smoothed	3.7(d)	0.57	0.97	0.77	0.11	0
4	2042	Initial	3.7(b)	0.00	0.95	0.74	0.19	16
		Smoothed	3.7(e)	0.65	0.97	0.81	0.09	0
6	6502	Initial	3.7(c)	0.00	0.92	0.69	0.24	15
		Smoothed	3.7(f)	0.64	0.98	0.81	0.09	0

as the element degenerates. Conversely, the quality measure, q_E, has image $[0, 1]$.

The measures defined in Section 3.2 can accommodate different ideal elements. We select two different type of ideals depending on the framework of the computation. On the one hand, it is necessary to be able to evaluate the quality of the elements of a mesh with respect to the same target tetrahedron. Hence, to obtain an absolute quality measurement, we select the equilateral tetrahedron as ideal (standard ideal for isotropic meshes (Knupp, 2001a)).

On the other hand, for optimization purposes we use a relative quality measurement. That is, we assume that we have an initial linear mesh, and for each high-order curved element we select the corresponding initial high-order straight-sided element as ideal. It is important to point out that we assume that the initial linear mesh verifies the geometrical constraints required by the numerical simulation Therefore, by the *a posteriori* mesh generation procedure, our final goal is to optimize the location of the inner nodes to obtain a valid (without tangled elements) high-order mesh composed by elements with a shape similar to the one in the initial linear mesh.

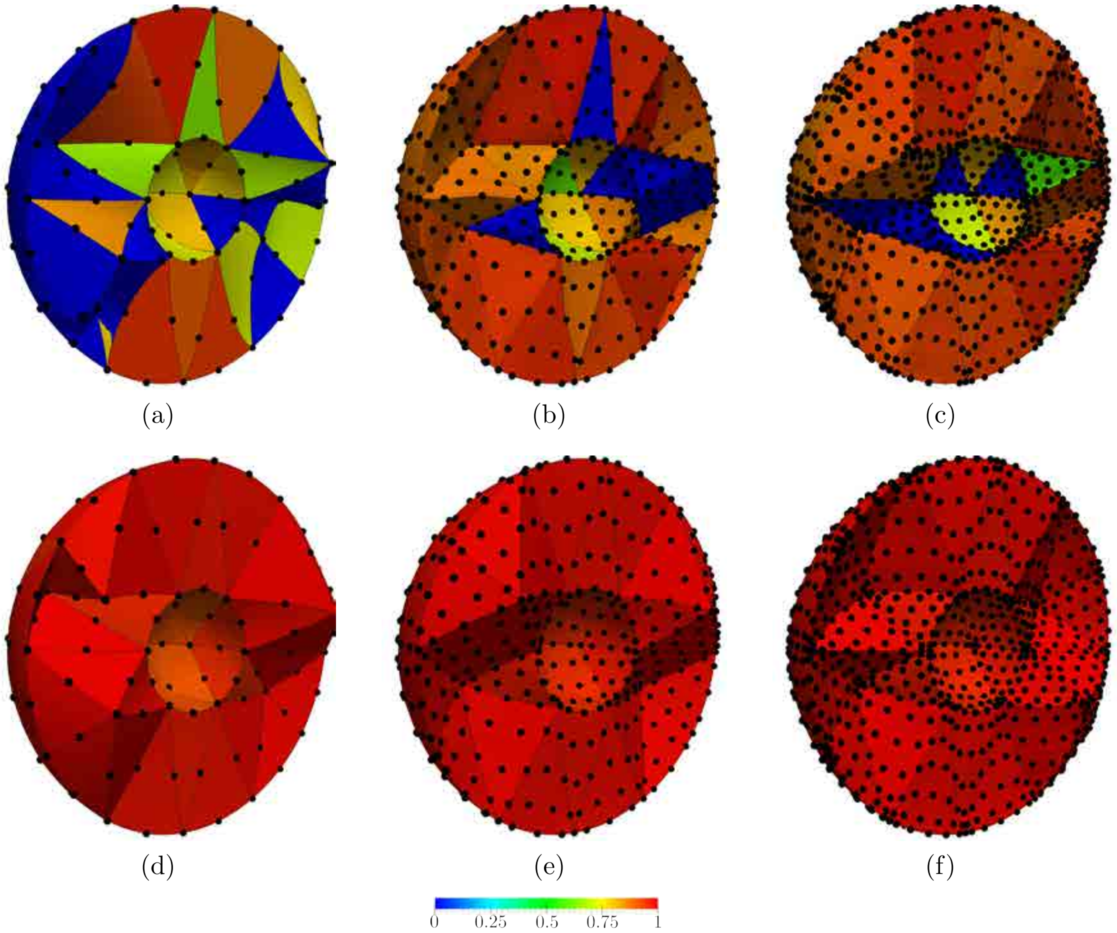
(a) (b) (c)

(d) (e) (f)

Figure 3.7: Tetrahedral meshes of polynomial degree 2, 4 and 6 colored according to the shape quality measure (initial straight-sided ideal) on a hollow sphere: (a-c) initial meshes, and (d-f) smoothed meshes.

3.3.2.1 Validation of isotropic curved high-order meshes

In this section, we illustrate that the defined measure is capable of quantifying the validity of a high-order tetrahedron. Specifically, we show that the measure detects when an element is valid or not. Moreover, it properly determines the deviation of a given element with respect to the considered ideal.

We consider a hollow sphere of inner radius 1 and external radius of 3, and we generate a coarse tetrahedral mesh. Then, we generate three meshes of polynomial degree 2, 4 and 6 with the same topology, and we tangle them, see Figures 3.7(a), 3.7(b) and 3.7(c). In Figures 3.7(d), 3.7(e) and 3.7(f) we present the meshes smoothed with the procedure that is presented in Chapter 4. Note that the optimization approach gen-

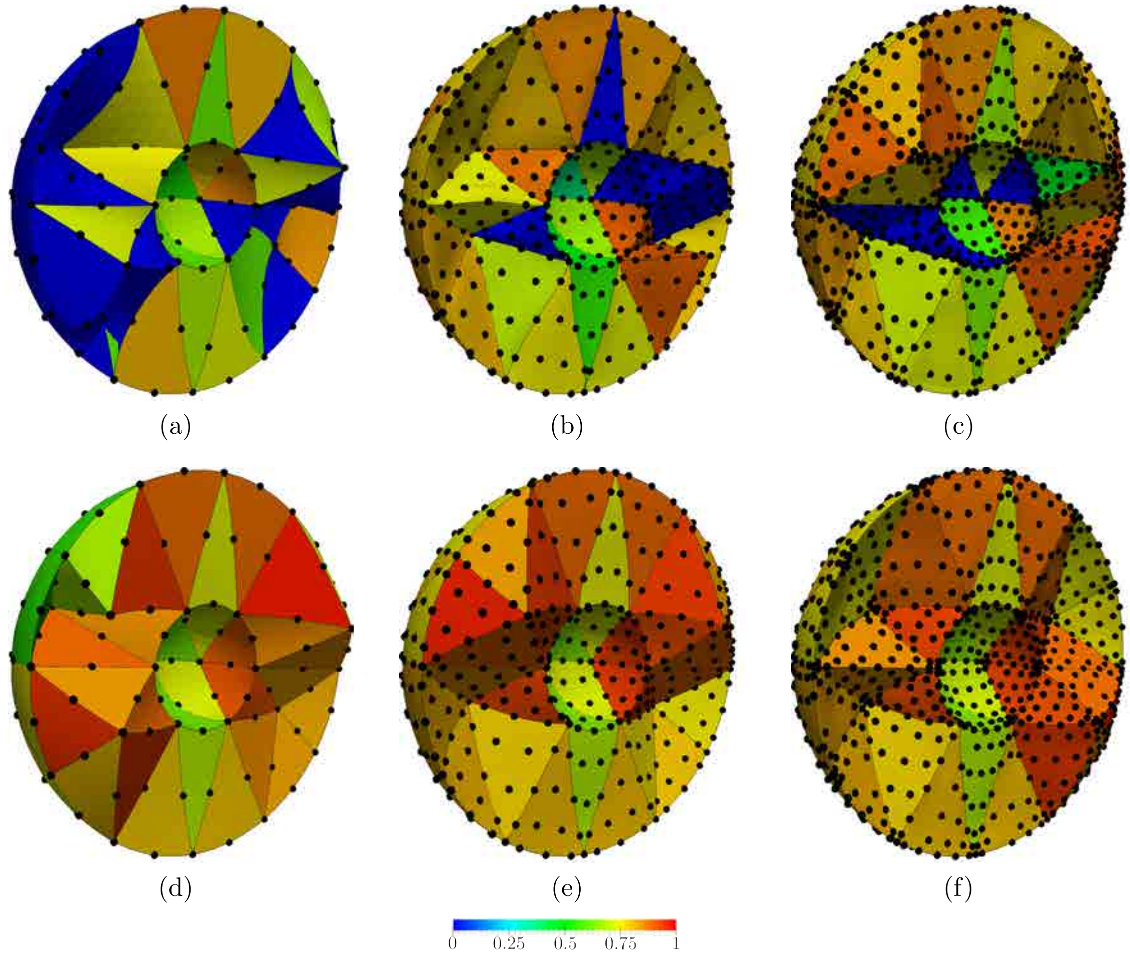
(a) (b) (c)

(d) (e) (f)

Figure 3.8: Tetrahedral meshes of polynomial degree 2, 4 and 6 colored according to the shape quality measure (equilateral ideal) on a hollow sphere: (a-c) initial meshes, and (d-f) smoothed meshes.

erates valid and high-quality meshes. In Table 3.2 we present the quality statistics of the obtained mesh. Note that all the inverted elements have been untangled and the overall quality statistics improved. The quality statistics and the displayed quality in Figure 3.7 are computed taking as ideal the initial linear mesh (relative quality). Therefore, we observe that in Figures 3.7(d), 3.7(e) and 3.7(f) almost all the elements are of quality one. That is, the optimized mesh is close to the straight-sided one.

In addition, we can check the validity and measure the shape regularity of the mesh elements by using the absolute quality, see Figure 3.8. We include the mesh statistics for the absolute quality in Table 3.3. As expected, the absolute measure detects the same invalid elements. Furthermore, the obtained quality values are lower than the ones obtained with the relative quality measure since each element is compared to a regular tetrahedron instead of the initial straight-sided configuration. Nevertheless, the minimum value is 0.57 and the mean is above 0.7. That is, the absolute quality measure is determining that the curved high-order elements have a shape close to the ideal regular tetrahedron.

Note that meshes that are composed by regular elements provide higher accuracy to represent a function that is not known a priori (Shewchuk, 2002). Therefore, the absolute quality measure can be used to measure the suitability of a curved high-order mesh to approximate arbitrary functions. If the mesh does not present enough regularity, we can fix it by adding a pre-process step to the *a posteriori* procedure. Specifically, we propose to improve the regularity of the initial linear mesh by minimizing its absolute distortion measure. Then, this mesh is converted to a high-order straight-sided mesh and it is set up as the ideal mesh. Now, we can curve the boundary and minimize the relative distortion measure, respect this new ideal mesh, to obtain a curved high-order mesh composed by elements of higher regularity.

3.3.2.2 Validation of boundary layer meshes

In this section, we analyze the type of ideal element that it is desired in order to determine the validity of a high-order boundary layer mesh. We consider a mesh of polynomial degree 4 on the exterior domain of a SD7003 airfoil. This mesh has been generated with the procedure presented in Section 6.3.3 from an initial linear mesh with four layers of stretching around the airfoil.

In Figure 3.9 we present two different views of the same high-order mesh. In Figure 3.9(a) we color the elements with the quality respect an equilateral tetrahedron as an ideal element (absolute quality). In Figure 3.9(b), we take as ideal the corresponding straight-sided high-order element from the initial mesh (relative quality). In Table 3.4 we present the statistics of both quality measurements. As we can observe, despite the fact that the absolute quality is useful in general to measure the validity of all the elements with respect to the same framework, it is not so when the mesh is not isotropic. Note that one of the main premises that we have stated is that the *a posteriori* procedure assumes that the input linear mesh is valid and has the desired size and shape for the mesh elements. Hence, in general, for high-order meshes we will use the relative quality measure. This measure is directed towards quantifying the validity of an element with respect to its shape before the curving of the boundary

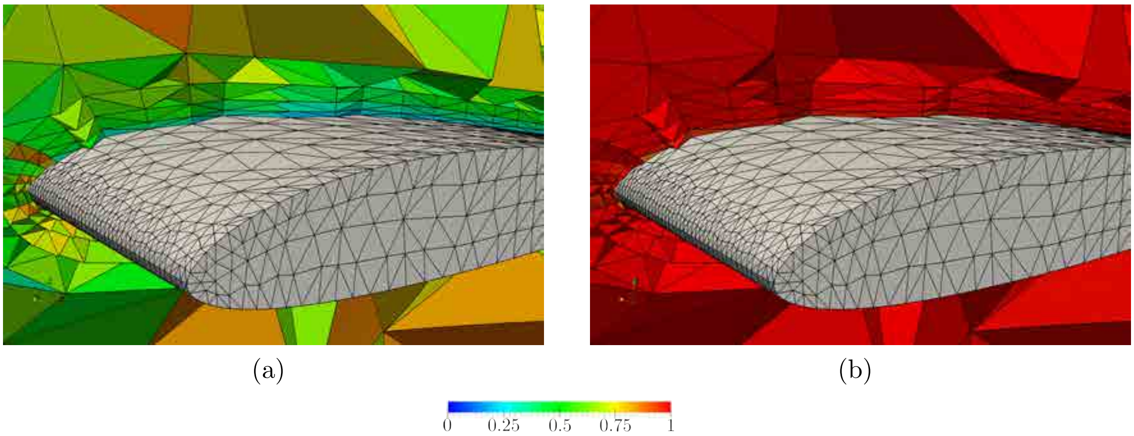

(a)

(b)

Figure 3.9: Tetrahedral boundary layer mesh of polynomial degree 4. Displayed quality: (a) absolute, and (b) relative.

Table 3.4: Shape quality statistics for a hollow sphere (absolute quality). The mesh is composed by 160 elements.

Ideal	Figure	Min.Q.	Max.Q.	MeanQ.	Std.Dev.	#inv
Equilateral	3.9(a)	0.05	1.00	0.65	0.19	0
Straight-sided mesh	3.9(b)	0.24	1.00	0.93	0.05	0

faces. A low value of the relative quality after the boundary curving warns that the Jacobian of the element is not admissible somewhere in the element. However, as we have observed in Section 3.3.2.1, when dealing with an isotropic mesh, the absolute quality can be used to measure the mesh validity.

3.4 Concluding remarks

In this chapter, we have presented a new technique to define distortion (quality) measures for nodal high-order meshes. First, we have defined point-wise distortion measure that determines the validity of the mesh on each point. The point-wise measure is defined in terms of a Jacobian-based distortion measure for linear elements. Second, we have proposed an elemental and a mesh distortion defined in terms of the norm of the point-wise measure.

The proposed definition is valid for any polynomial degree and allows detecting the validity of a high-order mesh. The quality measure assigns zero value to an invalid high-order element, and one if the element is ideal. Moreover, we have proved that if the quality is strictly positive, the region where the determinant is not positive has measure zero. This is of the major importance to check that a curved high-order meshes is valid for computational purposes. Furthermore, if the selected Jacobian-based measure is invariant under a given affinity, the defined measure inherits its invariance.

Finally, we have presented two examples to illustrate the main properties of the developed techniques. First, we have analyzed the behavior of the developed measures by means of studying the validity of a planar triangle of polynomial degree three. Second, we have applied the defined measures to determine the validity of isotropic and boundary layer meshes.

Chapter 4

Optimization of a regularized distortion measure to smooth and untangle curved high-order meshes

---

In the last decade, unstructured high-order methods (Szabo and Babuška, 1991; Schwab, 1998; Deville et al., 2002; Hesthaven and Warburton, 2007; Karniadakis and Sherwin, 2013) have attracted considerable attention from the computational mechanics community. This attention has been prompted by the ability of these methods to approximate with high-fidelity the solution of partial differential equations on complex domains. It is well known that for problems with smooth solutions, the approximation obtained with high-order methods converges exponentially with the order of the approximating polynomial. More generally, high-order methods have been shown to deliver higher accuracy with a lower computational cost than low-order methods in many practical applications (Vos et al., 2010; Cantwell et al., 2011b,a; Löhner, 2011; Yano et al., 2012; Kirby et al., 2012; Huerta et al., 2012, 2013; Löhner, 2013; Wang et al., 2013). In addition, the accurate approximation of the domain geometry eliminates the spurious effects in the solution that can arise from a piecewise linear representation of the curved domain boundaries (Bassi and Rebay, 1997; Dey et al., 1997; Luo et al., 2002; Xue and Demkowicz, 2005; Sevilla et al., 2011). An implicit assumption in high-order methods is that the geometry is represented with sufficient accuracy to enable high convergence rates to be realized.

Despite the attractive features of high-order methods, their adoption for practical applications has been hampered by technical challenges such as the development of robust implementations and the generation of suitable 3D curved meshes. In this thesis, we focus our attention on the generation of high-order meshes for general geometries that are suitable for high-order finite element analyses. To that end, the generated meshes must satisfy two requirements. On one hand, each high-order element must be the image of a valid straight-sided master element through an element-wise invertible mapping. On the other hand, the boundary elements must be curved to ensure that the error introduced in the solution by the inexact approximation of the geometry is smaller than the solution discretization error.

The main contribution of this chapter is to propose a robust smoothing and untangling method to repair and improve the quality of a given high-order mesh. The main applications is to curve a high-order mesh while matching a given mesh boundary. Specifically, we formulate a global non-linear least-squares minimization problem of a regularized distortion minimization measure in which the decision variables are the coordinates of the interior mesh nodes. For each element, we consider the mapping between the initial linear tetrahedron and the curved element in the final mesh. The mapping distortion measure is minimum when the element shape (but not necessarily its size) in the final and initial configurations is preserved. In addition, the mapping distortion measure is regularized so that it is well defined for both valid (unfolded) elements, where the mapping between the linear and curved elements is one-to-one, and invalid (folded), elements where the mapping becomes singular and the determinant of the transformation Jacobian becomes non-positive. For folded elements, the value of the distortion measure is a large positive value which forces the minimization process to untangle the mesh. Once all the elements are untangled, the regularization can be switched off. In that case, the resulting objective function tends to infinity if the Jacobian determinant tends to zero. This form of the objective function prevents untangled (valid) configurations from becoming tangled (invalid) during the optimization process.

The proposed formulation has the following advantages: first, it is capable of transforming an invalid curved high-order mesh to a valid mesh, thanks to the use of the regularized objective function; second, it ensures that initially valid configurations remain valid after transformation; third, it can deal with polynomials of any degree; fourth, it can handle curved boundaries; and fifth, geometrical mesh features features such as element shape, anisotropy are preserved.

We present several examples that demonstrate the advantages of the proposed method. Specifically, we show that the proposed approach is able to untangle consistently non-valid initial elements for approximations up to degree ten and large deformations of the initial mesh boundaries. Moreover, we show that some features of the initial mesh such as non-uniform element size, and anisotropy (boundary layers) are preserved.

The remainder of the chapter is organized as follows. In Section 4.1, we present the proposed optimization formulation. In Section 4.2, we describe the regularization of the distortion measure to untangle invalid meshes. Finally, in Section 4.3, we present several examples to illustrate the advantages and application of the proposed method.

4.1 Formulation of the mesh optimization

In this section, we present a formulation to solve the mesh deformation problem which is based on the optimization of a measure of the mesh distortion. To this end, we use the shape distortion measure for linear elements introduced in Section 3.1.1. This measure can be interpreted as a point-wise measure of the distortion of a deformation map. The continuous version of the mesh curving problem can be stated as finding a deformation map that satisfies a prescribed point-wise distortion. Finally, we present a non-linear least-squares discretization of the continuous problem.

4.1.1 Curving: globally defined smooth mapping

Given an initial domain $\Omega_I \subset \mathbb{R}^d$, and a physical domain $\Omega_P \subset \mathbb{R}^d$, we want to characterize Ω_P in terms of Ω_I. We assume that the physical domain can be defined as the image of a diffeomorphism ϕ in $\mathcal{C}^1(\Omega_I, \Omega_P)$, see Figure 4.1. To determine the desired diffeomorphism ϕ, we need a distortion measure for non-linear mappings. To this end, given a distortion measure for linear elements η, we define the distortion measure of ϕ at a point $\mathbf{y} \in \Omega_I$ as,

$$\mathrm{M}\phi(\mathbf{y}) := \eta(\mathbf{D}\phi(\mathbf{y})). \tag{4.1}$$

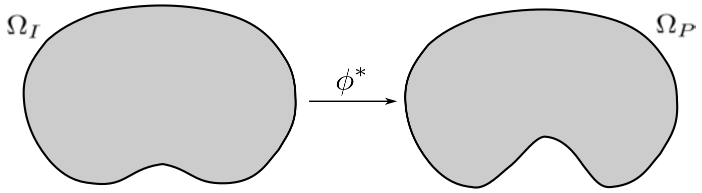

Figure 4.1: Mapping between the initial and physical domains.

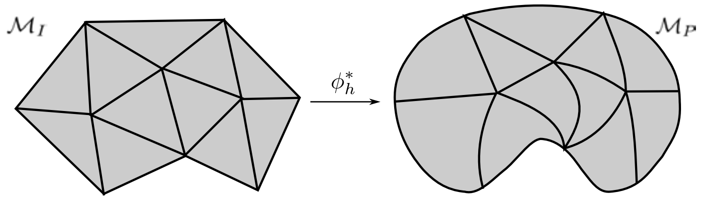

Figure 4.2: Mapping between the initial and physical meshes.

We note that the Jacobian $\mathbf{D}\phi$ at a given point $\mathbf{y}$ is a linear map and therefore, the distortion measure M is well defined.

Given the initial domain Ω_I and the boundary of the physical domain, $\partial\Omega_P$, the continuous problem is that of finding a diffeomorphism ϕ^* between Ω_I and Ω_P such that the distortion measure M is ideal. That is,

$$\begin{aligned} \mathrm{M}\phi^* &= 1, &&\text{in } \Omega_I, \\ \phi^* &= g, &&\text{on } \partial\Omega_I, \end{aligned}$$

where g is the mapping between $\partial\Omega_I$ and $\partial\Omega_P$.

4.1.2 Curving: element-wise defined smooth mapping

We consider that the domain Ω_I is approximated by the mesh $\mathcal{M}_I$ composed by the union of the elements E_e^I, for $e = 1, \cdots, n_E$. In addition, we consider that the prescribed curved boundary $\partial\Omega_P$ is approximated by a surface mesh $\partial\mathcal{M}_P$ determined by a mapping g_h from $\partial\mathcal{M}_I$ to $\partial\mathcal{M}_P$. In this setting, we seek an optimal mapping ϕ_h^* from $\mathcal{M}_I$ to $\mathcal{M}_P$, see Figure 4.2, such that for all E^I in $\mathcal{M}_I$, it has an ideal distortion measure. That is,

$$\mathrm{M}\phi_h^* = 1, \qquad \text{in } \mathcal{M}_I, \tag{4.2}$$

$$\phi_h^* = g_h, \qquad \text{on } \partial\mathcal{M}_I. \tag{4.3}$$

Since we want to obtain a conformal nodal high-order mesh, we seek for the mapping ϕ_h^*, see Figure 4.2 in the space of vector functions

$$\boldsymbol{\mathcal{U}} := \{\mathbf{u} \in \left[\mathcal{C}^0\left(\mathcal{M}_I\right)\right]^d \mid \mathbf{u}_{|_{E^I}} \in \left[\mathcal{P}^p(E^I)\right]^d,\ \forall E^I \in \mathcal{M}_I\},$$

where $\mathcal{P}^p(E^I)$ is the space of polynomials of degree p on the element E^I.

For a given mesh $\mathcal{M}_I$ and a boundary configuration g_h, a mapping ϕ_h such that Equation (4.2) and Equation (4.3) are verified may be, in general, not achievable. To address this issue, we impose the optimality condition in a least-squares sense. That is, we seek ϕ_h^* in $\boldsymbol{\mathcal{U}^D}$ such that

$$\phi_h^* \;=\; \underset{\phi_h \in \boldsymbol{\mathcal{U}^D}}{\operatorname{argmin}} \|\mathrm{M}\phi_h - 1\|^2_{\mathcal{M}_I}, \tag{4.4}$$

where

$$\boldsymbol{\mathcal{U}^D} := \{\phi_h \in \boldsymbol{\mathcal{U}} \mid\ (\mathrm{M}\phi_h - 1) \in \mathcal{L}^2(\mathcal{M}_I), \text{ and } \phi_h = g_h \text{ on } \partial\mathcal{M}_I\}.$$

In Equation (4.4) we define the norms

$$\|f\|_{\mathcal{M}_I} \;:=\; \sqrt{\langle f, f\rangle_{\mathcal{M}_I}}, \tag{4.5}$$

$$\|f\|_{E^I} \;:=\; \sqrt{\langle f, f\rangle_{E^I}}, \tag{4.6}$$

and the inner product for scalar functions f and g in $\mathcal{M}_I$

$$\langle f, g\rangle_{\mathcal{M}_I} \;:=\; \sum_{e=1}^{n_E} \langle f_{|_{E_e^I}}, g_{|_{E_e^I}}\rangle_{E_e^I}, \tag{4.7}$$

$$\langle f, g\rangle_{E^I} \;:=\; \int_{E^I} f(\mathbf{y})\ g(\mathbf{y})\mathrm{d}\mathbf{y}. \tag{4.8}$$

Once ϕ_h^* is found, each element in the physical domain can be obtained as

$$E_e^P = \phi_h^*(E_e^I),$$

and therefore, the desired physical mesh $\mathcal{M}_P$ is composed by the union of the elements E_e^P, for $e = 1, \cdots, n_E$.

4.1.3 Curving: nodal high-order mesh optimization

The minimization problem stated in Equation (4.4) can be rewritten in terms of elemental contributions. In particular, according to Equation (4.7) and Equation

(4.5), we have that

$$\|\mathrm{M}\phi_h - 1\|^2_{\mathcal{M}_I} = \sum_{e=1}^{n_E} \|\mathrm{M}\boldsymbol{\phi}_{h_{|_{E_e^I}}} - 1\|^2_{E_e^I} = \sum_{e=1}^{n_E} \|\mathrm{M}\boldsymbol{\phi}_{E_e} - 1\|^2_{E_e^I} \ ,$$

where $\boldsymbol{\phi}_{h_{|_{E_e^I}}}$ is the mapping $\boldsymbol{\phi}_{E_e}$ between E_e^I and its physical element E_e^P. Therefore, we seek ϕ_h^* in $\boldsymbol{\mathcal{U}^D}$ such that :

$$\phi_h^* = \underset{\phi_h \in \boldsymbol{\mathcal{U}^D}}{\operatorname{argmin}} \|\mathrm{M}\phi_h - 1\|^2_{\mathcal{M}_I} = \underset{\phi_h \in \boldsymbol{\mathcal{U}^D}}{\operatorname{argmin}} \sum_{e=1}^{n_E} \|\mathrm{M}\boldsymbol{\phi}_{E_e} - 1\|^2_{E_e^I}. \tag{4.9}$$

In particular, for nodal high-order elements, and according to Equation (A.2) in Appendix A, $\boldsymbol{\phi}_{E_e}$ depends on the coordinates of the n_p element nodes. Thus, the distortion at a point $\mathbf{y}$ in E_e^I in Equation (4.9) can be written as:

$$\mathrm{M}\boldsymbol{\phi}_{E_e}(\mathbf{y}) = \mathrm{M}\boldsymbol{\phi}_{E_e}(\mathbf{y}; \mathbf{x}_{e,1}, \ldots, \mathbf{x}_{e,n_p})$$

where the pairs (e, j) in $\mathbf{x}_{e,j}$ denotes the local j-th node of element e. Thus, for nodal high-order elements, determining ϕ_h^* in Equation (4.9), is equivalent to determining the coordinates of the nodes of the high-order mesh. Moreover, the element contribution to the objective function only depends on the nodes of that element.

We reorder the coordinates of the nodes, $\mathbf{x}_i$, in such a manner that $i = 1, \ldots, n_F$ are the indexes corresponding to the free (interior) nodes, and $i = n_F + 1, \ldots, n_N$ correspond to the fixed nodes (nodes on the CAD surfaces). Note that the coordinates of the fixed nodes are determined by the function g_h, and can be obtained using the technique presented in Chapter 5 (Gargallo-Peiró et al., 2013a, 2014). Defining

$$f(\mathbf{x}_1, \ldots, \mathbf{x}_{n_F}; \mathbf{x}_{n_F+1}, \ldots, \mathbf{x}_{n_N}) := \frac{1}{2}\|\mathrm{M}\phi_h - 1\|^2_{\mathcal{M}_I}, \tag{4.10}$$

we can formulate the mesh optimization problem as finding $\{\mathbf{x}_1^*, \ldots, \mathbf{x}_{n_F}^*\} \subset \mathbb{R}^3$ such that:

$$\{\mathbf{x}_1^*, \ldots, \mathbf{x}_{n_F}^*\} = \underset{\mathbf{x}_1, \ldots, \mathbf{x}_{n_F} \in \mathbb{R}^3}{\operatorname{argmin}} f(\mathbf{x}_1, \ldots, \mathbf{x}_{n_F}; \mathbf{x}_{n_F+1}, \ldots, \mathbf{x}_{n_N}), \tag{4.11}$$

where $\mathbf{x}_i = g(\mathbf{y}_i)$ for $i = n_F + 1, \ldots, n_N$. In Appendix B, we detail our approach to solve the global minimization problem stated in Equation (4.11). Moreover, we highlight that in Appendix C, we propose a p-continuation technique to accelerate the optimization of curved high-order meshes.

4.2 Mesh untangling

The minimization problem presented in Equation (4.11) is based on a Jacobian-based distortion measure presented in Equation (3.2). This distortion measure becomes infinity when the high-order element is degenerated (when $\sigma = \det(\mathbf{D}\boldsymbol{\phi}_E) = 0$). This feature precludes its use in an untangling procedure. In order to address this issue, we replace the distortion measure in Equation (3.2) by a regularized form.

4.2.1 Regularization of the distortion measure

As highlighted in Section 3.1.1, to incorporate the untangling capability to the optimization method, we use the regularization proposed in Escobar et al. (2003) and replace σ in Equation (3.2) by

$$\sigma_\delta(\sigma) = \frac{1}{2}\left(\sigma + \sqrt{\sigma^2 + 4\delta^2}\right),$$

where δ is a positive element-wise parameter and its selection is discussed in Section 4.2.2. The regularized Jacobian, $\sigma_\delta(\sigma)$, is a monotonically increasing function of σ, such that $\sigma_\delta(0) = \delta$, and tends to 0 when σ tends to $-\infty$, see Figure 4.3.

Using the regularized Jacobian, the modified shape distortion measure becomes,

$$\eta_\delta(\mathbf{D}\boldsymbol{\phi}_E) \quad = \quad \frac{\|\mathbf{D}\boldsymbol{\phi}_E\|^2}{3|\sigma_\delta|^{2/3}}.$$

The use of the regularized Jacobian removes the vertical asymptote at $\sigma = 0$, and therefore, allows the optimization procedure to recover from the non-valid configurations. Moreover, for small values of δ, the minimum of η_δ is close to the minimum of the original shape distortion measure η. We note that the element-wise parameter δ is only set to non-zero values when an invalid mesh configuration is considered. Once all the elements are valid, δ can be set to zero for all the elements. To analyze the validity of a mesh, we set $\delta = 0$, replacing σ_δ in Equation (3.6) by $\sigma_0 = (\sigma + |\sigma|)/2$. In this way, for invalid meshes, σ becomes negative and, $\eta_\delta = \infty$ and $q = 0$.

4.2.2 Selection of the regularization parameter

The regularization parameter δ needs to satisfy the following criteria. On the one hand, δ has to be large enough to ensure that δ^2 is significant compared to σ^2. On

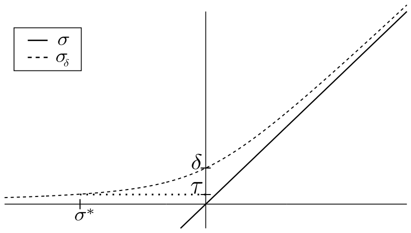

Figure 4.3: Representation of $\sigma_\delta(\sigma)$.

the other hand, it has to be small enough to ensure that the minimum of the modified mesh distortion function is not too far from the original minimum.

In order to simplify the computation of the derivatives of the distortion measure we select a constant value of δ for each element. In particular, we determine δ taking into account the volume of the straight-sided initial element (det $\boldsymbol{\phi}_I$) and only use the regularized distortion measure when the element is invalid ($\sigma \leq 0$).

Let $\sigma^* = -\det \boldsymbol{\phi}_I$ be a reference (negative) value of the determinant of that element. Then, we determine δ by ensuring that $\sigma_\delta(\sigma^*)$ is always positive. Since σ_δ is a strictly increasing function, then we guarantee that $\sigma_\delta > 0$ for $\sigma > \sigma^*$. In particular, we impose

$$\sigma_\delta(\sigma^*) = \frac{1}{2}\left(\sigma^* + \sqrt{(\sigma^*)^2 + 4\delta^2}\right) = \tau > 0,$$

where τ is a given tolerance. Hence,

$$\delta(\sigma^*) = \frac{1}{2}\sqrt{(2\ \tau + |\sigma^*|)^2 - (\sigma^*)^2} = \sqrt{\tau^2 + \tau\ |\sigma^*|}. \tag{4.12}$$

The parameter τ should be small compared to σ. We propose to select τ according to

$$\tau = \alpha\ |\sigma^*|, \tag{4.13}$$

where $\alpha = 10^{-3}$ has been found to work well in practice and used for all the presented examples. The final expression for δ becomes,

$$\delta(\sigma^*) = |\sigma^*|\ \sqrt{\alpha^2 + \alpha}. \tag{4.14}$$

which implies that (see Figure 4.3):

$$\begin{aligned} \sigma_{\delta(\sigma^*)}(0) &= \delta(\sigma^*), \\ \sigma_{\delta(\sigma^*)}(\sigma^*) &= \tau. \end{aligned}$$

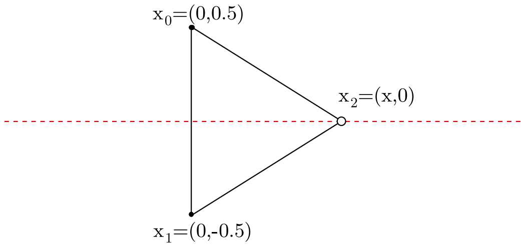

Figure 4.4: Triangle with $\mathbf{x}_2$ moving on a segment.

In order to illustrate the behavior of the regularized distortion measure presented in Equation (3.4) we consider a triangular element with two fixed nodes, $\mathbf{x}_0 = (0, 0.5)$ and $\mathbf{x}_1 = (0, -0.5)$, and examine the mesh distortion measure as the third node $\mathbf{x}_2(x) = (x, 0)$ is moved along the x-axis, see Figure 4.4. In addition, we select the equilateral triangle as the initial element and $\delta = 0.05$ for the regularized distortion measure. Figure 4.5(a) shows the shape distortion measure, Equation (3.2), when node $\mathbf{x}_2$ moves from $x = -5$ to $x = 5$. Note that only $0 < x < \infty$ correspond to valid configurations. For $x \to \pm\infty$ the distortion measure tends to infinity since the triangle tends to a degenerated configuration. The minimum values ($\eta = 1$) are achieved at $x = \pm\sqrt{3}/2$ where the triangle is equilateral (ideal). However, only $x = \sqrt{3}/2$ corresponds to a valid configuration. At the local minimum $x = -\sqrt{3}/2$ the element is inverted and has negative area. Moreover, at $x = 0$, when the triangle has null area, the shape distortion measure has a vertical asymptote. Figure 4.5(b) shows the value of the regularized shape distortion measure, Equation (3.6), when node $\mathbf{x}_2$ moves from $x = -5$ to $x = 5$. To show that the asymptote has been removed, we plot in Figure 4.5(d) the mesh distortion measure in logarithmic scale. The regularization removes the vertical asymptote at $x = 0$, and results in a continuous and differentiable function with a single minimum near $x = \sqrt{3}/2$ (the ideal configuration). Figure 4.5(e) and 4.5(f) plot the shape quality measure and the regularized shape quality measure, respectively. Finally, Figure 4.6 shows the distortion and quality measures when the free node $\mathbf{x}_2$ moves in $\mathbb{R}^2$. When then regularized distortion measure is used, the local minimum outside the feasible region is removed and the function is continuous and differentiable.

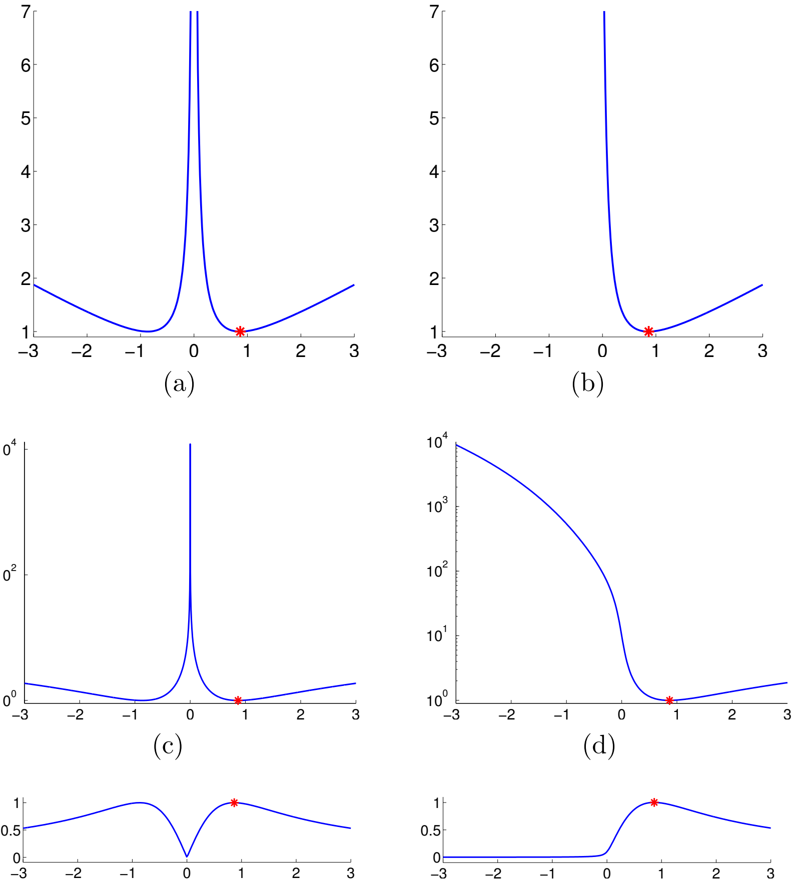

(a) (b)

(c) (d)

(e) (f)

Figure 4.5: Shape distortion and quality measures for the triangle test when node $\mathbf{x}_2$ moves from $x = -5$ to $x = 5$: (a) distortion, (b) regularized distortion, (c) distortion in logarithmic scale, (d) regularized distortion in logarithmic scale, (e) quality, and (d) regularized quality. The ideal configuration of the triangle is plotted with a red dot.

4.3 Results

In this section, we present several examples to illustrate the main features of the proposed approach. First, we focus on the robustness of the proposed method. In particular, we show that our method is capable of smoothing and untangling meshes of high polynomial degrees that contain a large number of inverted elements. That is, the method can generate high-quality curved meshes even if it starts from an invalid configuration resulting from large deformations or concave curved boundaries. Second, we show that our method leads to a curved mesh that preserves the features

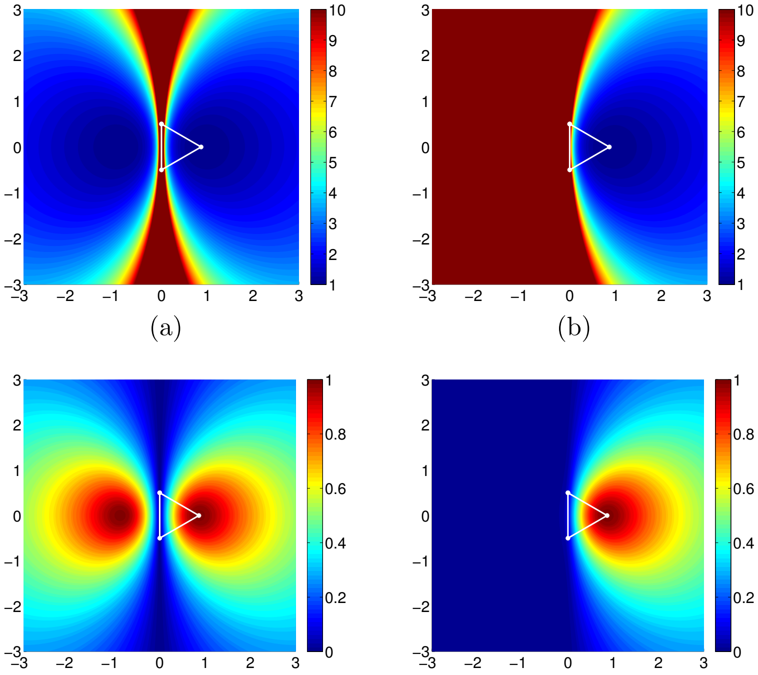

(a) (b)

(c) (d)

Figure 4.6: Shape distortion and quality measures for the triangle test when node $\mathbf{x}_2$ moves in a quadrilateral: (a) distortion, (b) regularized distortion, (c) quality, and (d) regularized quality. The ideal configuration of the triangle is also shown (white).

(size, shape, anisotropy) of the initial linear mesh. Moreover, we highlight that to narrow the test cases, the examples included in this section are exclusively for tetrahedra. In Appendix D we have illustrated several examples where we show that the proposed procedure can also smooth and untangle planar triangle and quadrilateral meshes, and hexahedral meshes.

In all figures, the meshes are colored according to the point-wise quality, *i.e.* the inverse of the distortion, see Equation (3.1) and Equation (4.1). For each example, we present a table summarizing the element quality statistics, see Definition 3.6. Specifically, we show the minimum, the maximum, the mean and the standard deviation of the mesh quality, and the number of tangled elements before the smoothing/untangling process is initiated. We highlight that in all cases, the smoothed mesh increases the minimum and mean values of the mesh quality and decreases its standard deviation.

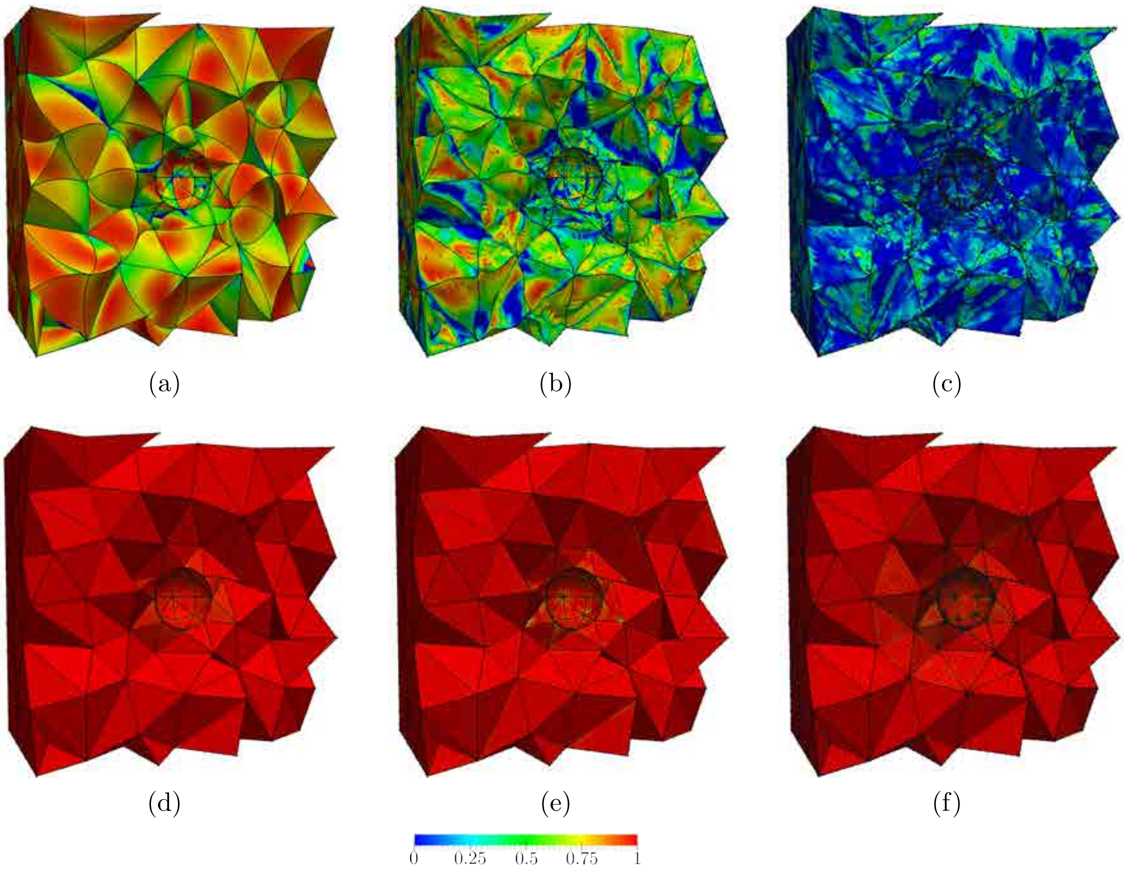

Figure 4.7: Initial and smoothed curved high-order meshes on a cube with a spherical cavity. Polynomial degrees: (a,d) 2, (b,e) 5 and (c,f) 10.

4.3.1 Robustness for high polynomial degrees

To illustrate the ability of our approach to untangle meshes which may contain a large number of inverted elements, we consider a cube of side length 5 with an spheric cavity of diameter 1 placed at the center of the cube. The initial isotropic linear mesh consists of 1441 elements. Next, we increase the polynomial degree of the elements to degrees 2, 5 and 10. We then curve the boundary faces to match the geometry. In order to test our approach, we randomly perturb the interior nodes obtaining meshes that have 373, 1333 and 1439 inverted elements, respectively (see Table 4.1). Finally, we apply our optimization procedure to obtain valid meshes for all cases. Figure 4.7 shows the initial meshes containing invalid elements and the final high-quality meshes for the different polynomial degrees. In Table 4.1 we summarize the element quality statistics for the initial and final meshes.

Table 4.1: Quality statistics for the meshes shown in Figure 4.7. The meshes are composed by 1441 elements, and 2327, 32382 and 249387 nodes, for polynomial degrees 2,5, and 10, respectively.

Mesh	Figure	Min	Max	Mean	Std. Dev.	#inv
Initial	4.7(a)	0.00	0.98	0.53	0.35	373
Smoothed	4.7(d)	0.96	1.00	1.00	0.01	0
Initial	4.7(b)	0.00	0.72	0.03	0.11	1333
Smoothed	4.7(e)	0.97	1.00	1.00	0.00	0
Initial	4.7(c)	0.00	0.21	0.00	0.01	1439
Smoothed	4.7(f)	0.96	1.00	1.00	0.01	0

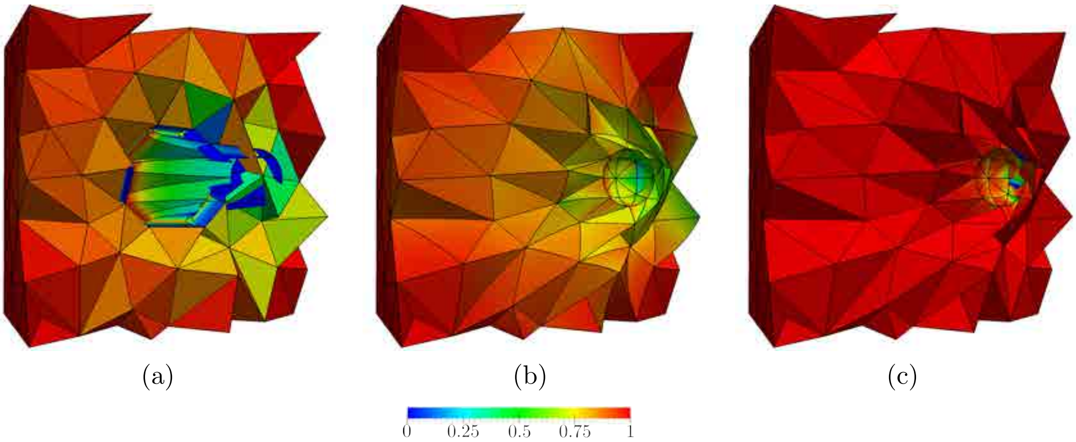

Figure 4.8: Meshes of polynomial degree 5 on a cube with a spherical cavity. (a) Initial curved mesh. (b) Mesh optimized with our objective function. (c) Mesh optimized with an objective function with constant Hessian.

Table 4.2: Quality statistics for the meshes of polynomial degree 5 shown in Figure 4.8. The meshes are composed of 1441 elements and 32382 nodes .

Formulation	Figure	Min	Max	Mean	Std. Dev.	#inv
Initial curved mesh	4.8(a)	0.00	1.00	0.83	0.28	134
Non-linear	4.8(b)	0.15	1.00	0.90	0.12	0
Linear (starting from 4.8(a))	-	0.00	1.01	0.91	0.27	110
Linear (starting from 4.8(b))	4.8(c)	0.00	1.00	0.99	0.09	15

In the next example, we illustrate the robustness of our approach to deal with large boundary deformations and non-convex geometries. We consider the valid curved mesh of polynomial degree five of the previous example and displace the sphere 1.5

Table 4.3: Quality statistics of a mesh of polynomial degree 2 for a SD7003 airfoil. The mesh is composed by 104522 elements and 146394 nodes.

Mesh	Figure	Min	Max	Mean	Std. Dev.	#inv
Initial	4.9(a)	0.00	1.00	0.96	0.05	130
Smoothed	4.9(b)	0.52	1.00	0.96	0.04	0

units towards the right boundary. The resulting mesh contains 134 invalid elements, see Figure 4.8(a). Using the proposed method, we are able to untangle this inverted configuration obtaining a valid mesh, see Figure 4.8(b). We compare our approach with a linear method obtained by imposing, for each element, that the Jacobian of the physical configuration is equal to the Jacobian of the initial configuration in a least-squares sense. Hence, the objective function in that case is:

$$f(\mathbf{x}_1, \ldots, \mathbf{x}_{n_F}; \mathbf{x}_{n_F+1}, \ldots, \mathbf{x}_{n_N}) = \|\mathbf{D}\phi_h - \mathbf{Id}\|^2. \tag{4.15}$$

This simpler formulation fails to generate a valid mesh when it starts from the tangled configuration presented in Figure 4.8(a). The fact that the linear approach is unable to handle inverted elements is further illustrated by the fact that starting from the valid mesh obtained by our non-linear method, see Figure 4.8(b), the linear method generates a non-valid mesh that contains 15 inverted elements, see Figure 4.8(c). The mesh quality statistics for this example considering the different objective functions in the optimization process are summarized in Table 4.2. We note that our proposed nonlinear least-squares approach combined with the ability to handle inverted elements is the only approach capable of consistently producing valid meshes.

4.3.2 Preservation of the features of the initial mesh including boundary layers

In this example, we illustrate how our approach preserves the features of the linear mesh such as a stretched boundary layer mesh, see Gargallo-Peiró et al. (2013b). We consider a linear boundary layer mesh for a SD7003 airfoil. We increase the order of the polynomial degree to 2. Next, we curve the boundary faces to match the geometry, see Figure 4.9(a). In Table 4.3 we observe that this initial mesh contains 130 tangled elements, all of them adjacent to the airfoil. Figure 4.9(c) shows a zoom of the inverted elements in the lower surface close to the leading edge. Figure 4.9(b) presents the

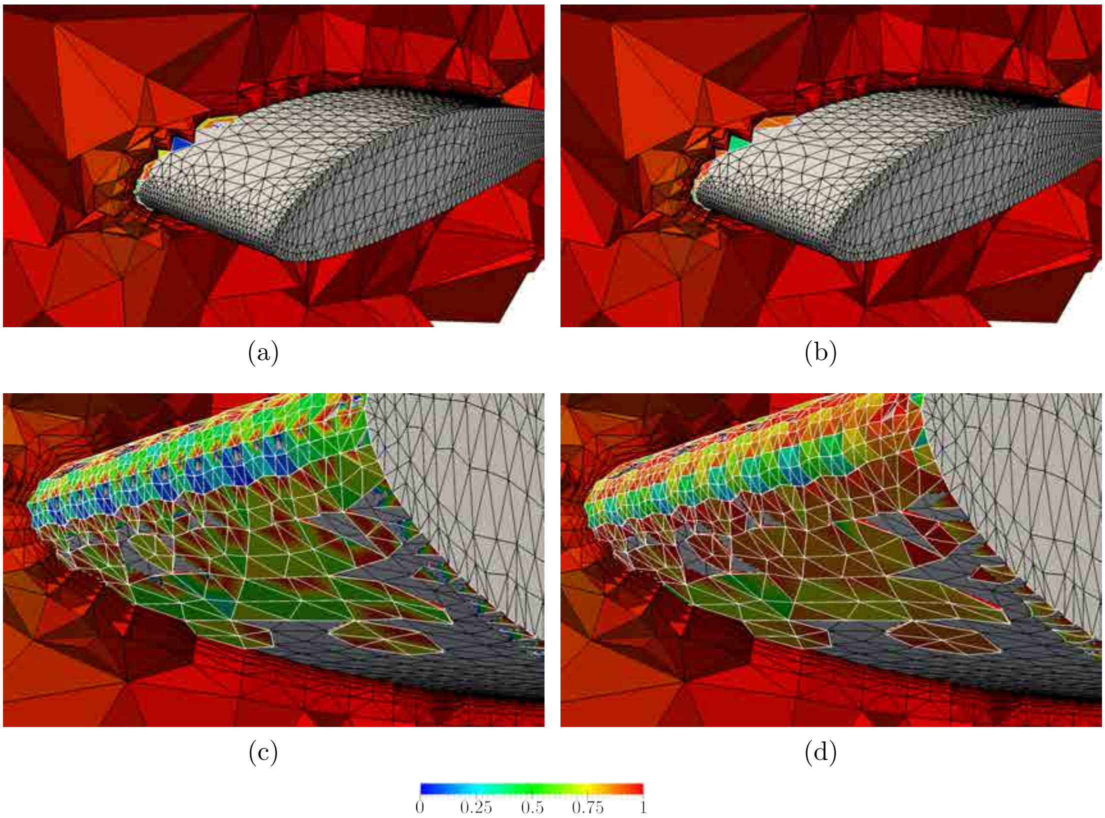

(a) (b)

(c) (d)

Figure 4.9: Tetrahedral meshes of polynomial degree 2 with boundary layer around a SD7003 airfoil. Initial curved high-order mesh (a) overview and (c) zoom. Final smoothed high-order mesh: (b) overview and (d) zoom. In these two figures we highlight with white edges the inverted high-order elements that appear in the initial curved high-order mesh.

final high-order mesh obtained by using the straight-sided high-order mesh as the initial configuration in our optimization process. All the inverted elements have been untangled and the final mesh presents a minimum quality of 0.52 and a mean value of 0.96, see Table 4.3. Figure 4.9(d) shows that the inverted elements in the leading edge have been untangled.

4.3.3 Preserving straight-sided elements and element size

In this example, we illustrate the capability of the proposed method to maintain the element size and shape prescribed on the ideal mesh. In addition, with this example we also show that our formulation can handle different ideal elements. To this end, we consider a cubic geometry of edge length 5 and we generate an isotropic linear mesh

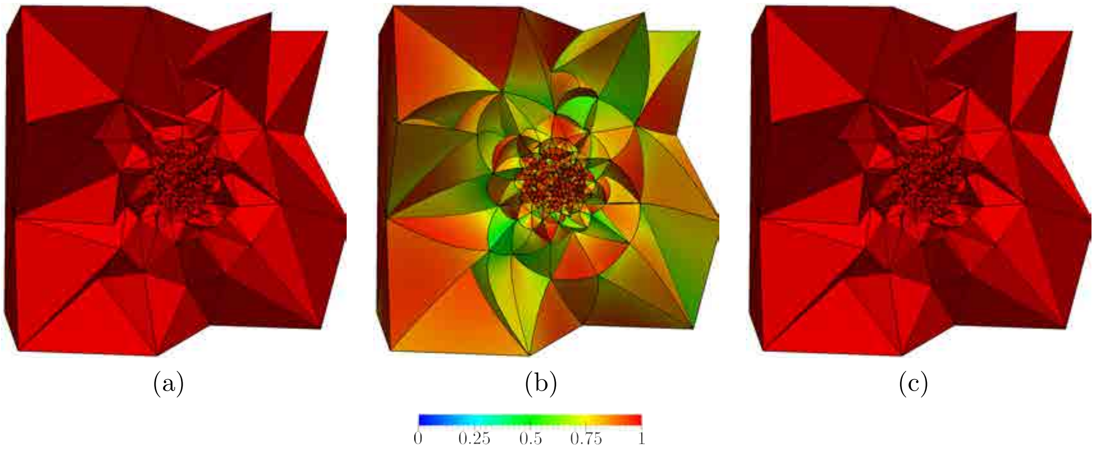

(a) (b) (c)

Figure 4.10: Meshes of polynomial degree five for a cube with non-constant element size. (a) Initial mesh, (b) mesh smoothed taking the equilateral high-order tetrahedron as ideal, and (c) mesh smoothed taking the straight-sided high-order mesh as ideal.

Table 4.4: Quality statistics of the meshes of polynomial degree 5 presented in Figure 4.10. The meshes are composed by 7394 elements and 79429 nodes.

Figure	Min	Max	Mean	Std. Dev.	#inv
4.10(a)	1.00	1.00	1.00	0.00	0
4.10(b)	0.40	1.00	0.86	0.10	0
4.10(c)	1.00	1.00	1.00	0.00	0

Table 4.5: Statistics of the scaled Jacobian values of the polynomial degree 5 meshes for the cubic domain.

Mesh	Figure	Min	Max	Mean	Std. Dev.	#inv
Equilateral tet.	4.10(b)	0.002	0.948	0.339	0.212	0
Straight-sided mesh	4.10(c)	0.990	1.000	0.990	0.001	0

using an element size field of 0.1 inside a spheric region of diameter 1 and an element size field of 2 on the outer boundary. Figure 4.10(a) presents the initial straight-sided high-order mesh. Then, we increase the polynomial degree of the elements to five. Note that after matching the boundary faces to the geometry, the resulting elements are still straight-sided since the contour of the geometry is planar.

Using the procedure presented in Section 4.1.3 we will optimize the high-order mesh using two different ideal elements. On the one hand, for each element, we select the equilateral tetrahedron as the ideal element. Figure 4.10(b) presents the optimized mesh. Note that a large number of elements with curved faces appear even if there are no curved boundaries in the domain. On the other hand, we select for each element its ideal configuration according to the straight-sided high-order mesh. Figure 4.10(c) shows the optimized mesh. Table 4.4 details the quality statistics of the new meshes. Note that the mesh optimized using the straight-sided mesh as ideal contains higher values of the minimum and mean quality values.

To quantify how the optimized meshes maintain the element size of the initial linear mesh we compute the relative error in the volume as:

$$r_v = \frac{|v_e - v_e^0|}{|v_e^0|},$$

for $e = 1, \ldots, n_E$, where v_e^0 and v_e are the volume of the e-th element in the initial and optimized meshes, respectively. It is important to point out that using the equilateral tetrahedron as the ideal element, the maximum value of the relative error, r_v is 2.013. Moreover, all the elements have a relative error in the volume bigger than 10^{-3}. On the contrary, if we use the straight-sided mesh as the ideal configuration, the maximum relative error is $2\ 10^{-3}$.

To check if an element is straight-sided we compute the scaled Jacobian measure

$$\mu = \frac{\min\limits_{\boldsymbol{\xi} \in E^M} \det \mathbf{D}\boldsymbol{\phi}_P(\boldsymbol{\xi})}{\max\limits_{\boldsymbol{\xi} \in E^M} \det \mathbf{D}\boldsymbol{\phi}_P(\boldsymbol{\xi})}$$

at the integration points of each element. Recall that if an element is affine to a linear element, then $\mu = 1$. Table 4.5 summarizes the statistics values for both meshes. We highlight that using the straight-sided mesh as ideal, we obtain 7387 elements with $\mu = 1$ (99% of the elements). However, if we select the equilateral tetrahedron as ideal, all the elements are curved (there are no elements with $\mu = 1$).

4.4 Concluding remarks

In this chapter, we have presented a robust method to smooth and untangle high-order meshes. Specifically, we propose a least-squares minimization of the regularized distortion measure for high-order meshes. We highlight that the robustness of the smoothing and untangling method emerges from the capabilities of the proposed optimization, namely: to repair invalid curved meshes (untangling), to transform valid configurations to valid configurations (consistency), to deal with any polynomial degree (high-order), and to preserve the geometrical features of the ideal mesh (size, stretching, straight-sided inner elements). Note that the untangling capability is the main advantage of the proposed method if we compare it with other consistent curving methods. Recall that to enable the consistency it is standard to use a non-linear measure of the point-wise distortion that penalizes non-positive determinants. However, this is not sufficient to guarantee that a method has the untangling capability.

Furthermore, for the presented method, one scalar parameter has to be chosen to determine the amount of relative regularization during the untangle procedure. To this end, we have empirically determined how to chose this scalar parameter. Moreover, we have detailed how to obtain, from this parameter and from the ideal mesh, an element-wise constant field that allows the regularization of the non-linear mesh distortion.

To test the robustness of the untangling capability, we have considered several examples. Specifically, we have seen that the method untangles meshes composed by a large number of invalid initial elements for: approximations up to degree ten, large deformations of the curved boundaries, concave boundaries, and highly stretched boundary layer elements. This robustness of the method is of practical importance, since after curving the mesh invalid high-order elements can appear close to the mesh boundaries.

Chapter 5

Validation and generation of high-order meshes on CAD surfaces

---

In the past recent years a growing interest for the use of high-order methods to solve partial differential equations has been awakened in the FEM community. The high-accuracy (Dey et al., 1997; Cockburn and Shu, 2002) and good convergence rates (Babuška and Guo, 1988, 1996) given by these methods has motivated an increase on their use. However, their application to industrial problems with complex geometries has been hampered by the difficulty to generate high-order discretizations. In particular, the issue of generating arbitrary high-order meshes for surfaces is still unresolved.

In 3D applications of high-order methods, the generation of high-quality meshes on the surfaces that conform the domain boundary is of the major importance. On the one hand, it has been evidenced that curved surface meshes can reduce the spurious effects that arise in the solution due to piece-wise linear approximation of the boundary of the domain in specific applications (Bassi and Rebay, 1997; Barth, 1998; Dey et al., 1997; Luo et al., 2002; Xue and Demkowicz, 2005; Sevilla et al., 2011). On the other hand, the quality of the volume mesh is limited by the quality of the surface mesh. If a boundary mesh face is inverted, the corresponding mesh element is inverted. Hence, to define high-quality 3D meshes it is mandatory to generate a high-quality curved surface mesh. Moreover, whereas interior volume nodes can move freely inside the container volumes, surface nodes can only move on the surface where they lie. Thus, to optimize a surface mesh, we require to involve the geometry representation in the optimization procedure. We highlight that several geometry representations can be used: triangular mesh, implicit entity, or CAD entities are the most common techniques. However, for industrial applications the CAD surface description is preferred, since CAD models are generated in the design process. Hence, in this work we focus on the generation of high-order meshes for CAD geometries.

The standard strategy to generate high-order meshes is an *a posteriori* procedure consisting on various steps (Dey et al., 2001a; Sherwin and Peiró, 2002; Shephard et al., 2005). First, a robust and automatic unstructured mesh generator is used to obtain an initial linear mesh. Second, the mesh is converted to high-order and is curved to fit the boundary geometry. In this step, tangled elements can appear. Since the boundary faces are forced to match the geometry, the determinant of the Jacobian can become zero, or auto-intersections of the element edges can be originated. Hence, it is necessary a final step where the position of the mesh nodes is optimized or the topology is modified to obtain a valid and high-quality mesh.

In this manner, the aim of this work is to generate valid and high-quality high-order meshes on parameterized CAD surfaces by means of an *a posteriori* procedure. We present three main contributions. First, we present a definition of distortion (quality) measure for nodal high-order meshes with the nodes on parameterized surfaces. The proposed measure quantifies the deviation between an ideal and a physical surface mesh, and is expressed in terms of the parametric coordinates of the mesh nodes. Moreover, this definition is independent of the selected surface parameterization.

Second, we derive a smoothing and untangling procedure for high-order meshes of any polynomial degree (high-order) on CAD surfaces. The proposed optimization approach is developed on the parametric space of the surface, ensuring that the nodes always lie on the exact CAD geometry. Moreover, it is capable to transform an invalid curved high-order mesh to a valid mesh (untangling). In addition, we prove that the optimization procedure is independent of the parameterization. Hence, the method is specially suited to generate high-order meshes on low-quality CAD parameterizations.

Finally, we propose an *a posteriori* curved mesh generation approach based on the proposed optimization technique. First, we generate a linear mesh. Second, we increase the polynomial degree of the elements and we curve them to match the geometry. And third, we optimize the location of the nodes to ensure that the mesh is valid.

The rest of the chapter is organized as follows. First, in Section 5.1 we present the scope of this work, the statement of the problem that we aim to solve, and the selected approach. Next, in Section 5.2, we set the framework for the definition of point-wise distortion measures for high-order elements on parameterized surfaces. In Section 5.3, we detail an smoothing and untangling procedure based on the minimization of the proposed distortion measures. Following, in Section 5.4 we use the point-wise measures to define a distortion (quality) measure for high-order elements on parameterized CAD surfaces. Finally, we present several examples to underline the main properties of the proposed optimization method and the derived nesh generation procedure, Section 5.5.

5.1 Problem statement and methodology

5.1.1 Input and output

Our input data is a linear mesh $\mathcal{M}^1_{\mathbf{x}}$ composed by elements with the nodes on a parameterized surface. We assume that the input linear mesh is valid and that it has elements of the desired shape and size for the target computation. In addition, we also assume that the surface Σ is parameterized by a continuously differentiable and invertible mapping

$$\begin{array}{rccc} \boldsymbol{\varphi}: & \mathcal{U} \subset \mathbb{R}^2 & \longrightarrow & \Sigma \subset \mathbb{R}^3 \\ & \mathbf{u} = (u, v) & \longmapsto & \mathbf{x} = \boldsymbol{\varphi}(\mathbf{u}), \end{array} \tag{5.1}$$

where $\mathcal{U}$ is the parametric space of the surface. In this work, we use OpenCASCADE library (CASCADE, 2012) to retrieve the parameterization of the surfaces from the CAD model.

The output data is a high-order mesh $\mathcal{M}^p_{\mathbf{x}}$ of polynomial degree p with all the nodes on the parameterized surface, and composed by valid elements (positive determinant of the Jacobian of the representation mapping) that have a shape close to the initial straight-sided linear elements.

5.1.2 Methodology

The proposed approach is composed by the following three steps.

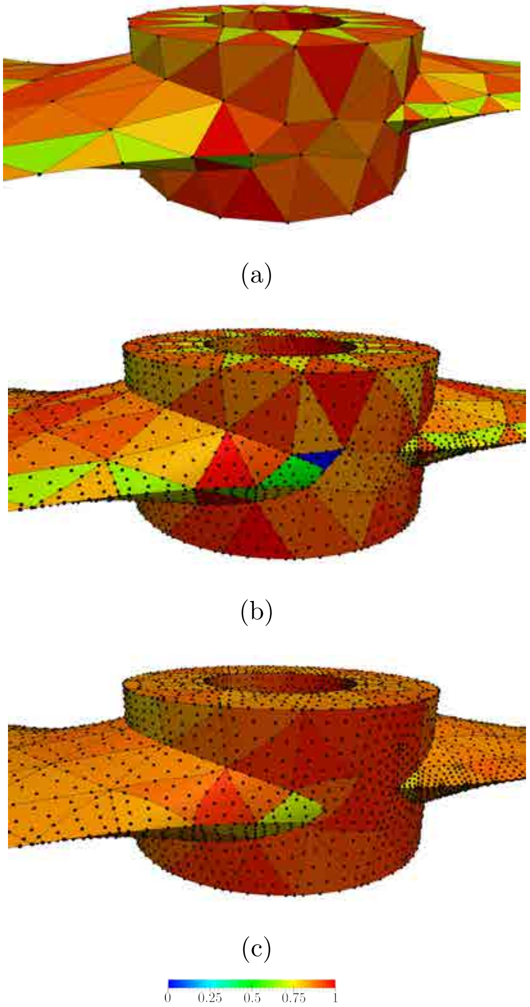
(a)

(b)

(c)

Figure 5.1: Process of the generation of a high-order mesh on a propeller: (a) linear mesh, (b) initial (invalid) curved mesh of polynomial degree five, and (c) optimized (valid) mesh of polynomial degree five.

1. *Generating the ideal mesh.*

   Using a robust and automatic linear surface mesh generator we create a mesh with elements of the desired size and shape. Our approach requires to know both the physical, $\mathcal{M}^1_{\mathbf{x}}$, and the parametric, $\mathcal{M}^1_{\mathbf{u}}$, coordinates of nodes of the initial linear surface mesh. There are two strategies to retrieve the parametric coordinates of the nodes. On the one hand, we can require that the linear mesh generator stores the parametric coordinates, see Roca et al. (2004, 2006). On the other hand, we can solve a non-linear problem to obtain the parametric coordinates of the closest point of the surface to each of the mesh nodes, see

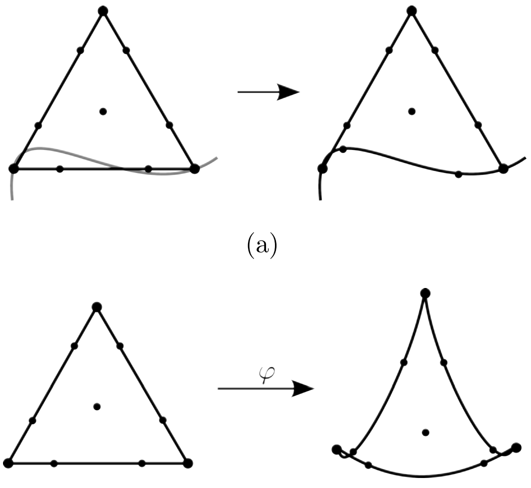

(a)

(b)

Figure 5.2: Possible tangling issues in the curving procedure: (a) element edge curving to fit the boundary geometry that creates an auto-intersection with an inner edge, and (b) anisometric parameterization that produces an invalid element on the physical space.

Roca (2009). In Figure 5.1(a) we show the linear mesh generated on a propeller. We have colored the mesh elements according to their shape quality taking as ideal element the equilateral triangle.

Next, we increase the polynomial degree of the mesh on the physical space and we set this straight-sided high-order mesh as the ideal configuration in our optimization procedure. Note that this mesh is of the desired polynomial degree, and, at the same time, has elements of the desired size and shape.

2. *Curving the mesh to match the geometry.*
   We define a distribution of nodes of degree p on the straight-sided elements on the parametric space. For elements adjacent to the surface boundary, we blend the boundary edge to fit the geometry curve. Next, we define a Legendre-Gauss-Lobatto distribution of the nodes (Warburton, 2006) along the edge using the arc parameter of the curve. Then, the inner nodes of the elements are redistributed by means of the blending presented in Warburton (2006). We name the mesh with nodes on the parametric space as initial parametric mesh, $\mathcal{M}_{\mathbf{u}}^{p,0}$. Afterwards, we map $\mathcal{M}_{\mathbf{u}}^{p,0}$ to the surface, obtaining an initial high-order physical mesh, $\mathcal{M}_{\mathbf{x}}^{p,0}$, see details in Roca et al. (2004, 2006).

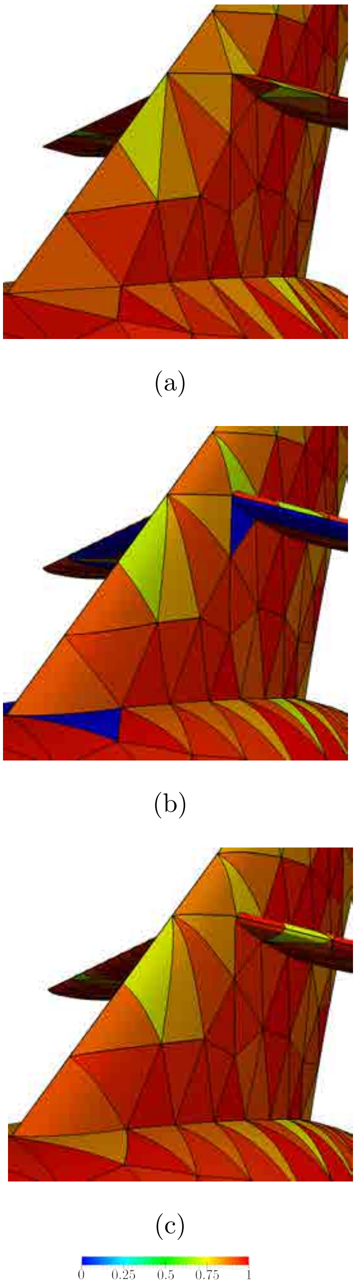

(a)

(b)

(c)

Figure 5.3: Process of the generation of a high-order mesh on the horizontal stabilizer of a falcon aircraft: (a) linear mesh, (b) initial (invalid) curved mesh of polynomial degree four, and (c) optimized (valid) mesh of polynomial degree four.

The high-order meshes obtained after these steps can contain tangled elements. For instance, Figure 5.1(b) shows a detail of the degree five mesh for the propeller with a tangled element colored in blue. These inverted elements appear due to two main issues. First, the *a posteriori* curving of the boundary edges to fit the geometry curves can lead to intersections between two element edges, see Figure 5.2(a). Second, a valid high-order distribution on the parametric space can be invalid once mapped onto the surface due to a low-quality parameterization, see Figure 5.2(b).

We highlight that these phenomena appear in real applications. Figure 5.3 shows the mesh generation process of a Falcon aircraft, close to the area of the horizontal stabilizer. In Figure 5.3(a) we observe the generated valid linear mesh. Next, Figure 5.3(b) shows the initial curved mesh of polynomial degree 4 where both types of tangling issues are observed. Finally, Figure 5.3(c) presents the mesh resulting from the optimization procedure that we will present in Section 5.3. We present further details of this example on Section 5.5.2.1.

3. *Optimizing the surface mesh.*
   We optimize (smooth and untangle) the node locations on the parametric space to repair the existent inversions and to improve the quality of the high-order elements on the surface. In this manner, we obtain a mesh $\mathcal{M}^p_{\mathbf{u}}$ on the parametric space that is valid and of high-quality on the physical surface. Next, by means of the surface parameterization $\boldsymbol{\varphi}$, we map the parametric mesh to the surface, $\mathcal{M}^p_{\mathbf{x}} = \boldsymbol{\varphi}(\mathcal{M}^p_{\mathbf{u}})$. In Figure 5.1(c) we show the final surface mesh, where all the elements are valid and high-quality. Comparing Figures 5.1(a) and 5.1(c) we realize that we have been able to obtain a valid and high-quality high-order mesh such that the shape of its elements is similar to the shape of the elements in the initial linear mesh. Analogously, in Figure 5.3(c) we show the final configuration for the horizontal stabilizer of the Falcon aircraft, composed by valid elements with similar shape than the straight-sided elements from Figure 5.3(a).

We point out that this work is devoted to the third step of the presented process. Specifically, we define a distortion measure to determine the validity of a high-order element on a parameterized surface, see Section 5.2.2, and we derive an optimization (smoothing and untangling) process in terms of the parametric coordinates of the nodes to improve the quality of the initial mesh, see Section 5.3.3. It is important to highlight that in this chapter we focus on nodal high-order triangular elements of degree p. However, changing the element shape functions in Section E, the same approach is applicable to high-order quadrilaterals.

5.2 Point-wise distortion measures for surfaces

In this section, we present a technique to define the distortion of a non-linear mapping between surfaces in $\mathbb{R}^3$. First, in Section 5.2.1, we propose a technique to extend the distortion measures for planar linear elements presented in Section 3.1.1 to quantify the distortion of mappings between pairs of vectors in $\mathbb{R}^3$. Second, in Section 5.2.2, we use the measures presented in Section 5.2.1 to define a point-wise distortion measure for non-linear deformations between surfaces.

5.2.1 Distortion measures for linear mappings between planes in 3D

Let $\Pi_a, \Pi_b \subset \mathbb{R}^3$ be two planes on $\mathbb{R}^3$, determined by two pairs of vectors $\mathbf{a}_1, \mathbf{a}_2 \in \Pi_a$ and $\mathbf{b}_1, \mathbf{b}_2 \in \Pi_b$, respectively. Let $\mathbf{J} : \Pi_a \subset \mathbb{R}^3 \rightarrow \Pi_b \subset \mathbb{R}^3$ be a linear mapping such that

$$\mathbf{b}_i = \mathbf{J}(\mathbf{a}_i), \qquad i = 1, 2.$$

The distortion measures for linear elements, presented in Section 3.1.1, are defined in the terms of a mapping between pairs of vectors in $\mathbb{R}^2$. However, linear surface meshes lead to planar elements immersed in $\mathbb{R}^3$ and therefore, distortion measures have to be defined in terms of a mapping between pairs of vectors in $\mathbb{R}^3$. Hence, the distortion measure for linear planar elements cannot be applied directly. To address this issue, the goal of this section is to determine a linear mapping $\bar{\mathbf{J}}$ in planar cartesian coordinates that has the same distortion as $\mathbf{J}$.

First, we obtain an orthonormal basis for Π_a by means of the Gram-Schmidt procedure. Specifically, we define

$$\begin{aligned}
\tilde{\mathbf{a}}_1 &:= \frac{\mathbf{a}_1}{\|\mathbf{a}_1\|}, \\
\tilde{\mathbf{a}}_2 &:= \gamma \, \frac{\mathbf{a}_2 - (\mathbf{a}_2^T \tilde{\mathbf{a}}_1)\, \tilde{\mathbf{a}}_1}{\|\mathbf{a}_2 - (\mathbf{a}_2^T \tilde{\mathbf{a}}_1)\, \tilde{\mathbf{a}}_1\|},
\end{aligned}$$

as the two orthonormal vectors of the new basis, where γ is defined to ensure a well oriented orthonormal basis. In particular, we set γ equal to ± 1, being 1 for counter-clockwise oriented vectors, and -1 for clockwise oriented ones.

Note that the 2×3 matrix $\tilde{\mathbf{A}}^T$, where $\tilde{\mathbf{A}} = [\tilde{\mathbf{a}}_1 \ \tilde{\mathbf{a}}_2]$, expresses $\mathbf{a}_i$ in the orthonormal basis $\tilde{\mathbf{a}}_i$. Analogously, we denote by $\tilde{\mathbf{b}}_1$ and $\tilde{\mathbf{b}}_2$ the two vectors of the orthonormal basis of Π_b, and $\tilde{\mathbf{B}} := [\tilde{\mathbf{b}}_1 \ \tilde{\mathbf{b}}_2]$. Therefore, $\tilde{\mathbf{B}}^T$ expresses $\mathbf{b}_i$ in the orthonormal basis $\tilde{\mathbf{b}}_i$.

Finally, we define the vectors

$$\bar{\mathbf{a}}_i \ := \ \tilde{\mathbf{A}}^T \mathbf{a}_i, \qquad i = 1, 2 \tag{5.2}$$

and

$$\bar{\mathbf{b}}_i \ := \ \tilde{\mathbf{B}}^T \mathbf{b}_i, \qquad i = 1, 2 \tag{5.3}$$

to determine in cartesian coordinates a linear mapping $\bar{\mathbf{J}}$ such that

$$\bar{\mathbf{b}}_i = \bar{\mathbf{J}} \bar{\mathbf{a}}_i, \qquad i = 1, 2. \tag{5.4}$$

Note that $\bar{\mathbf{J}}$ has the same distortion measure value as $\mathbf{J}$, since η_δ, see Equation (3.6), is invariant under rotation. To obtain the expression of the matrix $\bar{\mathbf{J}}$, we consider Equation (5.4) and we substitute $\bar{\mathbf{a}}_i$ and $\bar{\mathbf{b}}_i$ taking into account Equations (5.2) and (5.3):

$$\tilde{\mathbf{B}}^T \mathbf{b}_i = \bar{\mathbf{J}} \ \tilde{\mathbf{A}}^T \mathbf{a}_i.$$

In particular, defining $\mathbf{A} := [\mathbf{a}_1 \ \mathbf{a}_2]$, and $\mathbf{B} := [\mathbf{b}_1 \ \mathbf{b}_2]$, we have that

$$\tilde{\mathbf{B}}^T \mathbf{B} = \bar{\mathbf{J}} \ \tilde{\mathbf{A}}^T \mathbf{A}.$$

Since $\mathbf{a}_1$ and $\mathbf{a}_2$ define a plane Π_a, they are linearly independent and therefore, $\mathbf{A}$ is invertible. In addition, they determine the two linearly independent vectors $\bar{\mathbf{a}}_1$ and $\bar{\mathbf{a}}_2$ that lead to a non-invertible matrix $\tilde{\mathbf{A}}$. Thus, $\tilde{\mathbf{A}}^T \mathbf{A}$ is a 2×2 invertible matrix, and the matrix $\bar{\mathbf{J}}$ can be computed from $\mathbf{A}$ and $\mathbf{B}$ as

$$\bar{\mathbf{J}}(\mathbf{A}, \mathbf{B}) := \tilde{\mathbf{B}}^T \mathbf{B} \ (\tilde{\mathbf{A}}^T \mathbf{A})^{-1}. \tag{5.5}$$

In this manner, we define the distortion of the linear map $\mathbf{J}$ in terms of $\bar{\mathbf{J}}$ and of the regularized distortion measure for linear elements as $\eta_\delta(\bar{\mathbf{J}})$, Section 3.1.1,.

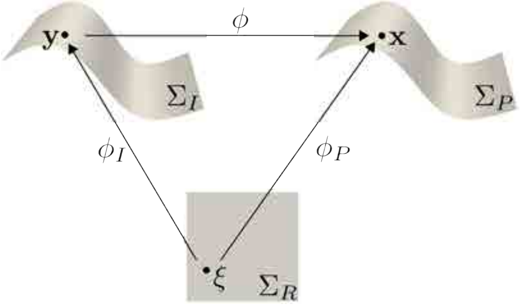

Figure 5.4: Mappings between the physical, ideal and reference surfaces.

5.2.2 Point-wise distortion measures for non-linear mappings

In this section, we define a measure of the distortion between two surfaces. We assume that we have an ideal surface $\Sigma_I \subset \mathbb{R}^3$ and a physical surface $\Sigma_P \subset \mathbb{R}^3$, that are diffeomorphic to the same planar domain $\Sigma_R \subset \mathbb{R}^2$. In particular, Σ_I and Σ_P are also diffeomorphic, and therefore, the physical surface can be defined as the image of a diffeomorphism ϕ from Σ_I to Σ_P, see Figure 5.4. We define the distortion between the surfaces in terms of the mapping ϕ. To determine the distortion measure $\mathrm{M}\phi$ for non-linear mappings ϕ between surfaces, we will pose M in terms of a given a distortion measure for linear elements η_δ.

We consider two diffeomorphisms between the reference surface, and the physical and ideal surfaces:

$$
\begin{aligned}
\phi_I &: \Sigma_R \subset \mathbb{R}^2 \longrightarrow \Sigma_I \subset \mathbb{R}^3, \\
\phi_P &: \Sigma_R \subset \mathbb{R}^2 \longrightarrow \Sigma_P \subset \mathbb{R}^3.
\end{aligned}
$$

Then, the diffeomorphism ϕ between the ideal and physical surfaces can be expressed as $\phi = \phi_P \circ \phi_I^{-1}$. In particular, ϕ is a non-linear mapping which Jacobian $\mathbf{J}(\mathbf{y}) := \mathbf{D}\phi(\mathbf{y})$ defines a linear mapping between the tangent space at a point $\mathbf{y}$ in Σ_I, and the tangent space at a point $\mathbf{x} = \phi(\mathbf{y})$ in Σ_P, see Figure 5.5. Next, using the applications

$$
\begin{aligned}
\mathbf{D}\phi_I &: \mathrm{T}_{\boldsymbol{\xi}}\Sigma_R \longrightarrow \mathrm{T}_{\mathbf{y}}\Sigma_I, \\
\mathbf{D}\phi_P &: \mathrm{T}_{\boldsymbol{\xi}}\Sigma_R \longrightarrow \mathrm{T}_{\mathbf{x}}\Sigma_P,
\end{aligned}
$$

we compute the expression of $\mathbf{J}$ on cartesian coordinates, $\bar{\mathbf{J}}(\mathbf{D}\phi_I, \mathbf{D}\phi_P)$, presented in Equation (5.5).

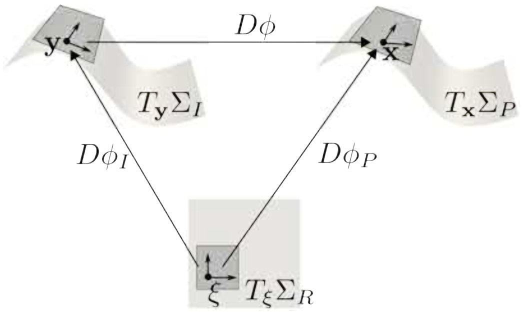

Figure 5.5: Mappings between the tangent spaces of the surfaces.

In this manner, we define the point-wise distortion for the non-linear mapping ϕ on a point $\mathbf{y}$ in Σ_I as:

$$\mathrm{M}\phi := \eta_\delta(\bar{\mathbf{J}}(\mathbf{D}\phi_I, \mathbf{D}\phi_P)). \tag{5.6}$$

Note that the distortion M for the non-linear mapping ϕ is casted to evaluate a distortion measure η_δ for linear mappings, see Equation (3.6). Therefore, it is well defined, since $\bar{\mathbf{J}}(\mathbf{D}\phi_I, \mathbf{D}\phi_P)$ defines a linear mapping for any $\mathbf{y}$ in Σ_I.

5.3 Generation of nodal high-order meshes on parameterized surfaces

In this section, we formulate an optimization problem to generate a valid curved high-order mesh by means of an *a posteriori* approach. First, we characterize the best diffeomorphism between two surfaces, Section 5.3.1. Next, we discretize the continuous characterization for the desired diffeomorphism, Section 5.3.2. Following, since our objective is to generate nodal high-order meshes on parameterized surfaces, we present the resulting optimization problem posed in terms of the parametric coordinates of the mesh nodes. Finally, in Section 5.3.4, we proof that the proposed distortion measure and the obtained objective function are independent of the surface parameterization.

5.3.1 Curving: globally defined smooth mapping

Fixed an ideal surface Σ_I and the boundary of the physical surface, $\partial\Sigma_P$, our goal is to find the best mapping, ϕ^* in $\mathcal{C}^1(\Sigma_I, \Sigma_P)$, between both surfaces according to

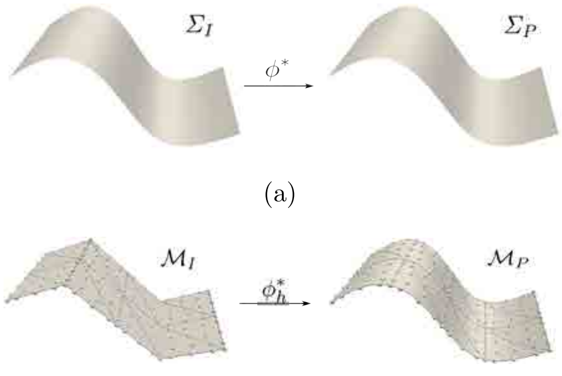

(a)

(b)

Figure 5.6: (a) Mapping between the ideal and physical surfaces. (b) Mapping between the ideal and physical meshes.

the distortion measure M, see Equation (5.6). Specifically, the ideal mapping ϕ^*, see Figure 5.6(a), would be a local diffeomorphism ϕ such that

$$\mathrm{M}\phi^* = 1, \quad \text{in } \Sigma_I, \tag{5.7}$$

$$\phi^* = g, \quad \text{on } \partial\Sigma_I, \tag{5.8}$$

where the boundary $\partial\Sigma_P$ is known and determined by the mapping g from $\partial\Sigma_I$ to $\partial\Sigma_P$.

5.3.2 Curving: element-wise defined smooth mapping

We consider that the surface Σ_I is approximated by the mesh $\mathcal{M}_I$, composed by the union of the ideal elements E_e^I, for $e = 1, \cdots, n_E$, where n_E is the number of elements of the mesh. Given the ideal mesh $\mathcal{M}_I$, we consider the space of vector functions on an ideal element E^I in $\mathcal{M}_I$,

$$\begin{aligned}\boldsymbol{\mathcal{W}}_{\boldsymbol{E^I}} := \Bigg\{ \mathbf{w} \in \left[\mathcal{P}^p(E^I)\right]^d \;\Bigg|\; \mathbf{w} = \sum_{i=1}^{n_p} \boldsymbol{\varphi}(\mathbf{u}_i) N_i(\mathbf{y}) \\ \text{for } \mathbf{u}_1, \ldots, \mathbf{u}_{n_p} \in \mathcal{U} \Bigg\}\end{aligned} \tag{5.9}$$

where $\mathcal{P}^p(E^I)$ is the space of polynomials of degree p on the element E^I, $\{N_i\}_{i=1,\ldots,n_p}$ are polynomial interpolative shape functions of degree p, and n_p is the number of element nodes. We point out that the elemental representation is selected to constrain the element nodes to the parameterized surface. Specifically, the physical nodes of an element, $\mathbf{x}_i$ in Σ_P, are expressed in terms of their parametric coordinates as $\mathbf{x}_i = \boldsymbol{\varphi}(\mathbf{u}_i)$, where $\mathbf{u}_i$ in $\mathcal{U}$, using the surface parameterization presented in Equation (5.1), see details in Appendix E. Hence, if we modify the parametric coordinates of a node $\mathbf{u}_i$, its physical location computed by the parameterization will always lie on the surface

Next, we consider the space of vector functions on the ideal mesh

$$\begin{aligned}\boldsymbol{\mathcal{W}} := \big\{\mathbf{w} \in \left[\mathcal{C}^0\left(\mathcal{M}\right)\right]^d \mid \\ \mathbf{w}_{|_{E^I}} \in \boldsymbol{\mathcal{W}}_{\boldsymbol{E^I}},\ \forall E^I \in \mathcal{M}_I\big\}.\end{aligned} \tag{5.10}$$

Fixed an ideal mesh $\mathcal{M}_I$, we seek the optimal mapping ϕ_h^* in $\boldsymbol{\mathcal{W}}$, see Figure 5.6(b), such that it is an element-wise local diffeomorphism for all E^I in $\mathcal{M}_I$ and it has an ideal distortion measure $\mathrm{M}\phi_h^*$. The best possible mapping ϕ_h^* can be characterized, in terms of the distortion $\mathrm{M}\phi_h^*$, as the element-wise diffeomorphism ϕ_h such that

$$\mathrm{M}\phi_h^* = 1, \qquad \text{in } \mathcal{M}_I, \tag{5.11}$$

$$\phi_h^* = g_h, \qquad \text{on } \partial\mathcal{M}_I, \tag{5.12}$$

where the curved boundary mesh $\partial\mathcal{M}_P$ is known and determined by the mapping g_h from $\partial\mathcal{M}_I$ to $\partial\mathcal{M}_P$.

Note that fixed $\mathcal{M}_I$ and determined $\partial\mathcal{M}_P$ in Equation (5.12), a mapping ϕ_h such that Equation (5.11) is verified may be, in general, not achievable. Therefore, this condition is imposed in a least-squares sense. That is, we seek ϕ_h^* in $\boldsymbol{\mathcal{W}}_{\boldsymbol{D}}$ such that

$$\phi_h^* \quad = \quad \underset{\phi_h \in \boldsymbol{\mathcal{W}}_{\boldsymbol{D}}}{\operatorname{argmin}} \, \|\mathrm{M}\phi_h - 1\|^2_{\mathcal{M}_I}, \tag{5.13}$$

where

$$\begin{aligned}\boldsymbol{\mathcal{W}}_{\boldsymbol{D}} := \{\phi_h \in \boldsymbol{\mathcal{W}} \mid \quad & (\mathrm{M}\phi_h - 1) \in \mathcal{L}^2(\mathcal{M}_I), \\ & \text{and } \phi_h = g_h \text{ on } \partial\mathcal{M}_I\}.\end{aligned}$$

In Equation (5.13), we define the norms

$$\|f\|_{\mathcal{M}_I} \quad := \quad \sqrt{\langle f, f\rangle_{\mathcal{M}_I}}, \tag{5.14}$$

$$\|f\|_{E^I} \quad := \quad \sqrt{\langle f, f\rangle_{E^I}}, \tag{5.15}$$

in terms of the inner product of two scalar functions on $\mathcal{M}_I$ as

$$\langle f, g\rangle_{\mathcal{M}_I} := \sum_{e=1}^{n_E} \langle f_{|_{E_e^I}}, g_{|_{E_e^I}}\rangle_{E_e^I}, \tag{5.16}$$

$$\langle f, g\rangle_{E^I} := \int_{E^I} f(\mathbf{x})\ g(\mathbf{x})\ \mathrm{d}\mathbf{x}. \tag{5.17}$$

Once ϕ_h^* is determined, we define the mesh $\mathcal{M}_P$ of the physical surface Σ_P as the image of $\mathcal{M}_I$ by ϕ_h^*. Each physical element can be obtained as:

$$E_e^P = \phi_h^*(E_e^I) \tag{5.18}$$

and we define the physical mesh as the union of the elements E_e^P, for $e = 1, \cdots, n_E$.

5.3.3 Curving: parametric nodal high-order mesh optimization

The minimization problem stated in Equation (5.13) can be rewritten in terms of elemental contributions. In particular, according to Equations (5.16) and (5.14) we seek ϕ_h^* in $\boldsymbol{\mathcal{W}_D}$ such that :

$$\begin{aligned}
\phi_h^* &= \underset{\phi_h \in \boldsymbol{\mathcal{W}_D}}{\operatorname{argmin}} \|\mathrm{M}\phi_h - 1\|^2_{\mathcal{M}_I} \\
&= \underset{\phi_h \in \boldsymbol{\mathcal{W}_D}}{\operatorname{argmin}} \sum_{e=1}^{n_E} \|\mathrm{M}\boldsymbol{\phi}_{h_{|_{E_e^I}}} - 1\|^2_{E_e^I} \\
&= \underset{\phi_h \in \boldsymbol{\mathcal{W}_D}}{\operatorname{argmin}} \sum_{e=1}^{n_E} \|\mathrm{M}\boldsymbol{\phi}_{E_e} - 1\|^2_{E_e^I}.
\end{aligned} \tag{5.19}$$

where $\boldsymbol{\phi}_{E_e} := \boldsymbol{\phi}_{h_{|_{E_e^I}}}$ is the mapping between E_e^I and its physical element E_e^P, see Equation (E.4) in Appendix E, as:

$$\boldsymbol{\phi}_{E_e}(\mathbf{y}; \mathbf{u}_{e,1}, \ldots, \mathbf{u}_{e,n_p}) = \sum_{i=1}^{n_p} \boldsymbol{\varphi}(\mathbf{u}_i) N_i(\mathbf{y}),$$

being $\mathbf{u}_{e,1}, \ldots, \mathbf{u}_{e,n_p}$ the parametric coordinates of the nodes of element E_e^P. Thus, the distortion measure at a point $\mathbf{y}$ of an element E_e^I of $\mathcal{M}_I$ can be written as:

$$\mathrm{M}\boldsymbol{\phi}_{E_e}(\mathbf{y}) = \mathrm{M}\boldsymbol{\phi}_{E_e}(\mathbf{y}; \mathbf{u}_{e,1}, \ldots, \mathbf{u}_{e,n_p}), \tag{5.20}$$

where the pairs (e, j) in $\mathbf{u}_{e,j}$ identify the local j-th node of element e with their global mesh number i. That is, for nodal high-order elements, determining ϕ_h^* in the minimization presented in Equation (5.19), is equivalent to determining the configuration of the nodes of the high-order mesh. Moreover, the element contribution to the objective function only depends on the nodes of that element.

According to the reasoning above, the optimization problem presented in Equation (5.19) can be expressed in such a manner that the nodal parametric coordinates are the unknowns of the problem (free nodes). To this end, we reorder the coordinates of the nodes, $\mathbf{u}_i$, selecting $i = 1, \ldots, n_F$ as the indexes corresponding to the inner nodes, and $i = n_F + 1, \ldots, n_N$ as the indexes corresponding to the fixed nodes (nodes on the edges of the CAD surfaces). Note that the coordinates of the fixed nodes are determined by the function g_h, and have been computed using the arc-parameter of the corresponding curve of the CAD geometry. Defining

$$f(\mathbf{u}_1, \ldots, \mathbf{u}_{n_F}; \mathbf{u}_{n_F+1}, \ldots, \mathbf{u}_{n_N}) := \frac{1}{2} \|\mathrm{M}\phi_h - 1\|^2_{\mathcal{M}_I}, \tag{5.21}$$

we can formulate the mesh optimization problem as finding $\{\mathbf{u}_1^*, \ldots, \mathbf{u}_{n_F}^*\}$ in $\mathcal{U} \subset \mathbb{R}^2$ such that:

$$\begin{aligned} \{\mathbf{u}_1^*, \ldots, \mathbf{u}_{n_F}^*\} = \underset{\mathbf{u}_1,\ldots,\mathbf{u}_{n_F} \in \mathbb{R}^3}{\operatorname{argmin}} \; & f(\mathbf{u}_1, \ldots, \mathbf{u}_{n_F}; \\ & \mathbf{u}_{n_F+1}, \ldots, \mathbf{u}_{n_N}), \end{aligned} \tag{5.22}$$

where $\mathbf{u}_i = \boldsymbol{\varphi}^{-1}(g(\mathbf{y}_i))$ for $i = n_F + 1, \ldots, n_N$. In Appendix B we detail our approach to solve the global minimization problem stated in Equation (5.22).

Note that the optimal configuration is found between the candidates for the minimization presented in Equation (5.22). The candidates are the critical coordinates $(\mathbf{u}_1, \ldots, \mathbf{u}_{n_F})$ of f. They are characterized by

$$\frac{\partial f}{\partial \mathbf{u}_i}(\mathbf{u}_1, \ldots, \mathbf{u}_{n_F}; \mathbf{u}_{n_F+1}, \ldots, \mathbf{u}_{n_N}) = 0 \qquad i = 1, \ldots, n_F. \tag{5.23}$$

5.3.4 Independence on the surface parameterization

In this section, we first prove that the defined point-wise measure is independent of the surface parameterization.

Proposition 5.1 (Independence on the parameterization)**.** *Let* $\boldsymbol{\varphi}_1 : \mathcal{U}_1 \to \Sigma_P$ *and* $\boldsymbol{\varphi}_2 : \mathcal{U}_2 \to \Sigma_P$ *be two different diffeomorphic parameterizations of* Σ_P*. Let* $\mathcal{M}$ *be a mesh on* Σ_P*, and* E^P *an element with nodes on the surface. Then, the point-wise distortion measure* M*, presented in Equation* (5.6)*, is independent of the surface parameterization.*

Proof. Each parameterization $j = 1, 2$ defines a different function space $\boldsymbol{\mathcal{W}}^j$, see Equation (5.10). In particular, for each parameterization $j = 1, 2$, it exists a set of nodal parametric coordinates $\mathbf{u}^j_{i=1,\dots,n_p}$ in $\mathcal{U}_j$, according to Equation (E.4), that we can write two different mappings $\boldsymbol{\phi}^j_E$ in $\boldsymbol{\mathcal{W}}^j_{\boldsymbol{E^I}}$, see Equation (5.9):

$$\boldsymbol{\phi}^j_E(\mathbf{y}) = \sum_{i=1}^{n_p} \boldsymbol{\varphi}_j(\mathbf{u}^j_i) N_i(\mathbf{y}), \quad \mathbf{y} \in E^I, \quad j = 1, 2.$$

Since both parameterizations are diffeomorphisms, we can write the element nodes $\mathbf{x}_1, \dots, \mathbf{x}_{n_p}$ of an element E^P as

$$\mathbf{x}_i = \boldsymbol{\varphi}_1(\mathbf{u}^1_i) = \boldsymbol{\varphi}_2(\mathbf{u}^2_i)$$

for unique $\mathbf{u}^j_i$ in $\mathcal{U}_j$, $j = 1, 2$, $i = 1, \dots, n_p$. Moreover, in any point $\mathbf{y}$ in E^I:

$$\begin{aligned} \boldsymbol{\phi}^1_E(\mathbf{y}) &= \sum_{i=1}^{n_p} \boldsymbol{\varphi}_1(\mathbf{u}^1_i) N_i(\mathbf{y}) \\ &= \sum_{i=1}^{n_p} \mathbf{x}_i N_i(\mathbf{y}) \\ &= \sum_{i=1}^{n_p} \boldsymbol{\varphi}_2(\mathbf{u}^2_i) N_i(\mathbf{y}) = \boldsymbol{\phi}^2_E(\mathbf{y}). \end{aligned} \tag{5.24}$$

Note that $\boldsymbol{\phi}^j_E$ is $\boldsymbol{\phi}^j_P \circ (\boldsymbol{\phi}^j_I)^{-1}$, see Appendix E. Analogously to Equation (5.24), the mappings $\boldsymbol{\phi}^j_I$ and $\boldsymbol{\phi}^j_P$ (between the master and the ideal and physical triangles, respectively) are independent of the CAD parameterization. Next, we denote by M_j the point-wise distortion measure defined using the space $\boldsymbol{\mathcal{W}}^j_{\boldsymbol{E^I}}$. Note that M_j is strictly determined from $\mathbf{D}\boldsymbol{\phi}^j_I$ and $\mathbf{D}\boldsymbol{\phi}^j_P$, see Equation (5.6). Moreover, since $\boldsymbol{\phi}^j_I$ and $\boldsymbol{\phi}^j_P$ are independent on the parameterization, so their Jacobians are. Therefore, from Eqs. (5.6) and (5.20),

$$\mathrm{M}_1 \boldsymbol{\phi}^1_E(\mathbf{y}; \mathbf{u}^1_1, \dots, \mathbf{u}^1_{n_p}) \;=\; \mathrm{M}_2 \boldsymbol{\phi}^2_E(\mathbf{y}; \mathbf{u}^2_1, \dots, \mathbf{u}^2_{n_p}).$$

Thus, the distortion at a point $\mathbf{y} \in E^I$ is independent of the selected surface parameterization.

□

Second, since the conditions imposed for the optimization procedure in Equation (5.23) are expressed in terms of M, which is independent of the surface parameterization, we can proof the following result:

Proposition 5.2. *According to the objective function f, defined in Equation* (5.22)*, the optimal location for the mesh nodes $\mathbf{x}_i = \boldsymbol{\varphi}(\mathbf{u}_i)$ in Σ, $i = 1, \ldots, n_F$, is independent of the surface parameterization.*

Proof. The conditions for the critical points of f are expressed in terms of M and its derivatives, Equation (5.23). Since M is independent of the surface parameterization, Proposition 5.1, the critical points of f are also independent of the surface mesh parameterization. To finalize, the optimal configurations are also independent of the surface parameterization, since they are found between the candidate configurations. □

Remark 5.1. *In Proposition 5.2, we have proved that the candidate configurations are independent of the surface parameterization. In particular, the candidate configurations have to be the same for high (smooth Jacobian) and low (highly varying Jacobian) quality surface parameterizations. Therefore, the proposed method can be applied to obtain candidate mesh configurations on CAD surfaces represented by low-quality parameterizations.*

Remark 5.2. *The goal of the proposed method is to obtain the critical points independently of the surface parameterization. However, there are meshes that cannot be untangled by the proposed method, such as when the boundary edges of the mesh present self-intersections. Nevertheless, the proposed method has properly smoothed and untangled all the tested meshes with valid boundary configurations.*

5.4 Distortion and quality measures for high-order elements on surfaces

To validate the suitability of a given surface mesh for computational purposes, in this section, we use the point-wise distortion measure presented in Equation (5.6) to propose a definition of distortion (quality) for high-order elements.

Definition 5.1. The *distortion measure for a high-order surface element* is

$$\eta_{\mathcal{U}}^{E} := \frac{\|\mathrm{M}\boldsymbol{\phi}_E\|_{E^I}}{\|1\|_{E^I}}, \tag{5.25}$$

where η_E is a function of the element nodes $\mathbf{u}_1, \ldots, \mathbf{u}_{n_p}$, since $\mathrm{M}\boldsymbol{\phi}_E$ is. Note that $\|1\|_{E^I}$ is the area of the ideal element.

Definition 5.2. The *quality measure for a high-order surface element* is

$$q_{\mathcal{U}}^{E} := \frac{1}{\eta_{\mathcal{U}}^{E}}. \tag{5.26}$$

Remark 5.3. *Since* $\eta_{\mathcal{U}}^{E}$ *is defined in terms of* $\mathrm{M}\boldsymbol{\phi}_E$*, it is also independent of the selected surface parameterization. Analogously, the corresponding quality measure* $q_{\mathcal{U}}^{E}$ *is also independent.*

We highlight that to check that the mesh is valid to perform a numerical simulation, a quality measure has to properly detect if an element it is non-valid (and assign 0 value). Moreover, the measure has to penalize the deviation of the element with respect to the target ideal (and assign value 1 to the ideal). In Appendix F we illustrate the behavior of the defined distortion and quality measures for high-order elements on parametrized surfaces.

Herein, when we validate a given curved high-order surface mesh, we set δ to 0 in Equation (5.6). Therefore, if there is a region where the Jacobian is non-positive ($\sigma \leq 0$), then η_E, Equation (5.25), is not defined and the quality $q_{\mathcal{U}}^{E}$ is 0. Conversely, if the physical element is the ideal, $\boldsymbol{\phi}_E$ is the identity. Then, the point-wise distortion $\mathrm{M}\boldsymbol{\phi}_E(\mathbf{y})$ is 1 for all $\mathbf{y} \in E^I$. Thus, by Definition 5.1, the element distortion η_E is also 1. Summarizing, we state the following remark:

Remark 5.4. *The distortion measure* $\eta_{\mathcal{U}}^{E}$ *for high-order surface elements has image* $[1, \infty)$*, where 1 corresponds to the ideal configuration and* ∞ *to a non-valid one. Hence, by Definition 5.2,* $q_{\mathcal{U}}^{E}$ *has image* $[0, 1]$*, where 0 corresponds to an invalid element, and 1 to the ideal one.*

5.5 Results

This section is divided in two parts. First, we present three examples to assess the properties of the proposed smoothing and untangling procedure for nodal high-order meshes with the nodes on CAD geometries. Second, we present three additional examples to illustrate the proposed mesh *a posteriori* mesh generation approach for CAD geometries.

We highlight that, in all the figures, the mesh elements are colored according to the quality measure presented in Definition 5.2. Moreover, for all the examples we

Mesh	Min	Max	Mean	SD	Tang.
Initial	0.00	1.00	0.98	0.11	6
Figure 5.7(a)	0.96	1.00	0.99	0.01	0
Figure 5.7(b)	0.96	1.00	0.99	0.01	0

Table 5.1: Shape quality statistics for the high-order meshes on a component of a motorbike brake, presented in Figure 5.7.

present a table summarizing the quality statistics of the mesh elements. Specifically, we provide: the minimum, the maximum, the mean and the standard deviation (SD) of the mesh quality, and the number of tangled elements. We highlight that in all cases, the smoothed mesh increases the minimum and mean values of the mesh quality and decreases its standard deviation. In all the examples, the resulting high-order elements are valid and curved, and we ensure that the nodes lie on the exact CAD geometry.

5.5.1 Properties

In this section, we present three examples to illustrate the main properties of the defined quality measure and the derived optimization process, namely: consistency, independence on the surface parameterization, and robustness of the untangling procedure.

5.5.1.1 Consistency

The goal of this example is to illustrate that the defined measure for high-order meshes on parameterized surfaces, see Equation (5.6), when applied to planar surfaces is equivalent to the high-order measure for planar meshes, presented in Roca et al. (2012). The planar point-wise distortion is expressed as:

$$\eta_{\mathbb{R}^2} := \eta(\mathbf{D}\boldsymbol{\phi}_E), \tag{5.27}$$

since it does not require the embedding of the Jacobian required in the definition of the surface measure in Section 5.2.2. That is, we show that Equation (5.6) is consistent with Equation (5.27) when the surface is planar. It is important to point out that this is true by construction. If the considered surface is planar, the matrix $\bar{\mathbf{J}}$, Equation (5.5), required to compute the value of the quality measure, corresponds to the matrix $\mathbf{J}$ except by a rotation. Note that we define the high-order measures

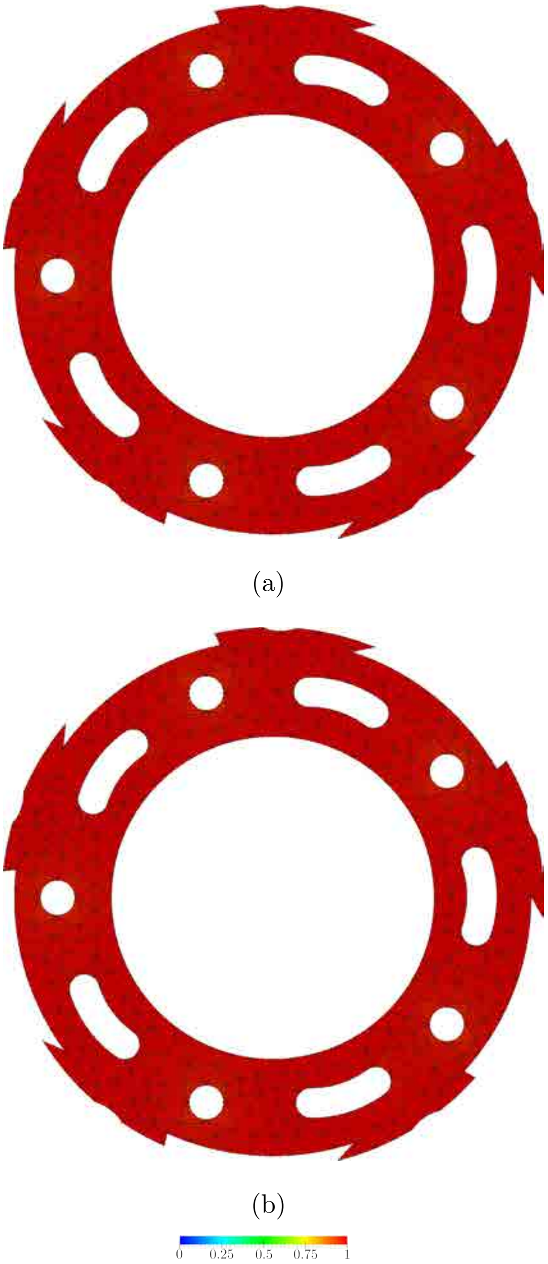
(a)

(b)

Figure 5.7: Optimization of a planar mesh of degree 3 for a component of a motorbike brake using: (a) the planar technique, and (b) the surface technique.

in terms of Jacobian distortion measures that are invariant under rigid body motion (such as the shape measure, see details in Knupp (2001a)). Therefore, we have that $\eta_{\mathcal{U}}^{E}$ is equal to η_E.

To illustrate this consistency, we consider a planar CAD model of a component of

Srf.	Figure	Min.Q.	Max.Q.	Mean Q.	SD	Tang.
$\varphi^1_{\Sigma_1}$	5.8(b)	0.29	0.96	0.67	0.18	0
	5.8(d)	1.00	1.00	1.00	0.00	0
$\varphi^1_{\Sigma_2}$	5.8(f)	0.43	1.00	0.65	0.16	0
	5.8(h)	1.00	1.00	1.00	0.00	0
$\varphi^1_{\Sigma_2}$	5.8(j)	0.16	0.93	0.57	0.22	0
	5.8(l)	0.91	1.00	0.97	0.02	0
$\varphi^2_{\Sigma_2}$	5.8(n)	0.34	0.96	0.63	0.16	0
	5.8(p)	0.91	1.00	0.97	0.02	0

Table 5.2: Shape quality statistics of the meshes on Σ_1 and Σ_2, presented in Figure 5.8.

a motorbike brake, see Figure 5.7. First, we generate a mesh composed by 643 elements of degree 3 and 5608 nodes. When the mesh is curved to match the boundary geometry, 8 tangled elements appear. Then, we optimize it using the planar, Figure 5.7(a), and the surface, Figure 5.7(b), distortion measures. Note that the ideal triangle for each element has been selected as the straight-sided high-order element itself in the initial configuration. To check that we obtain equivalent meshes, we compute

$$E = \max_{i=1,\ldots,n_F} \frac{\|\mathbf{x}_i^1 - \mathbf{x}_i^2\|}{L} \tag{5.28}$$

where L is the minimum edge length in the mesh, and $\mathbf{x}_i^1$ and $\mathbf{x}_i^2$ are the coordinates of the free nodes obtained by the planar and the surface measures, respectively. We obtain that $E = 1.3 \cdot 10^{-4}$ and hence, the meshes are equal up to minimization tolerance. Moreover, according to Table 5.1, we obtain the same quality statistics for both meshes.

5.5.1.2 Independence on the parameterization

The aim of this example is to show that the proposed quality measure and the derived optimization procedure are independent of the surface parameterization, see Section 5.3.4. To illustrate this property, we consider two surfaces, and for each one we define two different parameterizations. For both surfaces, Figure 5.8 presents the meshes on the parametric space (first and third columns) and on the physical space (second and fourth columns). We generate the same parametric mesh for all surfaces and parameterizations. The mesh is structured and composed by 128 elements of degree 3 and 625 nodes. Since we are using structured meshes, we select as ideal element

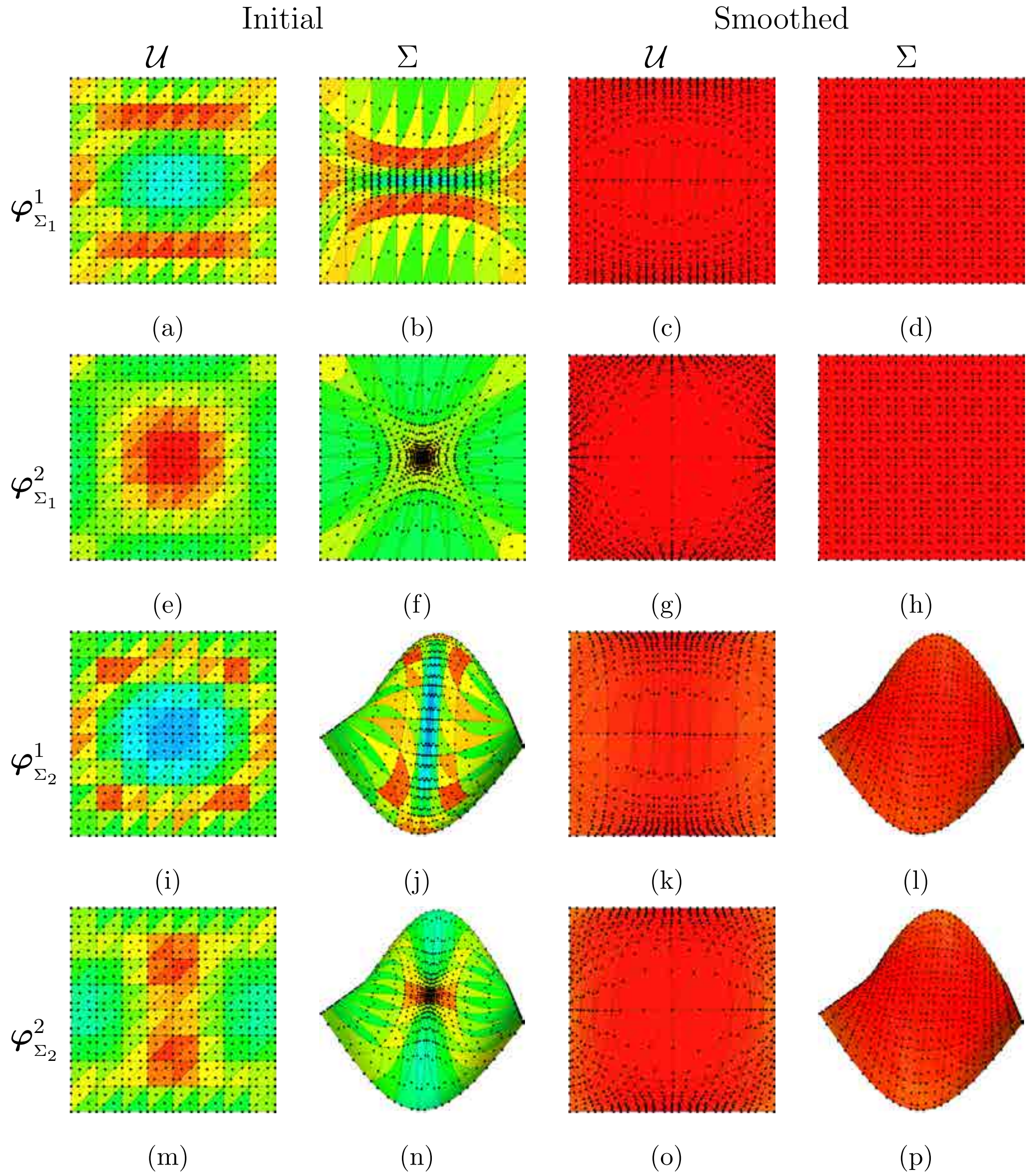

Figure 5.8: Independence of the optimization procedure on the surface parameterization. Degree three meshes on Σ_1 parameterized by $\boldsymbol{\varphi}^1_{\Sigma_1}$: (a,b) initial meshes on $\mathcal{U}^1_{\Sigma_1}$ and on Σ_1; (c,d) smoothed meshes on $\mathcal{U}^1_{\Sigma_1}$ and on Σ_1. Degree three meshes on Σ_1 parameterized by $\boldsymbol{\varphi}^2_{\Sigma_1}$: (e,f) initial meshes; (g,h) smoothed meshes. Degree three meshes on Σ_2 parameterized by $\boldsymbol{\varphi}^1_{\Sigma_2}$: (i,j) initial meshes; (k,l) smoothed meshes. Degree three meshes on Σ_2 parameterized by $\boldsymbol{\varphi}^2_{\Sigma_2}$: (m,n) initial meshes; (o,p) smoothed meshes.

the isosceles rectangle triangle. All meshes in Figure 5.8 are colored according to the shape quality of the elements on the physical space.

5.5.1.2.1 Surface 1 Given the parameterization

$$\begin{aligned} \boldsymbol{\varphi}_{\Sigma_1} : \mathcal{U}_{\Sigma_1} = [-1,1]^2 \subset \mathbb{R}^2 &\longrightarrow \mathbb{R}^3 \\ (u,v) &\longrightarrow (u,v,0), \end{aligned}$$

we define the surface Σ_1 as $\boldsymbol{\varphi}_{\Sigma_1}(\mathcal{U}_{\Sigma_1})$. Note that this parameterization has a constant Jacobian. We define two different parameterizations for Σ_1:

$$\begin{aligned} \boldsymbol{\varphi}^1_{\Sigma_1} : \mathcal{U}^1_{\Sigma_1} = [-1,1]^2 &\longrightarrow \Sigma_1 \subset \mathbb{R}^3 \\ (u,v) &\longrightarrow (u, v\ \epsilon(u,v), 0), \end{aligned} \tag{5.29}$$

and

$$\begin{aligned} \boldsymbol{\varphi}^2_{\Sigma_1} : \mathcal{U}^2_{\Sigma_1} = [-1,1]^2 &\longrightarrow \Sigma_1 \subset \mathbb{R}^3 \\ (u,v) &\longrightarrow (u\ \epsilon(u,v), v\ \epsilon(u,v), 0), \end{aligned} \tag{5.30}$$

where $\epsilon(u,v) := e^{-2(1-u^2)(1-v^2)}$. Note that these parameterizations have a non-constant Jacobian.

The elements of the initial mesh on the parametric space are rectangular isosceles triangles (see Figures 5.8(a) and 5.8(e)). These meshes are mapped to the physical space according to $\boldsymbol{\varphi}^1_{\Sigma_1}$ and $\boldsymbol{\varphi}^2_{\Sigma_1}$ respectively, see Figures 5.8(b) and 5.8(f). Therefore, the initial meshes on the physical space follow approximately the isolines of the corresponding parameterization. Note that both meshes contain low-quality elements due to the use of parameterizations with varying Jacobian matrices. Figures 5.8(c) and 5.8(g) show the optimized meshes in the parametric domain, and Figures 5.8(d) and 5.8(h) show the optimized meshes on the surface. We quantify if both optimized meshes are equal to each other using Equation (5.28) and we obtain $E = 1.01 \cdot 10^{-4}$. Hence, both meshes are equal up to minimization tolerance.

5.5.1.2.2 Surface 2 Given the parameterization

$$\begin{aligned} \boldsymbol{\varphi}_{\Sigma_2} : \mathcal{U}_{\Sigma_2} = [-1,1]^2 \subset \mathbb{R}^2 &\longrightarrow \mathbb{R}^3 \\ (u,v) &\longrightarrow (u,v,\sin(\pi u)\cos(\pi u)). \end{aligned}$$

we define the surface Σ_2 as $\boldsymbol{\varphi}_{\Sigma_2}(\mathcal{U}_{\Sigma_2})$. We define two different parameterizations for Σ_2:

$$\boldsymbol{\varphi}^1_{\Sigma_2}(u,v) := (u, v\ \epsilon(u,v), \sin(\pi u)\ \cos(\pi v\ \epsilon(u,v)))\,,$$

and

$$\begin{aligned}\boldsymbol{\varphi}^2_{\Sigma_2}(u,v) := \quad & (u\ \epsilon(u,v), v\ \epsilon(u,v),\\ & \sin(\pi u\ \epsilon(u,v))\ \cos(\pi v\ \epsilon(u,v))).\end{aligned}$$

In Figures 5.8(i) and 5.8(m) we present the structured parametric meshes. The image of these meshes on the surface is presented in Figures 5.8(j) and 5.8(n). Again, the parameterizations lead to low quality meshes on the physical surface. The optimized meshes on the parametric surface are shown in Figures 5.8(k) and 5.8(o), and on the physical surface in Figures 5.8(l) and 5.8(p). Although in this case we have a non-planar surface, the smoothing-untangling procedure also provides the same meshes up to minimization tolerance with $E = 5.7 \cdot 10^{-4}$.

Table 5.2 presents the quality statistics for both surface meshes. The optimization procedure can smooth the initial meshes and obtain a high-quality mesh, increasing significantly in both cases the minimum value of the quality.

5.5.1.3 Robustness of the smoothing and untangling procedure

The goal of this example is to illustrate the capability of the developed procedure to simultaneously untangle and smooth a high-order mesh with a large number of tangled elements. We consider a CAD geometry of a propeller and, according to Section 5.1, we generate an initial mesh of degree five composed by 1374 elements and 18343 nodes. This non-smoothed mesh contains 2 tangled elements, and therefore, is not valid for computational purposes. Figures 5.9(a) shows a general view of the initial curved high-order mesh, and Figure 5.9(d) shows a zoom where a tangled element appears. Recall that using the *a posteriori* curving approach detailed in Section 5.1, we normally obtain meshes with several tangled elements when the boundary is curved to match the geometry. These elements are usually located on the boundaries of the surface and therefore, the number of tangled elements is small compared to the total number of elements.

To check the capabilities of the proposed method, we increase the number of tangled elements by applying a random perturbation to the location of the inner nodes of the surface. The resulting mesh contains 1372 tangled elements, see Figures 5.9(b) and 5.9(e). After applying the optimization procedure we obtain a high-quality mesh without tangled elements, see Figures 5.9(c) and 5.9(f). The ideal triangle for each element is the element itself with straight edges in the initial configuration. Table

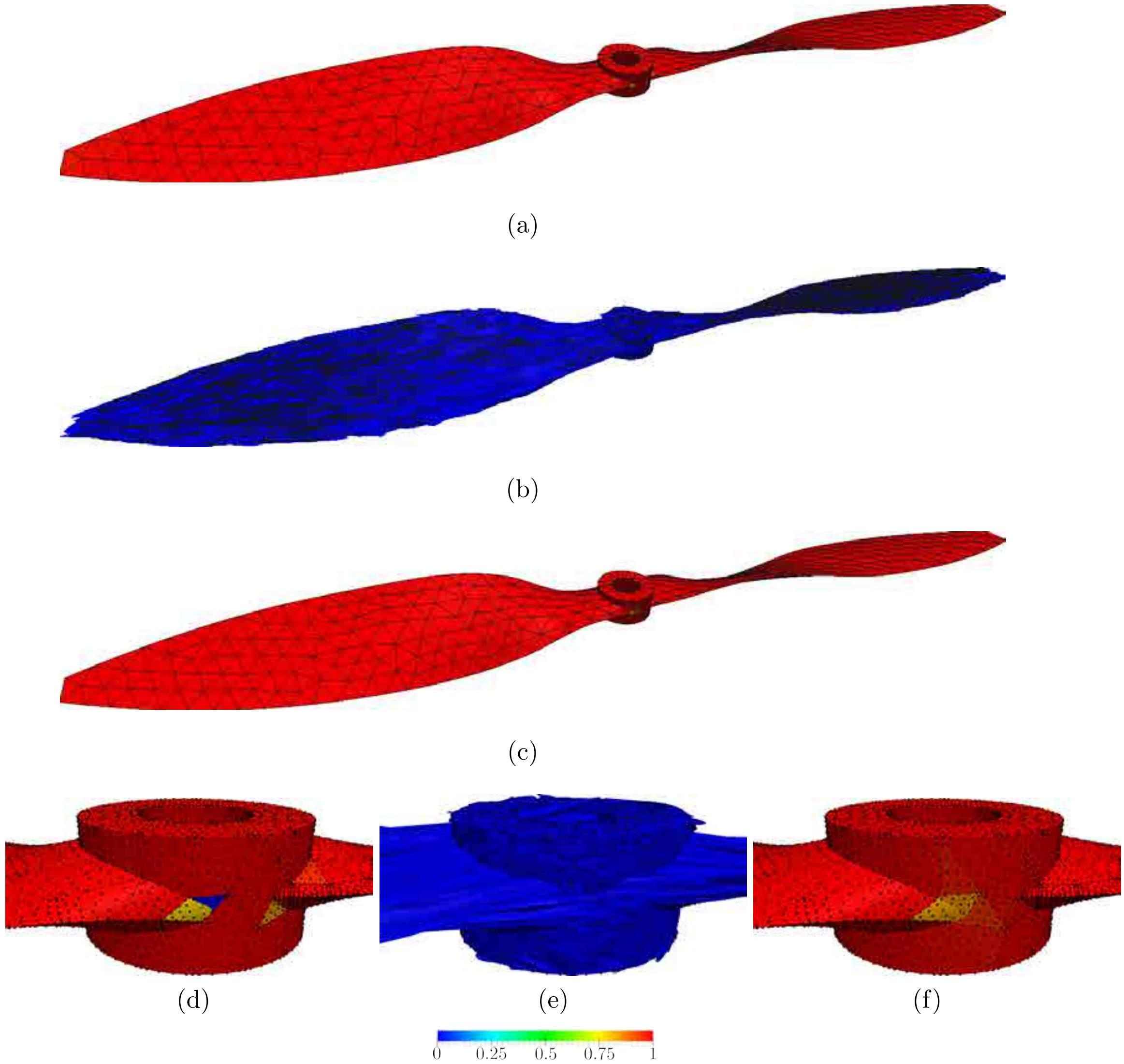

Figure 5.9: High-order meshes of polynomial degree five colored according to the shape quality measure for a propeller: (a,d) initial curved mesh, (b,e) tangled mesh, and (c,f) smoothed and untangled mesh.

5.3 summarizes the quality statistics of the three high-order meshes. We highlight that the smoothed mesh increases the values of the minimum quality of the initial and randomized meshes.

In addition, we have also smoothed the initial mesh (the mesh with only two tangled elements) and we obtain the same smoothed mesh up to minimization tolerance. Specifically, the relative distances between the smoothed meshes is $E = 1 \cdot 10^{-10}$, see Equation (5.28).

Figure	Min	Max	Mean	SD	Tang.
5.9(a)	0.00	1.00	1.00	0.04	2
5.9(b)	0.00	0.23	0.00	0.01	1372
5.9(c)	0.83	1.00	1.00	0.01	0

Table 5.3: Shape quality statistics of the high-order meshes on a propeller, presented in Figure 5.9.

p	Figure	Min	Max	Mean	SD	Tang.
1	5.10(b)	1.00	1.00	1.00	0.00	0
1	5.10(a)	0.21	1.00	0.93	0.09	0
5	5.10(d)	0.00	1.00	0.97	0.14	45
5	5.10(c)	0.00	1.00	0.91	0.16	45
5	5.10(f)	0.69	1.00	0.99	0.01	0
5	5.10(e)	0.24	1.00	0.93	0.09	0

Table 5.4: Shape quality statistics of the high-order meshes on a Falcon aircraft, presented in Figure 5.10.

5.5.2 High-order curved meshing

In this section, we analyze several aspects of the proposed *a posteriori* approach to generate high-order meshes on parameterized surfaces, see Section 5.1. First, we illustrate the complete procedure to generate a final valid high-order mesh on a CAD geometry. Next, we show that the proposed methodology is able to generate meshes of low and high polynomial degrees for a given geometry. Finally, we analyze the quality of the obtained meshes in terms of the scaled Jacobian measure, that is a standard measure of the smoothness of the element representation mapping, see Dey et al. (2001b); Sherwin and Peiró (2002); Persson and Peraire (2009); Xie et al. (2012).

5.5.2.1 High-order mesh generation on a CAD geometry

The objective of this example is to illustrate the complete process for the generation of a high-order mesh on a CAD geometry. We consider a CAD model of a Falcon aircraft and we generate a valid mesh of polynomial degree five. Figure 5.10 shows each one of the required steps. In the first column, the elements are colored according to the quality that results from considering an equilateral triangle as an ideal element. This is an absolute value of the quality, since it uses the same ideal for all the elements. In the second column, the elements are colored according to the quality measure

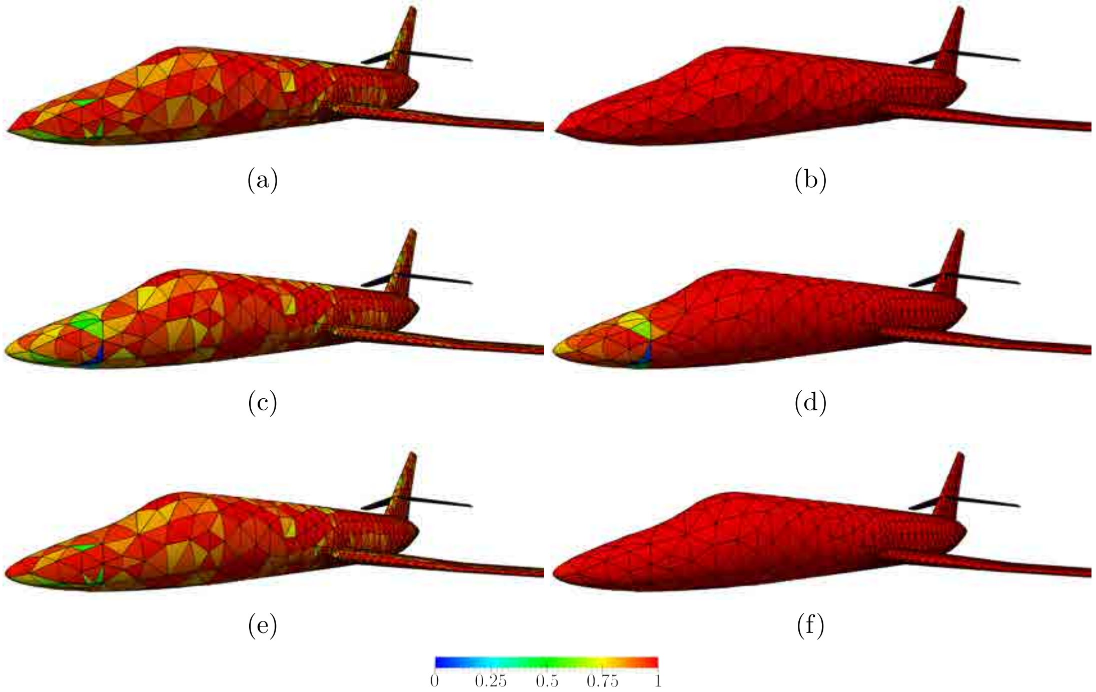

Figure 5.10: Snap-shots of the meshes involved in the generation of a high-order mesh for a Falcon aircraft: (a,b) initial linear mesh; (c,d) initial curved mesh of polynomial degree five, and (e,f) optimized mesh of polynomial degree five. The first column is colored taking the ideal as the equilateral triangle. The second column is colored taking the ideal as the corresponding element in the initial linear mesh.

that results from considering the initial straight-sided high-order elements as ideal elements. This is a relative value of the quality, that allows comparing each element to a different ideal triangle.

First, we generate an initial linear mesh using any established mesh generation procedure that provides control over the size and shape of the generated elements, see Figures 5.10(a) and 5.10(b). Note that these mesh characteristics will be inherited by the final high-order mesh. Second, we set the ideal mesh increasing the order of the initial straight-sided linear mesh. Thus, for the optimization procedure, the ideal triangle for each element is the high-order triangle itself with straight edges in the initial configuration. Third, we get the parametric coordinates of the linear mesh. If we do not have access to them, we use the projection technique presented in Roca (2009) to compute them. Next, we increase the polynomial degree of the mesh in the parametric space, and we map it to the CAD geometry, see Figure 5.10(c) and 5.10(d). Note that several tangled elements appear. Then, we optimize this mesh on the parametric space, and we map it to the surface. To assess that we obtain a valid high-order mesh composed by elements that preserve the shape of the initial linear mesh we present the optimized mesh in Figures 5.10(e) and 5.10(f).

Analyzing Figures 5.10(e) and 5.10(f), we realize that the quality distribution is similar to the quality distribution of the initial linear mesh. Thus, the optimized mesh has untangled the inverted elements of Figure 5.10(d) and is a valid high-order mesh that preserves whenever is possible the shape of the elements of the initial straight-sided high-order mesh.

Table 5.4 summarizes the quality values of the meshes presented in this example. Note that the optimized mesh does not include tangled elements. Note that the mean value of the shape quality is 0.99 with a standard deviation of 0.01 when the ideal is selected as the initial linear mesh.

5.5.2.2 High polynomial degree

The aim of this example is to show the capability of the presented methodology to generate valid and high-quality meshes for any polynomial degree. To this end, we first generate an initial linear mesh composed by 832 elements of the CAD geometry of a component of a gear box. Then, we increase the polynomial degree of the initial mesh to degree 3, 5, 8 and 10. As expected, these meshes contain tangled elements. In the first column of Figure 5.11 we present the initial high-order meshes. We observe that the number of tangled elements changes depending on the polynomial degree (from 10 tangled elements for degree 3 to 130 tangled elements for degree 10). The number of tangled element increases with the polynomial degree since the feasible region of the nodes of the higher degree elements is smaller. Then, we apply the proposed optimization procedure to each initial high-order mesh, selecting the ideal for each element as the element itself in the initial straight-sided high-order mesh. In the second column of Figure 5.11 we present the optimized high-order meshes.

Table 5.5 details the shape quality statistics of the presented meshes. For any of the tested degrees, the proposed procedure provides a valid and high-quality mesh, obtaining a valid configuration from an invalid initial one.

5.5.2.3 Validation of the smoothness of the representation mapping

In this section, we present an analysis of the scaled Jacobian measure for the degree 5 meshes generated in Secs. 5.5.1.3 and 5.5.2.1, and for the degree 10 mesh generated

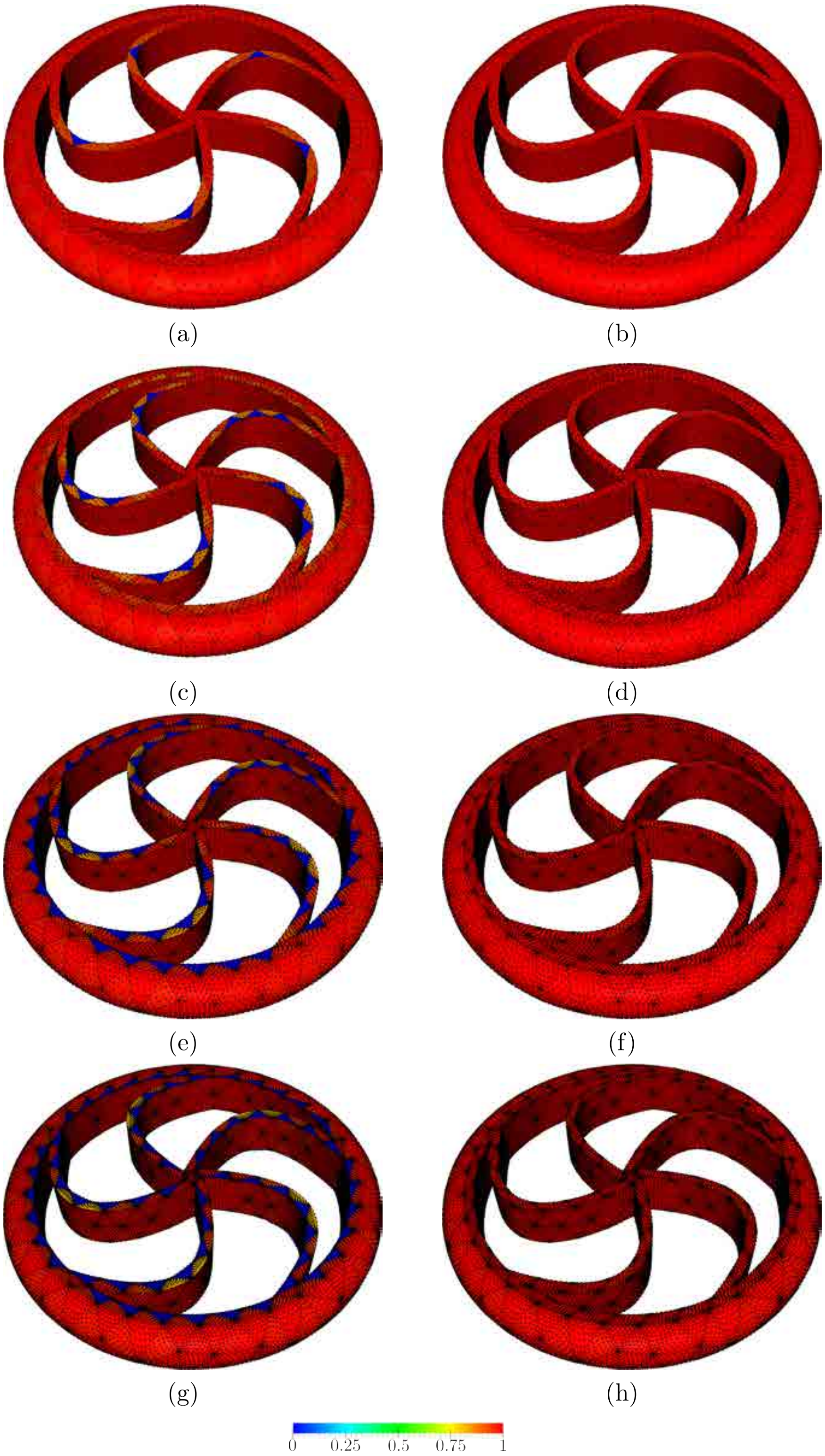

Figure 5.11: High-order meshes of polynomial degrees 3, 5, 8 and 10 for a component of a gear box. (a,c,e,g) Initial curved meshes. (b,d,f,h) Optimized meshes.

p	Figure	Min	Max	Mean	SD	Tang.
3	5.11(a)	0.00	1.00	0.98	0.11	10
3	5.11(b)	0.98	1.00	1.00	0.00	0
5	5.11(c)	0.00	1.00	0.95	0.19	30
5	5.11(d)	0.98	1.00	1.00	0.00	0
8	5.11(e)	0.00	1.00	0.86	0.34	110
8	5.11(f)	0.98	1.00	1.00	0.00	0
10	5.11(g)	0.00	1.00	0.83	0.36	130
10	5.11(h)	0.98	1.00	1.00	0.00	0

Table 5.5: Shape quality statistics of the high-order meshes on a component of a gear box, presented in Figure 5.11 .

in Section 5.5.2.2. The scaled Jacobian element quality measure

$$\mu = \frac{\min_{\boldsymbol{\xi}\in E^M} \mathbf{D}\boldsymbol{\phi}_P(\boldsymbol{\xi})}{\max_{\boldsymbol{\xi}\in E^M} \mathbf{D}\boldsymbol{\phi}_P(\boldsymbol{\xi})} \tag{5.31}$$

is widely used to assess the validity of the high-order mesh elements (Dey et al., 2001b; Sherwin and Peiró, 2002; Persson and Peraire, 2009; Xie et al., 2012), and it quantifies the variation of the Jacobian of the representation mapping. In fact, it quantifies the *linearity* of the representation mapping, being 1 only for constant Jacobian matrices, that is, for linear elements.

It is important to point out that we expect an improvement on the scaled Jacobian quality measure of the meshes obtained with the proposed optimization procedure. On the one hand, from Equation (5.31) we realize that the scaled Jacobian measure is constant for linear elements, and penalizes elements with non-constant Jacobian. On the other hand, we highlight that our approach considers as ideal the initial straight-sided high-order element. Thus, it tries to transform the physical curved element into a high-order element similar to the initial straight-sided one, while it maintains the nodes on the surface.

In Figure 5.12 we color the meshes presented in the previous examples using the scaled Jacobian quality measure. In the first and second columns of Figure 5.12 we show the initial and optimized high-order meshes, respectively. In Table 5.6 we display the scaled Jacobian quality statistics for the meshes presented in Figure 5.12. As expected, using the proposed approach we improve the minimum and the mean values of the scaled Jacobian quality measure in all the cases. Hence, we obtain valid and high-order meshes with a good behavior of the Jacobian of the representation mapping.

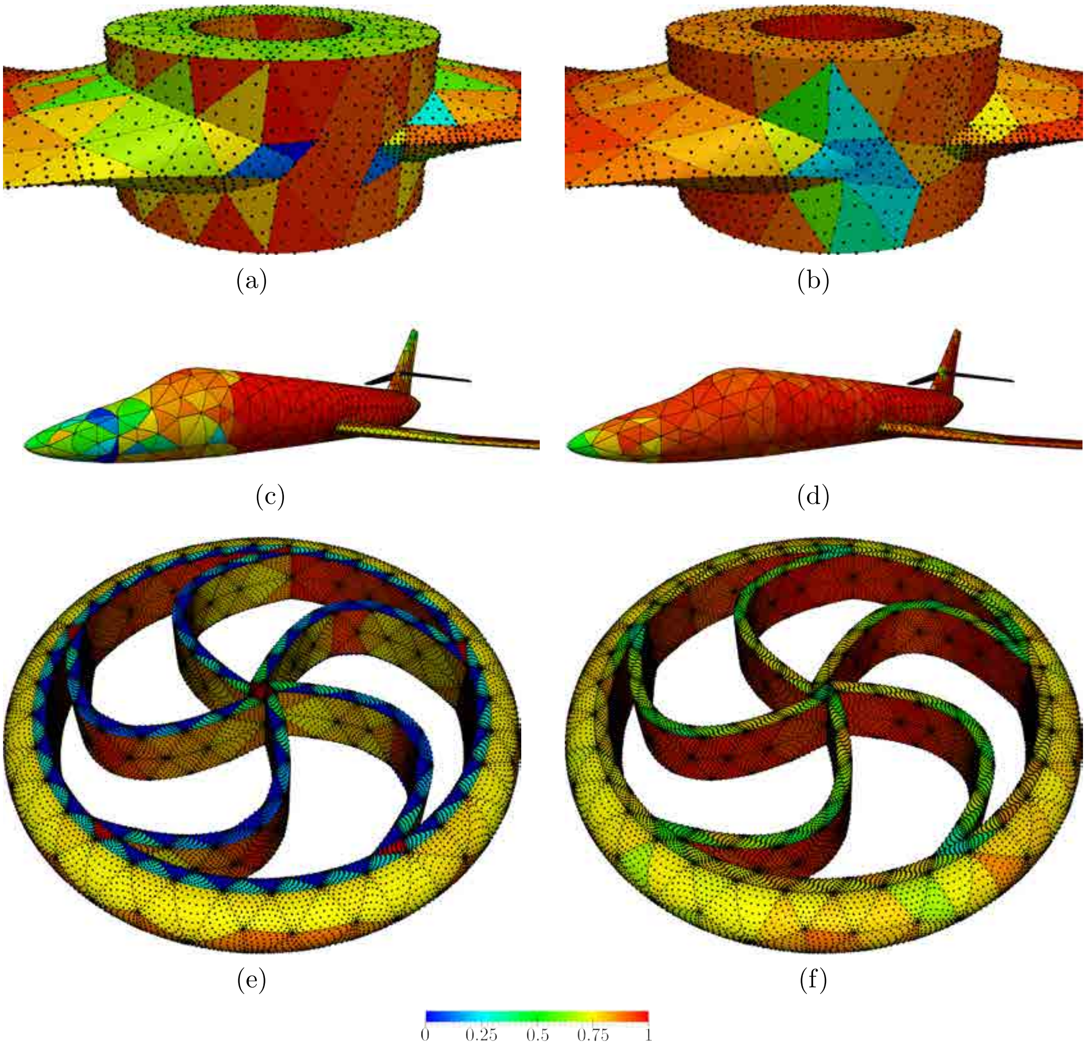
(a) (b) (c) (d) (e) (f)

Figure 5.12: Initial and optimized high-order meshes colored according to the scaled Jacobian quality measure for the examples presented in Section 5.5.2: (a,b) degree 5 meshes on a propeller, (c,d) degree 5 meshes on a Falcon aircraft, and (e,f) degree 10 meshes on a component of a gear box.

5.6 Concluding remarks

The main goal of this work is to validate and generate curved meshes of any polynomial degree on parameterized CAD surfaces. First, we detail a new technique to extend any Jacobian-based distortion (quality) measure defined for planar triangles to high-order elements on parameterized surfaces. The proposed measure is expressed in terms of the parametric coordinates of the mesh nodes, and we prove that it is

Mesh	Figure	Min	Max	Mean	Std.Dev.	Tang.
Initial	5.12(a)	-2.93	1.00	0.89	0.18	2
Smoothed	5.12(b)	0.18	1.00	0.95	0.08	0
Initial	5.12(c)	-0.75	1.00	0.85	0.25	50
Smoothed	5.12(d)	0.09	1.00	0.92	0.11	0
Initial	5.12(e)	-5.55	1.00	0.36	1.06	130
Smoothed	5.12(f)	0.26	1.00	0.81	0.16	0

Table 5.6: Scaled Jacobian element quality statistics of the high-order meshes presented on Figure 5.12.

independent of the surface parameterization.

Second, we develop a continuous optimization procedure to smooth and untangle high-order meshes on parameterized surfaces. Specifically, we propose a non-linear least-squares formulation to enforce in a weak form that the distortion of the mesh is minimal. The optimization procedure is formulated in terms of the parametric coordinates. Thus, it ensures that the nodes always lie on the exact CAD geometry. Moreover, the distortion measure is regularized to allow untangling inverted elements. In particular, the presented regularization technique avoids that a valid element becomes invalid and is capable of untangling highly meshes composed by a high number of inverted elements.

In addition, we prove that the optimization procedure is independent of the surface parameterization. That is, given two diffeomorphic parameterizations of the surface, the physical candidate locations are the same for both parameterizations. Therefore, this technique is particularly suited to generate high-order meshes on CAD geometries represented with by low-quality parameterizations.

Third, we present an *a posteriori* mesh generation procedure for CAD geometries. Specifically, given a linear mesh, we increase the polynomial order of the elements on the parametric space, and then we improve the quality of the resulting mesh by means of the proposed optimization procedure. Note that it is of the major importance that the optimization procedure allows untangling, since when the polynomial degree of the elements is increased, inverted elements appear close to the curved edges.

To conclude, we have included several examples to show the properties of the presented procedure, and to illustrate the *a posteriori* approach to generate high-order meshes. We present two sets of examples. First, we assess the properties of the presented technique: consistence, the independence of the surface parameterization, and robustness of the untangling technique. Second, we analyze the mesh generation process for CAD geometries. We show a detailed decomposition of the mesh generation process, the capability to generate low and high-order meshes up to degree ten, and a detailed analysis of the meshes obtained on three different CAD models.

Chapter 6

Hierarchical and *a posteriori* generation of curved meshes for unstructured high-order methods

---

High-order meshes are usually generated using *a posteriori* approaches (Dey et al., 1997, 2001a; Luo et al., 2002, 2004; Luo, 2005; Shephard et al., 2005; Sherwin and Peiró, 2002; Persson and Peraire, 2009; Xie et al., 2012; Toulorge et al., 2013) whereby the final mesh is obtained by modifying an initial linear mesh. Starting from an initial linear mesh that approximates the domain geometry, the first step consists of adding high-order nodes, either by enriching the linear element uniformly or according to a suitable distribution aimed at minimizing interpolation errors (Hesthaven and Warburton, 2007; Warburton, 2006). Next, the boundary nodes are projected onto exact curved boundary. Finally, the mesh is smoothed and untangled to remove the non-valid (folded) and low-quality (distorted) elements that might be created during the curving of the mesh boundary. This last step is indeed the most critical to ensure the quality of the generated meshes. When the grid deformation dictated by the projection of the boundary nodes onto the boundary of the domain is small, existing approaches are effective at producing suitable high-order meshes, but they often fail for more extreme cases where the required deformation is larger.

The main goal of this chapter is to use an *a posteriori* approach to generate 3D curved high-order meshes in which the boundary nodes are on CAD surfaces. To this end, we use a hierarchical approach to mesh each of the geometry entities. In particular, we first generate a valid surface mesh using the approach presented in Chapter 5. Next, we use the smoothing and untangling method presented in Chapter 4 to convert the initial linear mesh of the volume to the desired valid curved high-order mesh.

The remainder of the chapter is organized as follows. In Section 6.1 we detail the hierarchical approach to generate the meshes on each entity. In Section 6.2, we present the proposed *a posteriori* approach. Next, in Section 6.3 we present the mesh generation procedure for three different simulations. First, in Section 6.3.1 we present the *a posteriori* generation of a mesh of polynomial degree seven for the Barcelona harbor, and illustrate a wave propagation problem computed using the generated mesh. Second, in Section 6.3.2 we present the generation procedure for a mesh of polynomial degree four on a Falcon aircraft. Moreover, we illustrate an inviscid flow simulation using the generated mesh. Finally, in Section 6.3.3 we present a procedure to transform an inviscid mesh into a viscous mesh that has the stretching desired by the user around a target object. In particular, we illustrate the mesh generation procedure of a mesh of polynomial degree four on the exterior domain of a sphere, and the corresponding viscous simulation. In addition, we present the generation of a boundary layer mesh of polynomial degree four on a SD7003 airfoil.

6.1 Hierarchical approach

In this thesis, we follow a hierarchical procedure to generate high-order meshes. First, we will generate all the vertices of the high-order mesh. Second, we will generate a 1D mesh of the desired polynomial degree such that it approximates the curved edges of the geometry. Third, we will generate a 2D high-order mesh of the surfaces, and finally, once determined the boundary mesh, we will generate the volumetric high-order mesh. For all entities, we follow an *a posteriori* approach. That is, starting from the linear mesh on that entity, we obtain a high-order mesh. In particular, we follow the next procedure:

1. For each vertex of the linear mesh, we generate the corresponding node of the high-order mesh.

2. Given an edge from the linear mesh, if it is on a curve of the CAD geometry,

we will use the arc parameter to find a configuration of the high-order nodes on the parametric space, such that once mapped to the physical space it corresponds to a Legendre-Gauss-Lobatto distribution (Warburton, 2006; Hesthaven and Warburton, 2007). If the edge is not adjacent to a curve, we increase its polynomial order and we keep it straight-sided.

3. Once all the edges are of the desired polynomial order, we follow a similar procedure for the faces. On the one hand, if a given linear face is adjacent to the CAD geometry, we use a point distribution on the parametric space that provides a quasi-optimal Lebesgue constant by means of the blending presented in Warburton (2006); Hesthaven and Warburton (2007). Next, we map the nodes to the physical domain using the surface parameterization. Note that this elements can be invalid, since the physical edges are curved and the surface parameterization may be anisometric. Hence, we use the optimization procedure presented in Section 5 in order to ensure that the physical configuration is valid. On the other hand, if the face is not on the boundary, we increase its polynomial degree directly on the physical space.

4. Once all the faces are of the desired polynomial order, we generate the high-order volumetric elements. First, we increase the polynomial order of the element adding the remaining high-order nodes. Note that the resulting elements may be invalid, since the boundary faces and edges are curved matching the geometry. Therefore, next we optimize the location of the nodes that are not on the boundary geometry. In this manner, the volumetric elements are curved close to the CAD geometry in order to accommodate the curving of the boundary faces.

6.2 *A posteriori* generation of curved high-order meshes

In this section, we use the discrete formulation for curving presented in Section 4.1.2 to propose a new *a posteriori* approach to generate curved high-order meshes. This procedure is composed by three steps: generating the ideal mesh; curving the mesh boundary; and curving the mesh volume. Fig. 6.1 illustrates these three main steps in 2D.

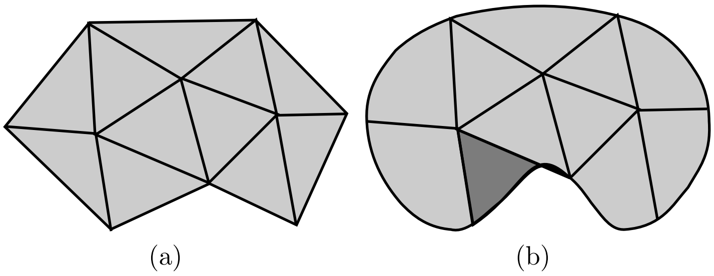

(a) (b) (c)

Figure 6.1: High-order mesh generation procedure: (a) ideal high-order mesh $\mathcal{M}_I$, (b) initial curved mesh $\phi_h^0(\mathcal{M}_I)$, and (c) final optimized mesh $\phi_h^*(\mathcal{M}_I)$. Invalid elements are colored in dark gray.

6.2.1 Generating the ideal mesh: obtain $\mathcal{M}_I$

Generate a linear mesh. We generate a linear mesh with any robust and well established linear mesher. Note that this mesh prescribes the topology and the geometrical requirements (size, shape, stretching...) of the final high-order mesh.

Set the ideal mesh $\mathcal{M}_I$. Once the linear mesh is generated, we increase its polynomial degree, see Fig. 6.1(a). We set this high-order straight-sided mesh as the ideal mesh $\mathcal{M}_I$.

6.2.2 Curving the mesh boundary: obtain g_h and set ϕ_h^0

Obtain a valid curved boundary mesh g_h. To generate a valid and high-quality high-order surface mesh, g_h, we use the technique presented in Chapter 5. In these previous works, we detail an optimization based method to generate valid and high-order meshes with the nodes on the CAD surfaces. Note that generating a valid surface mesh is of the major importance for ensuring the robustness of the proposed procedure. If the boundary mesh contains a single inverted element, then the 3D mesh will be always invalid.

Set the initial curved high-order mesh $\phi_h^0(\mathcal{M}_I)$. We curve the boundary faces of the straight-sided mesh imposing the curved surface mesh determined by g_h and we set this high-order mesh as the initial configuration, $\phi_h^0(\mathcal{M}_I)$, of our procedure. It is important to point out that this mesh may contain a large number of invalid (tangled) elements on the boundary, the dark gray element in Fig. 6.1(b) illustrates this issue in

2D. In Chapter 6.3.2, we show several configurations where invalid tetrahedra appear close to the curved features of the geometry.

6.2.3 Curving the mesh volume: obtain ϕ_h^*

Finally, we smooth and untangle the curved and high-order mesh using the optimization procedure proposed in Section 4.1.2. Specifically, we solve the minimization problem stated in Equation (4.4) taking as ideal the high-order straight-sided mesh $\mathcal{M}_I$. Fig. 6.1(c) shows the optimized mesh for the 2D analogy. Since the initial approximation, $\phi_h^0(\mathcal{M}_I)$, can contain invalid elements, it is mandatory that the optimization technique allows untangling invalid elements. Our approach allows untangling by means of using a distortion measure, see Equation (3.2), that can be regularized, see Equation (3.6), to explicitly penalize those elements that have negative values of the determinant of the Jacobian. The final curved high-order configuration is given by $\phi_h^*(\mathcal{M}_I)$.

6.3 Results

The final goal of the methods developed in this thesis is to generate curved high-order meshes that are valid to perform finite element analysis with solvers that feature high-order unstructured meshes. In this work we propose an *a posteriori* mesh generation procedure to ensure that the high-order mesh is valid, high-quality, and curved to match the CAD geometry. In this manner, we obtain a mesh with an accurate approximation of the curved domain that avoids the spurious effects that arise with piecewise linear approximations (Bassi and Rebay, 1997; Dey et al., 1997; Luo et al., 2002; Xue and Demkowicz, 2005; Sevilla et al., 2011).

In this chapter, we use the approach proposed in Section 6.2 to generate valid curved high-order meshes that match the boundary geometry for three different applications. First, in Section 6.3.1, we generate a triangular mesh of polynomial degree seven on the Barcelona harbor to solve a wave propagation problem. Second, in Section 6.3.2 we generate a tetrahedral mesh of polynomial degree four on a Falcon aircraft, to solve an inviscid flow computation. Finally, in Section 6.3.3, we present a technique to generate boundary layer meshes, and we present a viscous flow computation around an spheric geometry.

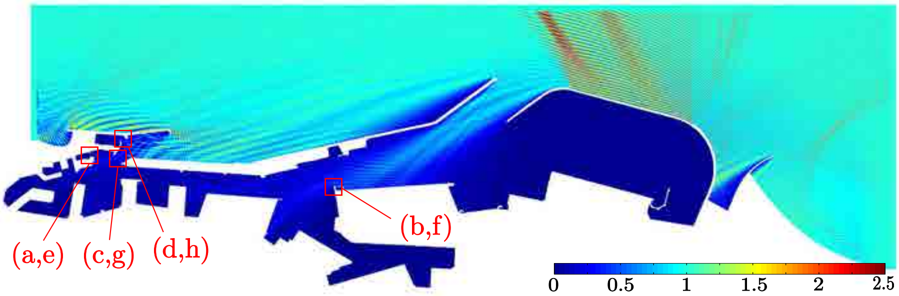

Figure 6.2: Wave amplification factor on the Barcelona harbor for an incident wave of height equal to 1. The solution is obtained on a high-order mesh of polynomial degree 7.

6.3.1 Barcelona harbor

In this example, we generate a high-order mesh for computing the wave agitation inside the Barcelona (Spain) harbor. The physical problem that is studied is the wave propagation in highly reflective coastal areas. The final goal is to obtain the wave amplification factor for an incident wave of height one. The Barcelona harbor contains several small geometric features (10 m length) compared to the total extension of the domain (12 km), requiring fine computational meshes if linear elements are used. On top of that, high-order elements are needed in order to reduce the numerical dispersion error, commonly associated with the propagation of high frequency waves in presence of numerous reflections. Using a mesh composed by 2.4 millions of linear elements an erroneous solution without physical meaning is obtained. However, using a high-order mesh of polynomial degree 7 composed by 32802 elements (803649 nodes), the dispersion error can be reduced obtaining an accurate solution. Figure 6.2 shows the wave amplification factor for the Barcelona harbor when the angle between the incident wave and the x-axis is 43 degrees and the period is 6 seconds (Huerta et al., 2011; Giorgiani et al., 2013).

To generate a high-order mesh for this problem, we first generate a linear triangular mesh, and we increase the polynomial degree, curving the boundary edges and maintaining straight the interior edges. Figure 6.3 shows the initial and smoothed curved high-order meshes, displaying also the high-order quality of the elements, for the four areas marked in Figure 6.2. We apply the optimization procedure using a Fekete distribution of nodes on the master and ideal element. Figures 6.3(a) to 6.3(d) present the four selected details of the initial mesh. Note that Figures 6.3(a), 6.3(b) and 6.3(c) contain non-valid elements. Figures 6.3(e) to 6.3(h) show the four selected

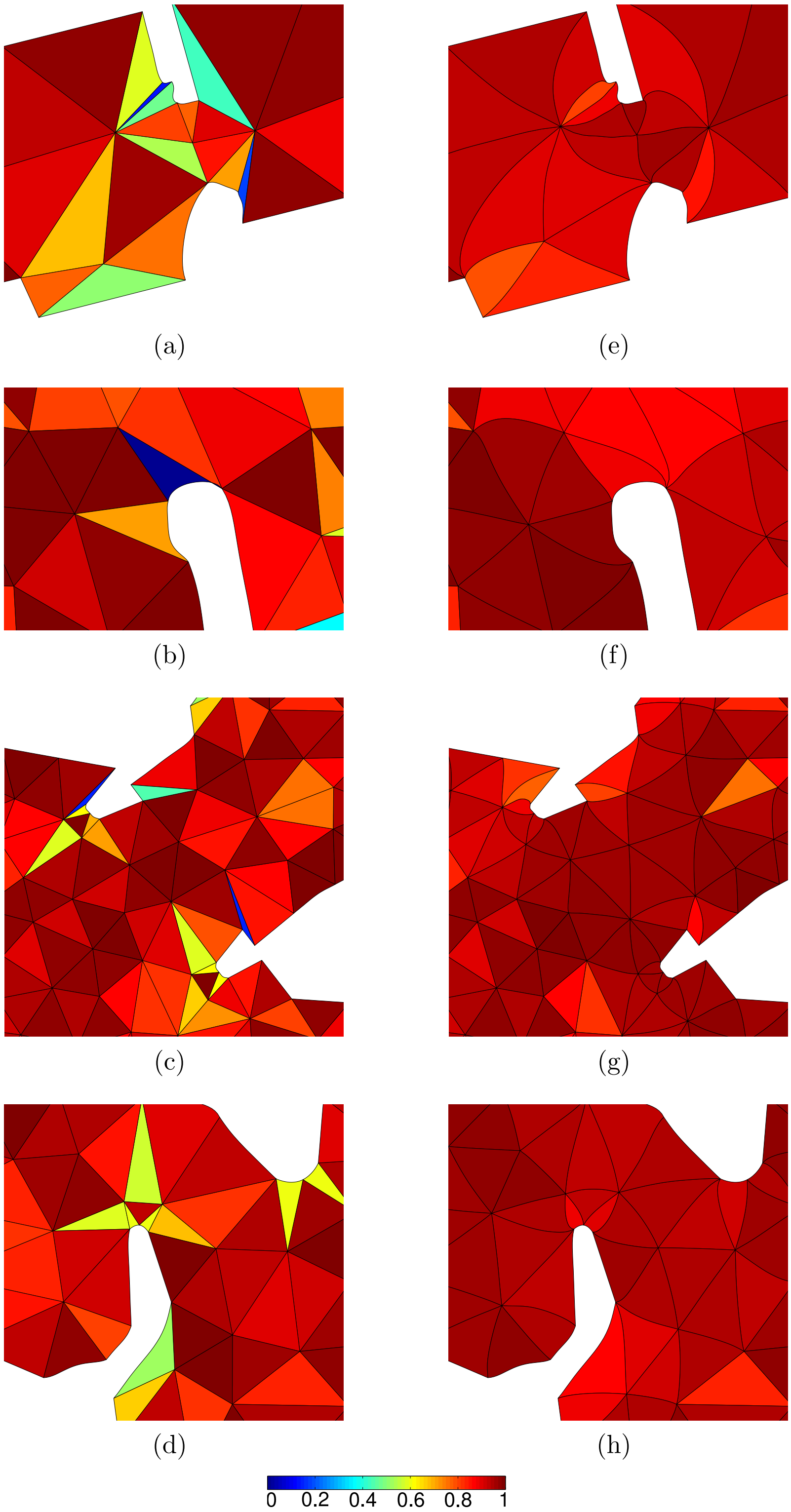
(a) (e)

(b) (f)

(c) (g)

(d) (h)

Figure 6.3: Details of a high-order mesh for the Barcelona harbor: (a) to (d) details of the initial curved mesh, (e) to (h) details of the smoothed mesh.

Figure	Min.	Max.	Mean	Std.Dev.	#inv
6.3(a-d)	0.00	1.00	0.91	0.08	3
6.3(e-h)	0.52	1.00	0.92	0.08	0

Table 6.1: Quality statistics for mesh of polynomial degree 7 on the Barcelona harbor.

Table 6.2: Quality statistics of a mesh of polynomial degree 4 for a Falcon aircraft. The mesh is composed by 27511 elements and 317854 nodes.

Mesh	Figure	Min	Max	Mean	Std. Dev.	#inv
Straigh-sided	6.4(a)	1.00	1.00	1.00	0.00	0
Initial	6.4(b)	0.00	1.00	0.99	0.02	12
Smoothed	6.4(c)	0.31	1.00	0.99	0.01	0

details of the smoothed mesh. The final mesh is composed by valid and high-quality elements. Specifically, on the boundary we obtain well shaped elements with curved edges, whereas inner elements tend to have straight edges. Table 6.1 displays the quality statistics of the presented meshes.

6.3.2 Generation of curved and high-order tetrahedral meshes for unstructured methods

In this section, we illustrate the complete *a posteriori* mesh generation approach on a 3D domain. Specifically, we present the main steps involved in the generation of a smoothed and untangled high-order mesh of polynomial degree five for the exterior domain of a Falcon aircraft. Finally, we show that the meshes obtained with the presented approach can be used to perform simulations with any unstructured high-order tetrahedral solver. In all figures, we color the meshes with respect to the quality at each point of the mesh, *i.e.* the inverse of the distortion of that point. Moreover, or all the examples, we present a table summarizing the quality statistics of the mesh elements. Specifically, we provide: the minimum, the maximum, the mean and the standard deviation of the mesh quality, and the number of tangled elements.

6.3.2.1 Generation of curved high-order tetrahedral meshes from CAD models

We consider the CAD definition of a Falcon aircraft and a mesh of degree 4 with valid and high-quality elements on the exterior domain. The straight-sided high-

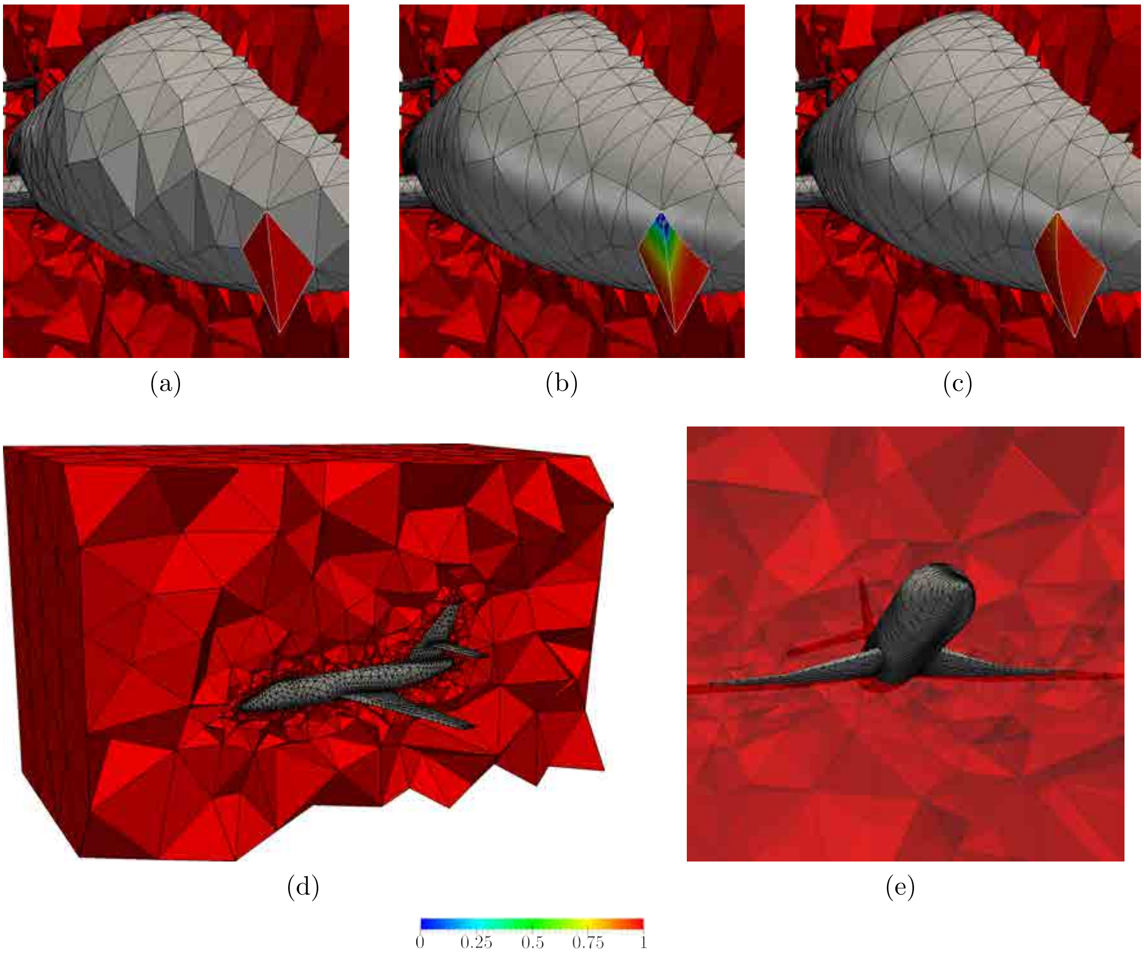
(a) (b) (c)

(d) (e)

Figure 6.4: Tetrahedral meshes of polynomial degree 4 around a Falcon aircraft. Detail of the: (a) ideal straight-sided mesh, (b) initial curved mesh, and (c) smoothed mesh. (d,e) General views of the smoothed mesh. In figures (a,b,c) two inverted high-order elements that appear when the mesh is curved are shown with the edges in white.

order mesh is shown in Figure 6.4(a). We choose this mesh as the ideal mesh, since we want to preserve the mesh features (shape, size, anisotropy...) of the linear mesh. We curve the boundary faces by relocating the nodes on the CAD surface, see Chapter 5. This process leads to 12 non-valid elements. Figure 6.4(b) presents a detail of the initial curved mesh near the nose and Figure 6.4(c) shows a detail of the optimized mesh near the nose including the two inverted elements highlighted in Figure 6.4(b). Additional details of the different meshes are shown in Figure 6.5. Finally, Table 6.2 summarizes the mesh quality statistics highlighting the superior qualities of the

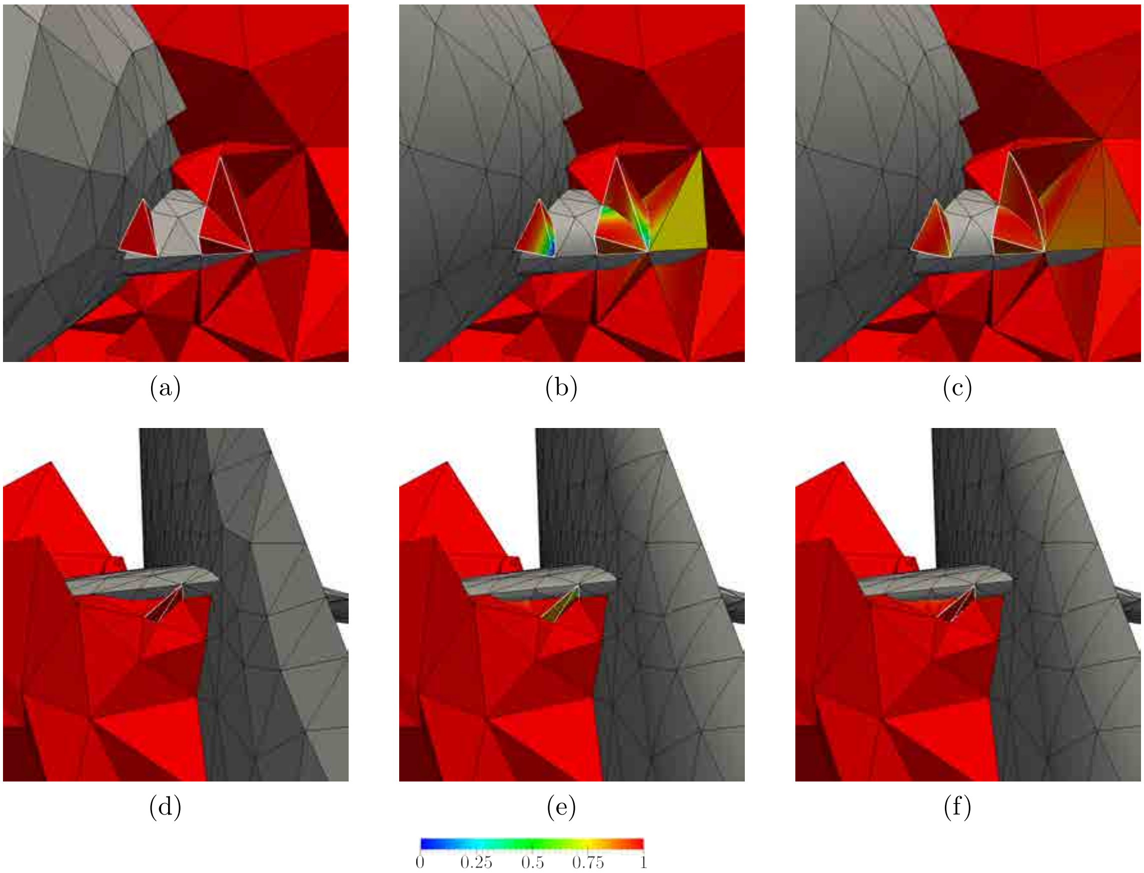
(a) (b) (c)

(d) (e) (f)

Figure 6.5: Tetrahedral meshes of polynomial degree 4 around a Falcon aircraft. Detail of the mesh where inverted elements can be observed: (a,d) straight-sided mesh, (b,e) initial curved mesh, and (c,f) smoothed mesh. Some inverted high-order elements that appear when the mesh is curved (b,d) are shown with white edges.

Table 6.3: Quality statistics of the mesh of polynomial degree 4 for a Falcon aircraft used in the numerical simulation. The mesh is composed by 64992 elements and 96258 nodes.

Mesh	Figure	Min	Max	Mean	Std. Dev.	#inv
Initial	-	0.00	1.00	0.99	0.009	11
Smoothed	6.6	0.85	1.00	0.99	0.003	0

smoothed high-order mesh.

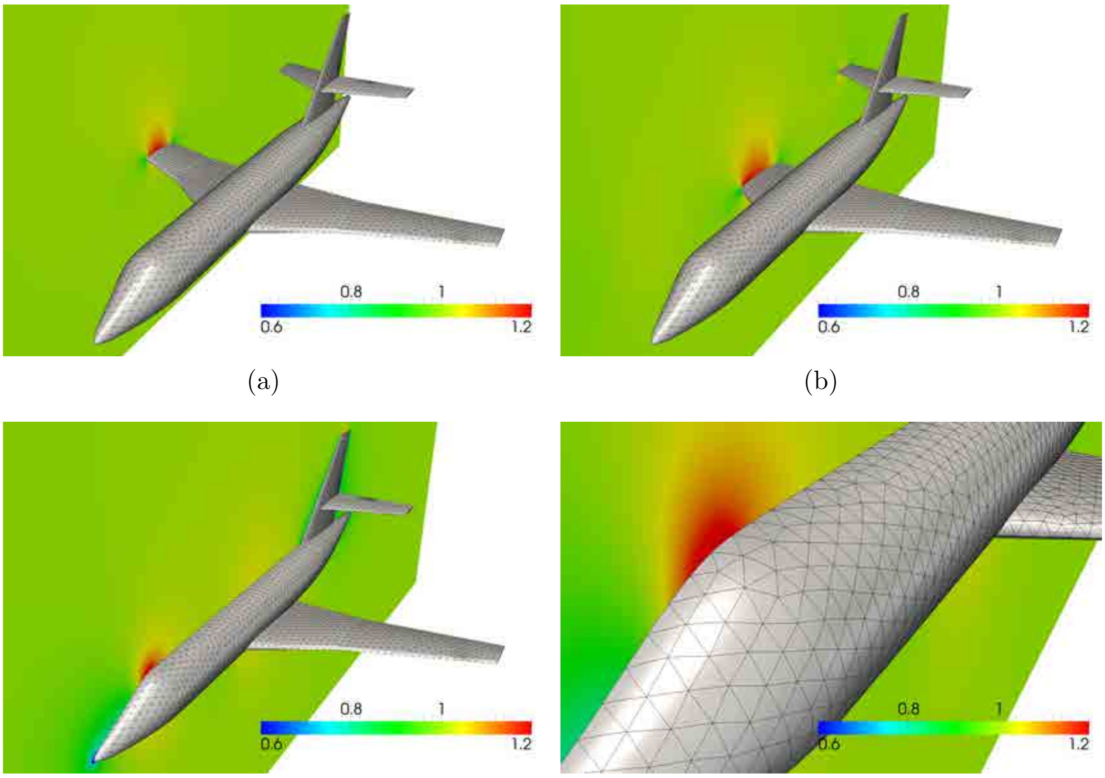

(a) (b)

(c) (d)

Figure 6.6: Curved mesh and inviscid flow around a Falcon aircraft for polynomial degree four, $\alpha = 0°$, and $M_\infty = 0.6$. Distribution of the magnitude of the velocity on different cut planes: (a,b,c) general view, and (d) detailed view.

6.3.2.2 Inviscid flow solution on a curved and high-order tetrahedral mesh

We perform a flow simulation using a high-order mesh for the Falcon geometry of the previous example. We consider an inviscid flow with a free stream Mach number of 0.6 (M_∞) and an angle of attack of 0° (α). The mesh quality statistics of the initial and optimized meshes are shown in Table 6.3. Then, we use this mesh to obtain an approximation of the steady state solution of the Euler equations. This approximation is obtained with a 3D and parallel solver (Roca et al., 2013) using the hybridized discontinuous Galerkin (HDG) method (Cockburn et al., 2009; Nguyen et al., 2009a,b; Peraire et al., 2010). Both the steady state solution and the mesh are represented by element-wise polynomials of degree 4. The mesh is composed by 64992 elements and 129984 faces. Each element (face) of polynomial degree four contains

35 (21) points. Furthermore, the solution of the compressible Euler equations has 5 components per point that correspond to the conserved quantities, namely: the density, the momentum, and the energy. This results in an HDG solution having a total of 14103264 degrees of freedom (DOFs) where: 11373600 DOFs are on the elements, and 2729664 DOFs are on the faces. To reduce the computation time, the mesh is partitioned in 128 sub-domains and accordingly, the HDG solver is run on 128 cores. In Figure 6.6, we present the magnitude of the velocity of the steady state of the inviscid flow, and a detail of the curved and high-order mesh on the aircraft surface. We point out that the curved elements are required to obtain a steady state solution of the Euler equations. Note that if the initial linear mesh is converted to a high-order mesh of degree four, but composed by straight-sided tetrahedra, the HDG solver does not converge to a steady state solution. This is in full agreement with the results reported in Bassi and Rebay (1997), where they show that piece-wise linear approximations of the curved surfaces lead to artificially polluted solutions of the Euler equations. On the contrary, the meshes generated with the proposed method allow the convergence of the HDG solver.

6.3.3 Inserting curved boundary layers for viscous flow simulation with high-order tetrahedra

We propose an *a posteriori* approach for generating curved meshes for viscous flow simulations composed by high-order tetrahedra. The proposed approach is performed in the following three steps: (1) generate a linear tetrahedral mesh for inviscid flow; (2) insert a boundary layer mesh, composed by linear tetrahedra, on the viscous part; and (3) convert the linear tetrahedral mesh to a curved and high-order mesh for viscous flow. This approach provides high-order tetrahedral meshes with boundary layer parts that are composed by elements that are: curved, valid, and of any polynomial degree.

The main application of the obtained meshes is the simulation of viscous flow with high-order unstructured solvers. Since the obtained meshes are conformal and fully composed by tetrahedra, they can be used with any continuous and discontinuous Galerkin solver that features linear and high-order tetrahedra. That is, it does not require a solver for non-conformal and hybrid meshes. To show the applicability of the method, we present the flow around a curved geometry obtained with the hybridized discontinuous Galerkin method.

6.3.3.1 Methodology and application: flow around a sphere

In this section, we outline the proposed method and we apply it to generate a mesh for the simulation of the viscous flow around a sphere. Note that a high-fidelity approximation of the flow requires a curved and high-order mesh with an anisotropic boundary layer in the regions adjacent to the sphere. The geometry of the sphere is described *exactly* (up to machine accuracy) by a 3D CAD model composed by 8 NURBS surfaces of degree 3 that correspond to the sphere octants. The rest of the mesh can be isotropic and corresponds to the inviscid part of the flow.

To illustrate the method, below we describe the meshes obtained in the different steps. Specifically, all the elements are colored according to a measure of the quality respect the ideal straight-sided element, Chapter 3, see Figure 6.9. This quality measure is also used to obtain the mesh statistics, see Table 6.4. Furthermore, the reciprocal of the quality (distortion) is minimized to smooth and untangle the inserted elements on the viscous part, see Chapter 4 for details. Note that this node relocation approach approach is an alternative to existent curved boundary layer meshing methods based on topological modifications (Sahni et al., 2010). Finally, we present a high-order approximation of the flow around the curved mesh of a sphere. The flow is obtained with a parallel implementation of the hybridized discontinuous Galerkin method (Roca et al., 2013).

1. Generate a linear tetrahedral mesh for inviscid flow. The first step in our methodology is to generate an isotropic linear mesh for inviscid flow simulations. The mesh has to be finer in the regions of higher curvature, and has to provide the required resolution on the inviscid part. Specifically, the inviscid mesh for the sphere is composed by 18936 linear tetrahedra and 3753 points, Figure 6.9(a). All the elements have quality one, since this initial mesh is considered the ideal mesh for the inviscid part.

2. Insertion of the boundary layer in the viscous part. The goal of this step is to obtain a valid linear mesh for viscous flow simulations. This step is performed in two stages: i) insert a linear boundary layer; and ii) smooth and untangle the initial viscous linear mesh.

First, we insert the topology of the boundary layer. To this end, we generate a layer of prisms by extruding in the normal direction the triangles on the wall boundary. The extrusion distance is the ten percent of the final desired boundary layer height since the goal is just to obtain the mesh topology. Then, the inserted

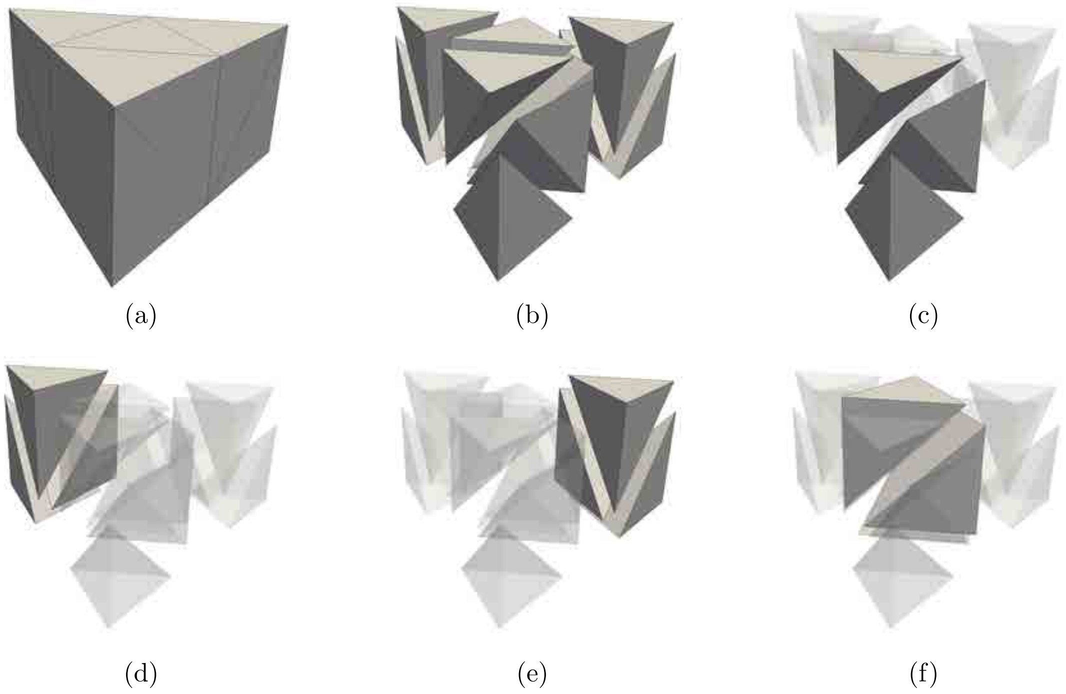

Figure 6.7: Template for a prism defined by an extruded triangle on the wall boundary.

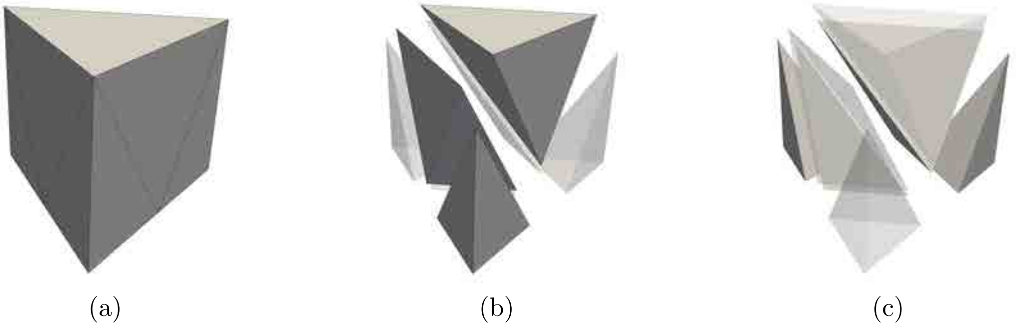

Figure 6.8: Template for a prism connecting the viscous and inviscid parts of the mesh.

layer is converted to a boundary layer mesh by splitting each prism in several levels of tetrahedra. The number of levels is characterized by: an initial size on the normal direction, the growing factor of the size along the normal direction, and a final size. To split the inserted layer, we consider two templates to split a prism in tetrahedral elements. The first template (Figure 6.7) is composed by 12 tetrahedra, and it is stacked along the normal direction, starting from the wall boundary, to form the boundary layer. The second template (Figure 6.8) is composed by 7 tetrahedra, and is used to connect the last layer of the viscous part of the mesh with the first layer of the inviscid part. Both templates ensure that the obtained mesh is conformal. Note that the triangles of the wall boundary have to be split into four triangles to insert the boundary layer. The boundary layer topology is composed by 24986 elements. This results in a viscous mesh composed by a total of 43922 elements and 8595 points. Note that the inserted tetrahedra have lower quality than the ones on the inviscid part, see Figure 6.9(b).

Second, we smooth and untangle the mesh with the inserted boundary layer. The goal of this step is to obtain a valid and high-quality viscous mesh. The elements on the viscous part have to present the desired stretching, and the elements on the inviscid part have to resemble the mesh size features of the initial linear mesh. To this end, we assign a different ideal element to each element of the mesh. One the one hand, each element on the viscous part is idealized by a tetrahedron that presents the proper stretching along the normal direction to the wall boundary. On the other hand, the elements on the inviscid part are idealized by the corresponding initial linear element. Then, we minimize the distortion respect the assigned ideal mesh using the smoothing and untangling procedure proposed in Chapter 4. This results in a valid tetrahedral mesh with an inserted boundary layer of the proper size and stretching, see Figure 6.9(c).

3. Conversion to a curved and high-order tetrahedral mesh. In this step, the valid viscous mesh is converted to a curved and high-order tetrahedral mesh. This process is also composed by two stages: i) convert the whole mesh to a high-order mesh; and ii) smooth and untangle the viscous high-order mesh.

First, the linear tetrahedral mesh with the inserted boundary layer is curved and converted to a high-order mesh. To this end, all the straight-sided elements of the mesh are expressed in terms of element-wise polynomials of degree four. Then, the nodes that correspond to faces on the wall boundary are forced to be on the sphere. This results in a curved and high-order mesh with 311 non-valid elements close to the wall boundary, see Table 6.4.

Second, we repair these invalid elements and increase the mesh quality by using again the smoothing and untangling procedure. It is important to highlight that now the ideal mesh is represented by the viscous linear mesh. The result is a valid curved

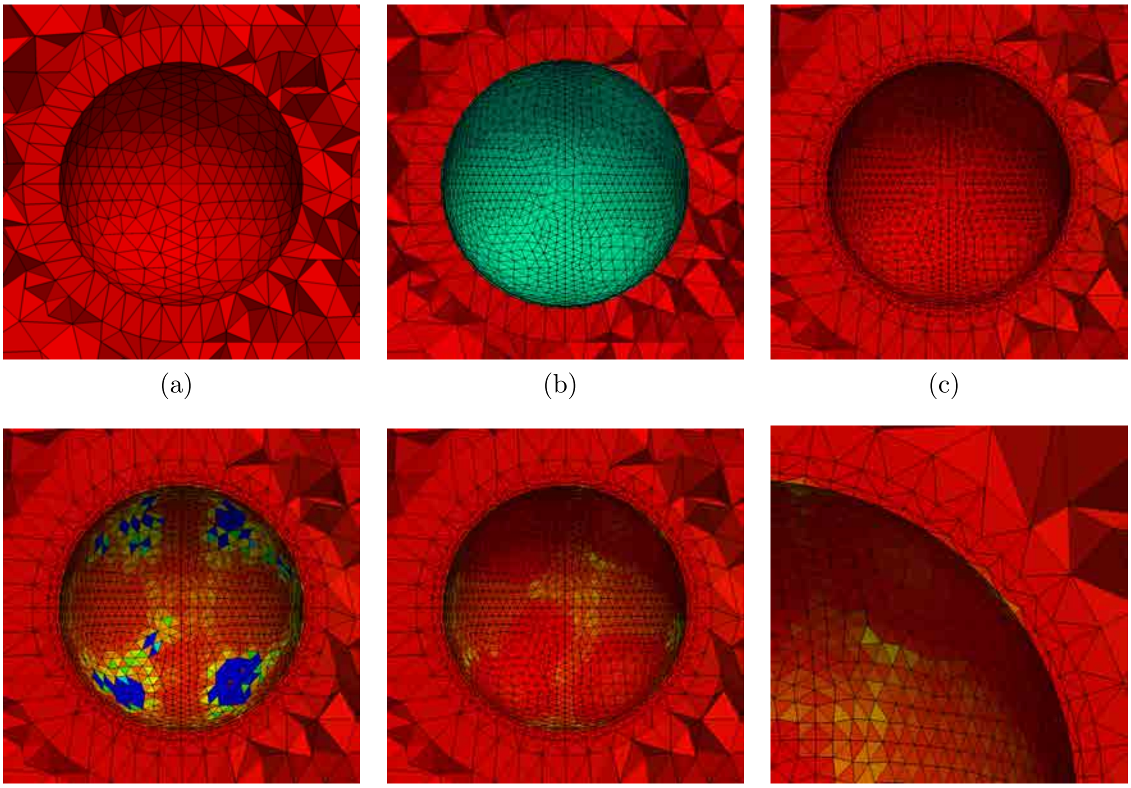

(a) (b) (c)

(d) (e) (f)

Figure 6.9: Shape quality along the process. (a) Inviscid linear mesh. Viscous linear mesh: (b) inserted boundary layer topology, and (c) smoothed and untangled mesh. Viscous mesh of polynomial degree 4: (d) curved wall boundary, (e) smoothed and untangled mesh, and (f) detail of the curved and high-order boundary layer.

Table 6.4: Shape quality statistics of the meshes presented in Figure 6.9.

p	#elems	#nodes	Figure	Min.Q.	Max.Q.	Mean Q.	Std.Dev.	#Inv.
1	18936	3753	6.9(a)	1.00	1.00	1.00	0.00	0
1	43922	8595	6.9(b)	0.32	1.00	0.61	0.34	0
1	43922	8595	6.9(c)	0.97	1.00	1.00	0.00	0
4	43922	487082	6.9(d)	0.00	1.00	0.98	0.09	311
4	43922	487082	6.9(e)	0.44	1.00	0.99	0.02	0

mesh composed by 43922 valid tetrahedra of polynomial degree 4 and 487082 points, see Table 6.4. Note that the elements that compound the boundary layer are curved and present the desired anisotropy, see Figures 6.9(d) and 6.9(e).

4. Simulation of the viscous flow around a sphere. Finally, the obtained

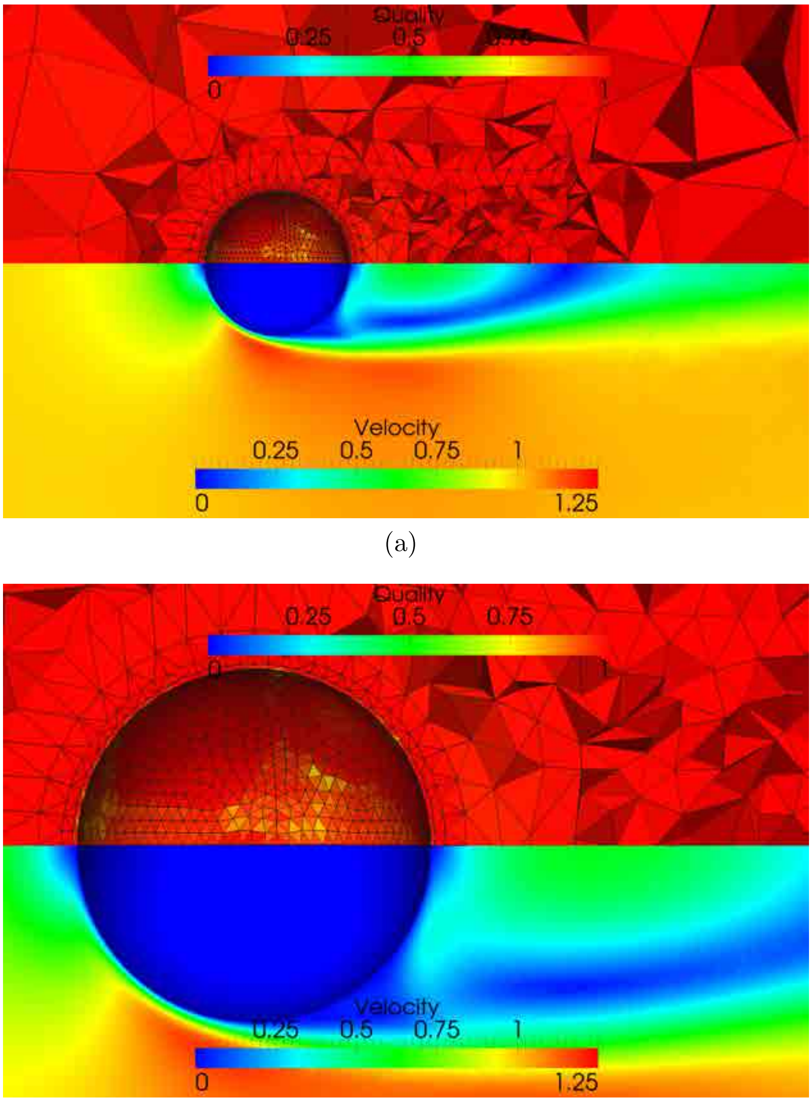

(a)

(b)

Figure 6.10: Section of the curved mesh of polynomial degree 4 showing the flow velocity and the element quality: (a) general view; and (b) detailed view.

curved and high-order tetrahedral mesh has been used to obtain a high-order approximation of the flow around a sphere of diameter one. Specifically, we consider the compressible Navier-Stokes solution for the steady-state flow around a sphere at a Reynolds number of $\mathrm{Re} = 200$, and a free-stream Mach number of $M_\infty = 0.3$. Figures 6.10(a) and 6.10(b), present an approximation of the velocity magnitude around the sphere with element-wise polynomials of degree four together with the quality of the curved mesh.

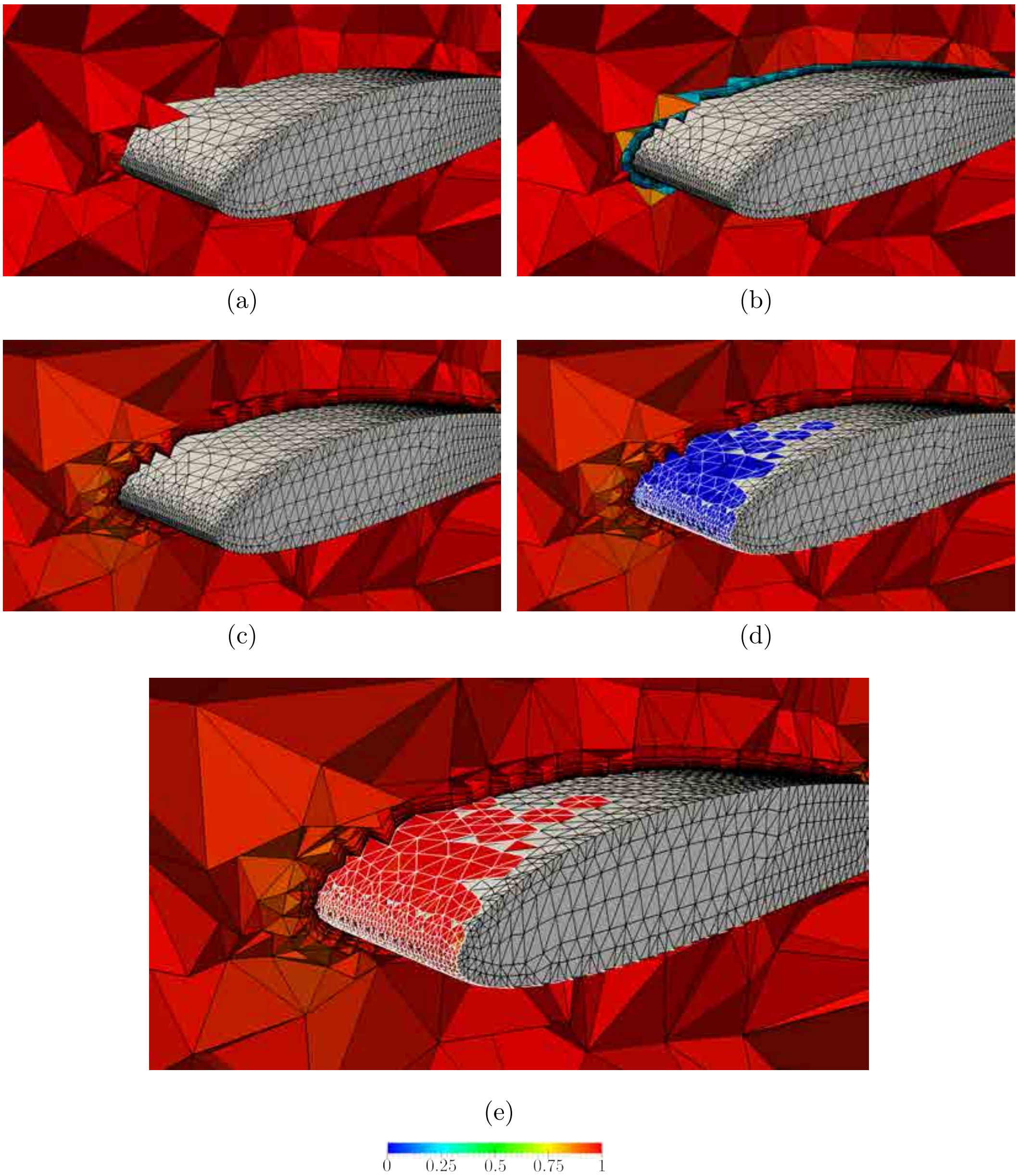
(a)
(b)
(c)
(d)
(e)

Figure 6.11: Steps of the generation of a tetrahedral mesh of polynomial degree 4 with boundary layer around a SD7003 airfoil. (a) Inviscid linear mesh. Viscous linear meshes: (b) inserted boundary layer topology, and (c) smoothed and untangled mesh. Viscous mesh of polynomial degree 4: (d) curved wall boundary, and (e) smoothed and untangled mesh. In Figures (d) and (e) we highlight with white edges the inverted high-order elements that appear in the initial high-order mesh.

Table 6.5: Shape quality statistics of the meshes presented in Figure 6.11.

p	#elems	#nodes	Figure	Min.Q.	Max.Q.	Mean Q.	Std.Dev.	#Inv.
1	7506	12430	6.11(a)	1.00	1.00	1.00	0.00	0
1	121898	22205	6.11(b)	0.00	1.00	0.24	0.18	396
1	121898	22205	6.11(c)	0.70	1.00	0.96	0.04	0
4	121898	1327354	6.11(d)	0.00	1.00	0.93	0.17	3590
4	121898	1327354	6.11(e)	0.21	1.00	0.96	0.04	0

6.3.3.2 Boundary layer around an *SD7003* airfoil

In this section, we illustrate the procedure presented in Section 6.3.3.1 to generate a boundary layer on an *SD7003* airfoil. In Figure 6.11 we present the main steps of the mesh generation procedure. In Figure 6.11(a) we illustrate the isotropic linear mesh, composed by 7506 elements and 12430 nodes. We modify the topology of this mesh by adding 7 anisotropic layers. The height in the orthogonal direction between each layer is twice the height of the previous layer. To reduce the possible inversions in the mesh, the extrusion distance is reduced to the 10 percent of the desired boundary layer height, see Figure 6.11(b). Next, the linear mesh with the inserted layers is smoothed, see Figure 6.11(c), obtaining a valid linear boundary layer mesh. Note that in this smoothed mesh, the boundary layer elements have the desired orthogonal height. Following, the polynomial degree of this mesh is increased to 4, and this mesh is selected as ideal. The resulting high-order mesh is composed by 121898 elements and 169566 nodes. Following, the boundary faces are curved to match the airfoil geometry. Note that since the height of the layers is small close to the size of the airfoil, auto-intersections of the boundary elements appear close to the curved features of the geometry, obtaining an invalid mesh composed by 3590 inverted elements. Finally, the high-order mesh is smoothed and we obtain a final valid boundary layer mesh with a minimum quality of 0.21 and a mean of 0.96. We highlight that the final obtained mesh is composed of curved valid elements of polynomial degree four, and has the desired boundary layer around the target airfoil.

6.4 Concluding remarks

We have presented an *a posteriori* method for generating curved and high-order conformal tetrahedral meshes from CAD models. The main application of the proposed method is to obtain valid meshes ready to be used by any continuous or discontinuous unstructured high-order solver that features tetrahedral elements. The proposed *a posteriori* method is divided in several steps. First, we generate a linear mesh with the desired size and shape of the elements. Note that this initial mesh can be generated with any unstructured tetrahedral mesher. Second, we increase the polynomial degree of the mesh, and we set this straight-sided mesh as ideal (since it has the desired polynomial degree, shape and size). Third, we curve and optimize the boundary faces to ensure a valid boundary configuration. This step is of the major importance, since to obtain a valid volume mesh, it is mandatory to obtain a valid surface mesh, see Chapter 5 for details. Finally, we relocate the inner nodes of the using the non-linear least-squares optimization of the regularized distortion measure presented in Chapter 4.

We want to highlight that to apply the smoothing and untangling method it is required that the following meshes are valid: the initial tetrahedral mesh (determines the ideal mesh), and the curved and high-order surface mesh (determines the boundary conditions). Note that these requirements arise from the first and second step of any *a posteriori* method.

In addition, we have shown trough the examples that the obtained meshes fulfill the requirements to perform a simulation with an unstructured and high-order solver. That is, the meshes are composed by valid elements that are curved to approximate the boundaries of the domain. First, we have generated a triangular mesh of polynomial degree seven and we have illustrated a wave propagation computed using the generated mesh. Second, we have generated a curved tetrahedral mesh to obtain an HDG solution of the steady state of the inviscid flow around a Falcon aircraft. Both the curved mesh and the approximation of the solution have been approximated with element-wise polynomials of degree four. Note that for the same geometry, a straight-sided mesh does not allow the convergence of the HDG solver to a solution of polynomial degree four. According to Bassi and Rebay (1997), we have checked that is mandatory to use curved meshes to obtain physically meaningful solutions of the Euler equations.

Finally, we have presented an *a posteriori* approach for generating curved high-order tetrahedral meshes for viscous flow simulations. The approach provides high-order meshes that include a boundary layer mesh composed by tetrahedra that are: curved, valid, and of any polynomial degree. Moreover, the approach enables the construction of a Navier-Stokes boundary layer mesh (viscous) from an isotropic Euler mesh (inviscid). The main application of this method is to compute with high-fidelity the flow around curved objects. That is, the curved and high-order boundary layer mesh allows the proper representation of the viscous features of the flow close to the wall conditions.

Chapter 7

Summary and future work

7.1 Summary

In this thesis, we have considered four partial goals addressed to validate and generate planar, surface, and volumetric curved high-order meshes from CAD models. We have presented in detail the methods developed to accomplish these goals in the central chapters of this dissertation. Therefore, below we summarize the main contributions of this thesis:

1. **We have proposed a new definition of distortion and quality measures to validate planar and volumetric high-order meshes.** In Chapter 3, we present a procedure to quantify the distortion (quality) of a high-order mesh composed by curved elements. First, we define a point-wise measure of the distortion of a mesh, in terms of the standard Jacobian-based distortion measures for linear elements. Next, we define an element and a mesh quality measure. The defined measures are valid for meshes of any polynomial degree. Specifically, they allow detecting the validity of a high-order element. The quality measure assigns a value of zero to an invalid high-order element, and a value of one if the element is ideal (has the desired shape and node distribution). In particular, we show that if an element has quality greater than zero, the region where the determinant of the representation mapping is lower or equal to zero has measure zero. Moreover, we also show that the measure inherits from the Jacobian-based measure its invariance under affine mappings. Finally, we

present several results to illustrate the application of the proposed measures. First, we analyze the behavior of the developed measures. Second, we show that the quality measure can be used to validate isotropic and boundary layer meshes.

Chapter 3 corresponds to an extension of the peer reviewed conference paper Gargallo-Peiró, Roca, Peraire, and Sarrate (2014a). This work has been invited for publication in the 22nd International Meshing Roundtable special issue of Engineering with Computers (Gargallo-Peiró, Roca, Peraire, and Sarrate, 2014b).

2. **We have proposed a novel robust untangling and smoothing procedure to curve planar and volumetric curved high-order meshes.** In Chapter 4, we propose a smoothing and untangling algorithm to curve high-order meshes. Specifically, we derive a non-linear optimization of a regularized measure of the mesh distortion where the unknowns are the coordinates of the interior mesh nodes.

   The proposed algorithm repairs invalid curved meshes (untangling), ensures that initially valid configurations remain valid after transformation (consistency), deals with arbitrary polynomial degrees (high-order), and preserves some geometrical features of the initial linear mesh (shape, stretching, size, straight-sided interior elements). These properties of the method are demonstrated through examples. Specifically, the examples show that the implementation of the proposed method is capable of handling situations in which the initial mesh contains a large number of invalid elements (robustness) for: polynomial approximations up to degree ten, large deformations of the curved boundaries, concave boundaries, and highly stretched boundary layer elements.

   Chapter 4 corresponds to an extension of the peer reviewed conference paper Roca, Gargallo-Peiró, and Sarrate (2012). This extended work has already been submitted for publication (Gargallo-Peiró, Roca, Peraire, and Sarrate, 2014c).

3. **We have proposed a new framework to validate and generate curved high-order meshes with the nodes on CAD surfaces.** In Chapter 5, we present a new definition of distortion (quality) measure for high-order elements of any polynomial degree with the nodes on CAD parameterized surfaces. The proposed measure is expressed in terms of the parametric coordinates of the

nodes. We use the measures to validate high-order surface meshes and to derive a simultaneous smoothing and untangling procedure. The distortion measure is regularized to allow untangling invalid elements. In particular, the minimization is performed in terms of the parametric coordinates of the nodes, ensuring that the nodes always lie on the surface. Moreover, the developed technique is independent of the selected parameterization. Hence, our method is specially suited for CAD surface representations, even when low-quality parameterizations determine the different patches. Finally, we use the derived optimization framework to generate valid and high-quality surface meshes by an *a posteriori* procedure.

Chapter 3 corresponds to the generalization to high-order meshes of the work presented in Gargallo-Peiró, Roca, and Sarrate (2014). Moreover, it corresponds to the peer reviewed conference paper Gargallo-Peiró, Roca, Peraire, and Sarrate (2013a). We highlight that the proposed technique was acknowledged with the Meshing Maestro Award at the 2012 International Meshing Roundtable.

4. **We have detailed a new a posteriori method to generate valid curved high-order meshes from CAD models for simulation with high-order methods.**

   In Chapter 6, an *a posteriori* method for generating curved high-order conformal meshes from CAD models is presented. The main purpose of the generated meshes is to perform finite element analysis with unstructured high-order solvers. Hence, the generated high-order mesh must be composed of valid elements that are curved to approximate the boundaries of the domain. To this end, we use the smoothing and untangling procedures for volumetric and surface meshes presented in Chapters 4 and 5, respectively, to convert an initial linear mesh (ideal) to a valid curved high-order mesh that matches the boundary CAD geometry.

   Moreover, we have showed that the proposed method can be used to generate valid curved high-order meshes from CAD models suitable for finite element analysis with high-order unstructured methods. Specifically, we have obtained three different curved high-order meshes that have been used to obtain an approximated solution for three different partial differential equations. First, we have generated a triangular mesh of polynomial degree seven of the Barcelona harbor for a 2D wave propagation problem. Second, we have generated a tetrahedral mesh of polynomial degree four on the exterior domain of a Falcon aircraft for an inviscid flow simulation. Finally, we have generated a high-order mesh with a curved boundary layer for 3D viscous flow simulation. Specifically, we have developed a procedure to insert a curved boundary layer to an initial linear isotropic mesh. In particular, we have tested the proposed approach to generate meshes with stretching ratios up to $1 : 10^4$. To validate the obtained meshes the steady-state flow of the compressible Navier-Stokes equations around a sphere is computed.

The technique presented in Chapter 6 to transform an inviscid linear mesh to a viscous curved high-order mesh was presented in Gargallo-Peiró, Roca, Peraire, and Sarrate (2013b).

7.2 Future work

Several extensions of the methods presented in this thesis, together with new ideas, are left to be further investigated in the near future:

1. **Improvement of the performance of the smoothing and untangling procedure.** The main goal of the thesis has been to develop a robust method that can be used to generate valid curved meshes of any polynomial degree. The analysis of the computational time and efficiency of the developed procedures has been out of the scope and of the schedule. However, the proposed *a posteriori* procedure and, more specifically, the stated optimization process involve many components that can be improved in order to reduce the computational cost of the global method. Among the main components, we should improve the implementation of the global and local solvers. In particular, to accelerate the global solver we could consider a parallel Newton-Krylov solver (*e.g.* GMRES) preconditioned with a proper algebraic domain decomposition method. Moreover, the nature of the local implementation of the proposed global optimization method allows coloring the mesh nodes in order to parallelize the code, which could bring a significant speed-up.

2. **Extension of the mesh generation technique to other high-order methods.** The presented quality measures, optimization procedure, and the *a poste-*

riori mesh generation approach can be extended to other types of representations for curved elements. Although in this thesis we have focused on examples of meshes featuring triangles and tetrahedra, we have already demonstrated that changing the element representation we can extend all the presented techniques to quadrilaterals and hexahedra, see Figures D.4 and D.5.

We highlight that in the near future, we would like to extend this formulation to generate meshes for other representations of curved elements. Particularly for hexahedra, changing the function spaces from a polynomial representation to NURBS or B-splines, the proposed definitions could be extended to curved elements for the isogeometrical analysis method (Hughes et al., 2005; Höllig et al., 2012). Differently, changing also the representation of the physical element in terms of the ideal element, the quality measures can be applied for the homotopy-based representation for tetrahedral elements bounded by NURBS used in NEFEM (Sevilla et al., 2011).

3. **Improvements on the technique to transform an isotropic mesh into a boundary layer mesh.** In Section 6.3.3, we have developed a technique to transform an inviscid mesh to a viscous mesh by means of extruding the boundary faces according to a given stretching ratio. However, we have considered a unique extrusion template for all surface faces. In order to widen the set of considered geometry configurations, we should develop new templates for face extrusion according to the type of edges and vertices surrounding a face. For a given face, the edges are classified according to the angle defined by their adjacent faces into *end*, *side*, *corner*, or *reversal*, see Roca (2009) and Ruiz-Gironés (2011). In an analogous manner, we can classify the vertices of each face. Hence, considering specific templates for each geometrical face configuration, we would enhance the quality of the obtained curved high-order boundary layer meshes.

4. **Adaptivity for high-order meshes.** Generating highly anisotropic meshes using the proposed *a posteriori* approach has been out of the scope of this thesis. Nevertheless, we have shown that boundary layer meshes with stretching ratios up to $1 : 10^4$ can be obtained by the current implementation of the method. On the contrary, we have observed that when the initial linear mesh has stretching ratios of $1 : 10^9$, the implemented version of the proposed mesh optimization

does not converge to a valid curved high-order mesh. This issue was identified and reported to us by Phil Caplan and David Darmofal (Department of Aeronautics and Astronautics, Massachusetts Institute of Technology). It seems that this drawback is governed by some numerical issues that prevent the method to converge. Specifically, we have planned to determine the specific origin of this numerical instabilities. In this manner, we could consider the proper modification of the implementation of the smoothing and untangling algorithm to ensure that anisotropic meshes with high stretching ratios can be curved. Further research should be developed for the regularized optimization method in order to: increase the robustness, improve the numerical stability, and reduce the perturbation induced by the regularization of the objective function.

5. **Continuity of the derivatives in the surface mesh.** In the existing approaches to generate high-order 3D meshes and, in particular, in the approach presented in this work, the face elements in the boundary of the mesh are $\mathcal{C}^0$ continuous. Ensuring also the continuity of the normal vector between adjacent face elements could enhance the quality of the obtained meshes. That is, the resulting meshes would reduce, in the simulation, the generation of the artificial entropy originated from the approximation of the curved boundaries (Bassi and Rebay, 1997). To this end, we have considered to develop a least-squares optimization algorithm that minimizes the distortion but that, at the same time, enforces that the surface mesh is $\mathcal{C}^1$.

Appendix A

Nodal high-order elements

The main goal of this work is the validation and generation of nodal high-order meshes. Therefore, in this section we detail the representation of nodal high-order elements. Let E^P in $\mathcal{M}_P$ be a nodal high-order element of interpolation degree p determined by n_p nodes with coordinates $\mathbf{x}_i$ in $\mathbb{R}^{d_x}$, for $i = 1, \ldots, n_p$ (d_x denotes the dimension of the physical space). Note that the number of element nodes n_p depends on the selected element type and the desired interpolation degree p:

- Triangle: $n_p = \frac{1}{2}(p+1)(p+2)$
- Quadrilateral: $n_p = (p+1)^2$
- Tetrahedron: $n_p = \frac{1}{6}(p+1)(p+2)(p+3)$
- Hexahedron: $n_p = (p+1)^3$

In addition, we use a node distribution that provides a quasi-optimal Lebesgue constant (Warburton, 2006; Hesthaven and Warburton, 2007). Given a master element E^M with nodes $\boldsymbol{\xi}_j$ in $\mathbb{R}^{d_\xi}$, being $j = 1, \ldots, n_p$ (d_ξ denotes the master space dimension), we consider the basis $\{N_i\}_{i=1,\ldots,n_p}$ of nodal shape functions (Lagrange interpolation) of degree p. Then, the high-order representation mapping from E^M to E^P, see Figure A.1, can be expressed as:

$$\begin{aligned} \boldsymbol{\phi}_P : \quad E^M \subset \mathbb{R}^3 \quad &\longrightarrow \quad E^P \subset \mathbb{R}^3 \\ \boldsymbol{\xi} \qquad\quad &\longmapsto \quad \mathbf{x} = \boldsymbol{\phi}_P(\boldsymbol{\xi}) = \sum_{i=1}^{n_p} \mathbf{x}_i N_i(\boldsymbol{\xi}). \end{aligned} \tag{A.1}$$

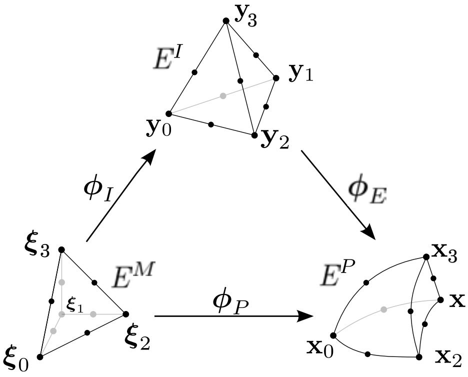

Figure A.1: Mappings between the master, ideal and physical nodal high-order elements.

The Jacobian of the iso-parametric mapping, Equation (A.1), is the matrix

$$\mathbf{D}\boldsymbol{\phi}_P(\boldsymbol{\xi}) = \sum_{i=1}^{n_p} \mathbf{x}_i \boldsymbol{\nabla} N_i(\boldsymbol{\xi}) \in \mathbb{R}^3 \times \mathbb{R}^3.$$

Similar to the linear case, we define the high-order mapping $\boldsymbol{\phi}_I$ from the master element, E^M, to the ideal element, E^I. Then, the mapping $\boldsymbol{\phi}_E = \boldsymbol{\phi}_P \circ \boldsymbol{\phi}_I^{-1}$ from each ideal element, E^I, to the corresponding physical element, E^P, in the high-order mesh can be expressed as

$$\begin{array}{rcccl} \boldsymbol{\phi}_E : & E^I \subset \mathbb{R}^3 & \longrightarrow & E^P \subset \mathbb{R}^3 & \\ & \mathbf{y} & \longmapsto & \mathbf{x} = \boldsymbol{\phi}_E(\mathbf{y}) = \displaystyle\sum_{i=1}^{n_p} \mathbf{x}_i N_i(\boldsymbol{\phi}_I^{-1}(\mathbf{y})). & \end{array} \tag{A.2}$$

As described in Section 4.1, for a given element in the physical mesh we always choose its corresponding element in the initial straight-sided mesh as the ideal element. Therefore, $\boldsymbol{\phi}_I$ is an affine mapping. However, for high-order elements, the mapping $\boldsymbol{\phi}_P$ presented in Equation (A.1), is not affine in general. Hence, $\boldsymbol{\phi}_E = \boldsymbol{\phi}_P \circ \boldsymbol{\phi}_I^{-1}$ is also not affine, and the Jacobian matrix is not constant. Specifically, for a point $\mathbf{y}$ in the initial element, the expression of the Jacobian is:

$$\mathbf{D}\boldsymbol{\phi}_E(\mathbf{y}) = \mathbf{D}\boldsymbol{\phi}_P(\boldsymbol{\phi}_I^{-1}(\mathbf{y})) \cdot \mathbf{D}\boldsymbol{\phi}_I^{-1}(\mathbf{y}).$$

Appendix B

Numerical optimization

To solve the optimization problems presented in Equations (4.11) and (5.22), we can choose a global or a local approach. For small problems solving the global system resulting from assembling the contributions of all the elements works well. If the problem is too large and we want to reduce the memory requirements, we choose a non-linear iterative method that: exploits the locality of the problem, avoids solving large linear systems, and is well suited for parallelization (by coloring the mesh nodes). Specifically, we use a non-linear iterative Gauss-Seidel method determined by the iteration

$$\mathbf{x}_i^{k+1} = \mathbf{x}_i^k - \alpha_i^k \; [\boldsymbol{\nabla}_{ii}^2 f(\mathbf{w}_i^k)]^{-1} \; \boldsymbol{\nabla}_i f(\mathbf{w}_i^k) \qquad i = 1, \ldots, n_F, \tag{B.1}$$

where α_i^k is the step length, and

$$\mathbf{w}_i^k = (\mathbf{x}_1^{k+1}, \ldots, \mathbf{x}_{i-1}^{k+1}, \mathbf{x}_i^k, \mathbf{x}_{i+1}^k, \ldots, \mathbf{x}_{n_F}^k; \mathbf{x}_{n_F+1}^0, \ldots, \mathbf{x}_{n_N}^0)$$

is the vector of updated node locations for the $i-1$ first nodes. Note that $\boldsymbol{\nabla}_i$ and $\boldsymbol{\nabla}_{ii}^2$ denote the gradient and the Hessian with respect to the coordinates $\mathbf{x}_i$ of node i.

To implement this iterative non-linear solver, we have to compute the gradient $\boldsymbol{\nabla}_i f$, the Hessian $\boldsymbol{\nabla}_{ii}^2 f$, and the step length, α_i^k. According to Equation (4.10) and taking into account Equation (4.5), the computation of the gradient

$$\begin{aligned}
\boldsymbol{\nabla}_i f(\mathbf{x}_1, \ldots, \mathbf{x}_{n_F}; \mathbf{x}_{n_F+1}, \ldots, \mathbf{x}_{n_N}) &= \frac{\partial}{\partial \mathbf{x}_i} \sum_{e=1}^{n_E} \| \mathrm{M} \boldsymbol{\phi}_{E_e} - 1 \|_{E_e^I}^2 \\
&= \sum_{e=1}^{n_E} \frac{\partial}{\partial \mathbf{x}_i} \int_{E_e^I} (\mathrm{M} \boldsymbol{\phi}_{E_e}(\mathbf{y}) - 1)^2 \mathrm{d}\mathbf{y},
\end{aligned}$$

Algorithm B.1 Backtracking Line Search

```
1: function BackLineSearch(Vector $\mathbf{w}_i^k$, Vector $\mathbf{p}_i^k$)
2:     Set $\alpha > 0,\ \rho \in (0,1),\ c \in (0,1)$;
3:     $\mathbf{w}_i^\alpha \leftarrow \mathbf{w}_i^k + (\mathbf{0}, \dots, \mathbf{0}, \alpha \mathbf{p}_i^k, \mathbf{0}, \dots, \mathbf{0})$;
4:     while $f(\mathbf{w}_i^\alpha) > f(\mathbf{w}_i^k) + c\alpha [\boldsymbol{\nabla}_i f(\mathbf{w}_i^k)]^T \mathbf{p}_i^k$ do
5:         $\alpha \leftarrow \rho\alpha$;
6:         $\mathbf{w}_i^\alpha \leftarrow \mathbf{w}_i^k + (\mathbf{0}, \dots, \mathbf{0}, \alpha \mathbf{p}_i^k, \mathbf{0}, \dots, \mathbf{0})$;
7:     end while
8:     return $\alpha$;
9: end function
```

can be simplified. That is, $\int_{E_e^I} (\eta(\mathbf{D}\boldsymbol{\phi}_{E_e}(\mathbf{y}) - 1)^2 \mathrm{d}\mathbf{y}$ only depends on the coordinates of the nodes of the element E_e^P. Therefore, we have that

$$\frac{\partial}{\partial \mathbf{x}_i} \int_{E_e^I} (\mathrm{M}\boldsymbol{\phi}_{E_e}(\mathbf{y}) - 1)^2 \mathrm{d}\mathbf{y} = \frac{\partial}{\partial \mathbf{x}_i} \int_{E_e^I} \left(\eta \left(\mathbf{D}\boldsymbol{\phi}_{E_e}(\mathbf{y})\right) - 1\right)^2 \mathrm{d}\mathbf{y} = 0$$

for all the elements that do not contain the node i. Thus, the gradient can be evaluated as

$$\boldsymbol{\nabla}_i f(\mathbf{x}_1, \dots, \mathbf{x}_{n_F}; \mathbf{x}_{n_F+1}, \dots, \mathbf{x}_{n_N}) = \sum_{e \sim i} \frac{\partial}{\partial \mathbf{x}_i} \int_{E_e^I} (\mathrm{M}\boldsymbol{\phi}_{E_e}(\mathbf{y}) - 1)^2 \mathrm{d}\mathbf{y},$$

where $e \sim i$ denotes that the summation is performed only for the elements that contain the node i. Therefore, if we define

$$\hat{f}(\mathbf{x}_i) := \sum_{e \sim i} \int_{E_e^I} (\mathrm{M}\boldsymbol{\phi}_{E_e}(\mathbf{y}) - 1)^2 \mathrm{d}\mathbf{y} = \sum_{e \sim i} \|\mathrm{M}\boldsymbol{\phi}_{E_e} - 1\|_{E_e^I}^2, \tag{B.2}$$

we have that

$$\boldsymbol{\nabla}_i f(\mathbf{x}_1, \dots, \mathbf{x}_{n_F}; \mathbf{x}_{n_F+1}, \dots, \mathbf{x}_{n_N}) = \boldsymbol{\nabla}_i \hat{f}(\mathbf{x}_i)\ . \tag{B.3}$$

Moreover, the Hessian can be computed as

$$\boldsymbol{\nabla}_{ii}^2 f(\mathbf{x}_1, \dots, \mathbf{x}_{n_F}; \mathbf{x}_{n_F+1}, \dots, \mathbf{x}_{n_N}) = \boldsymbol{\nabla}_{ii}^2 \hat{f}(\mathbf{x}_i)\ . \tag{B.4}$$

Finally, we have to compute the step length α_i^k. To this end, we use the Backtracking Line Search algorithm (Nocedal and Wright, 1999) detailed in Algorithm B.1, where we set: $\alpha = 1$, $\rho = 0.5$ and $c = 10^{-4}$. Note that in this algorithm, we have to evaluate the global objective function f and its gradient to check the sufficient decrease condition in Line 4. From Equation (B.3), the sufficient decrease condition is equivalent to

$$f(\mathbf{w}_i^\alpha) > f(\mathbf{w}_i^k) + c\alpha [\boldsymbol{\nabla}_i \hat{f}(\mathbf{x}_i^k)]^T \mathbf{p}_i^k,$$

where $\mathbf{w}_i^\alpha$ is defined in Line 3 of Algorithm B.1. Moreover, we have that

$$f(\mathbf{w}_i^\alpha) - f(\mathbf{w}_i^k) = \hat{f}(\mathbf{x}_i^\alpha) - \hat{f}(\mathbf{x}_i^k),$$

since the contributions of the elements that do not depend on the free node are mutually cancelled, being $\mathbf{x}_i^\alpha = \mathbf{x}_i^k + \alpha \mathbf{p}_i^k$. Therefore, the sufficient decrease condition is equivalent to

$$\hat{f}(\mathbf{x}_i^\alpha) > \hat{f}(\mathbf{x}_i^k) + c\alpha[\boldsymbol{\nabla}_i \hat{f}(\mathbf{x}_i^k)]^T \mathbf{p}_i^k. \tag{B.5}$$

Taking into account Equation (B.3), (B.4), and (B.5), we observe that we only need to compute the gradients, the Hessian, and the value of the local function $\hat{f}$ introduced in Equation (B.2).

In our implementation, we exploit the computational reduction associated with the evaluation of the function $\hat{f}$. To this end, we denote by $\mathcal{M}_\mathbf{x}$ the elements that contain a free node $\mathbf{x}$. The set of elements $\mathcal{M}_\mathbf{x}$ is referred as the *submesh* associated with node $\mathbf{x}$.

Remark B.1. *Let $\mathbf{x}_i^k$ be the coordinates of node i at step k, and let $\mathcal{M}_{\mathbf{x}_i^k}$ be the corresponding associated submesh composed by m_i elements. We say that*

$$\hat{f}(\mathbf{x}_i) = \sum_{e\sim i} \|\mathrm{M}\boldsymbol{\phi}_{E_e} - 1\|^2_{E_e^I} = \sum_{e\sim i} \int_{E_e^I} (\mathrm{M}\boldsymbol{\phi}_{E_e}(\mathbf{y}) - 1)^2 d\mathbf{y} = \sum_{e=1}^{m_i} \int_{E_e^I} (\mathrm{M}\boldsymbol{\phi}_{E_e}(\mathbf{y}) - 1)^2 d\mathbf{y}$$

is a local merit function that measures the deviation respect an ideal configuration of the submesh distortion associated with $\mathbf{x}_i$. *According to this merit function, and to Equations* (B.3)*,* (B.4)*, and* (B.5)*, we can implement the iteration $k+1$ for node i of the proposed non-linear method, Equation* (B.1)*, as*

$$\mathbf{x}_i^{k+1} = \mathbf{x}_i^k - \alpha_i^k \; [\boldsymbol{\nabla}^2_{ii} \hat{f}(\mathbf{x}_i^k)]^{-1} \; \boldsymbol{\nabla}_i \hat{f}(\mathbf{x}_i^k) \qquad i = 1, \ldots, n_F.$$

Appendix C

Initial configuration: *p*-continuation

In this section, we detail a *p*-continuation procedure to improve the initial configuration of a high-order invalid mesh for the optimization procedure presented in Section 4.1.3. The proposed approach is composed by three steps.

First, we generate a linear mesh by decomposing each high-order element into several structured linear elements determined by the high-order nodes. Specifically, each triangle of polynomial degree p is decomposed into $\mathcal{O}(p^2)$ linear triangles, and each high-order tetrahedron into $\mathcal{O}(p^3)$ linear tetrahedra. The obtained linear mesh has the same nodes of the high-order mesh. Moreover, we assign to each linear sub-element a different ideal linear element. The ideal element associated to each sub-element is the corresponding sub-element of the ideal high-order element. In Figure C.1 we show the linear decomposition of a triangle and a tetrahedron, both of polynomial degree four.

The second step is the optimization of the linear sub-mesh using an objective function based on the distortion measure for linear elements presented in Equation (3.6). Since the linear sub-mesh can also contain inverted elements, it is mandatory that the optimization method for linear elements also allows untangling invalid meshes. To meet this requirement, in this work, we use the optimization technique presented in Escobar et al. (2003) and Gargallo-Peiró et al. (2014). Finally, in the third step we recover the high-order mesh by updating the location of the nodes.

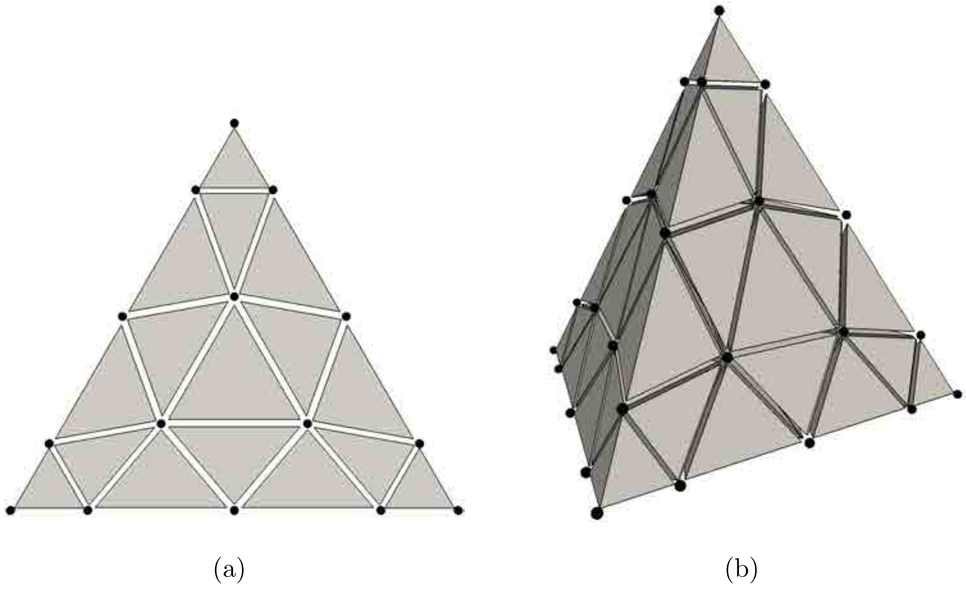

Figure C.1: Decomposition of a triangle and a tetrahedral elements of polynomial degree four into the corresponding linear sub-elements.

Note that an untangled linear sub-mesh is a necessary condition to have a valid high-order mesh. Therefore, we only apply our procedure when this necessary condition is not hold, *i.e.* if the linear sub-mesh has invalid elements. In this context, our procedure guarantees that the quality of the initial high-order configuration is improved, since it obtains an untangled linear sub-mesh. We highlight that having a valid linear sub-mesh is a necessary, but not sufficient, condition. Hence, the updated high-order mesh can still be invalid after this procedure. Note that this is not the case of the example presented in Figure C.2, where the final high-order mesh is also untangled. However, since the validity of the high-order mesh can not be guaranteed with this procedure, it is required to use the high-order optimization process presented in Section 4.1.3 to obtain a valid and high-quality high-order mesh.

To illustrate the p-continuation process, in Figure C.2 we show a triangular mesh of polynomial degree four on a circular ring. Figure C.2(a) presents the initial high-order mesh obtained after curving the boundary edges of the high-order ideal mesh. Next, in Figure C.2(c) we show the initial linear sub-mesh generated by decomposing the high-order elements. Note that the high-order mesh has four invalid elements, and the corresponding linear sub-mesh has twelve tangled triangles. Figure C.2(d) displays the optimized linear sub-mesh. Notice that it does not contain inverted

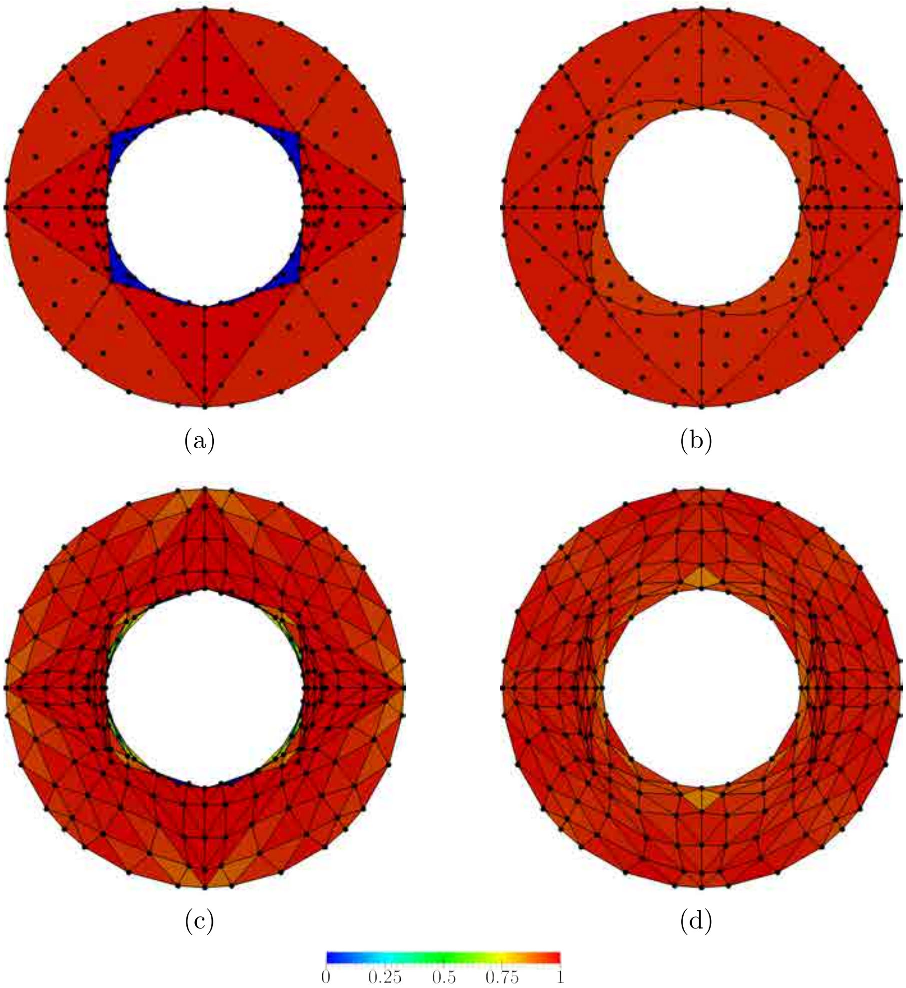

Figure C.2: Procedure to find an initial mesh configuration. High-order meshes: (a) initial invalid configuration, (b) mesh configuration obtained with the smoothing of the linear sub-mesh. Linear sub-meshes: (c) initial invalid configuration, (d) optimized configuration.

elements. Finally, in Figure C.2(b) the high-order mesh is recovered. Note that the quality of this mesh configuration has been improved with respect to the initial one, and that it does not contain any invalid elements. This high-order mesh is the input of the optimization procedure presented in Section 4.1.3.

For this example, using the p-continuation procedure saves more than half of the total computational cost of using just the high-order method. For the presented 2D mesh of polynomial degree four, we have checked that each global iteration of the linear mesh represents a half of the cost of the high-order one. On the one hand, if we directly run the high-order method, we require 82 iterations. On the other hand, the p-continuation process requires 55 iterations, and the high-order optimization just 6 more. Hence, the p-continuation brings an speed-up of about 2.21 of the procedure using just the high-order optimization.

Appendix D

Validation and generation of high-order triangular, quadrilateral and hexahedral meshes

---

In this appendix, we illustrate that, according to Remark 3.4, we can change the element representation to extend the distortion measure, the derived optimization procedure and the *a posteriori* approach to high-order triangle, quadrilateral and hexahedral meshes.

D.1 Curved high-order triangular meshes

Circular ring. In the first example, we generate four meshes of orders 3, 4, 5 and 10 for a circular ring, see Figure D.1. The meshes are composed by 24 elements. The number of nodes depends on the selected order: 126 nodes for order 3, 216 nodes for order 4, 330 nodes for order 5, and 1260 nodes for order 10. All the initial meshes have the same straight inner edges and only differ on the degree of the polynomial approximation of the boundary. Figure D.1(a) shows the initial mesh for order 3 displaying also the quality of its elements. Note that the inner edges of this mesh are straight. Therefore, several tangled elements appear at the inner boundary. Figure D.1(b) shows a detail of the upper-right inner boundary of this initial mesh, where a tangled element with null quality appears.

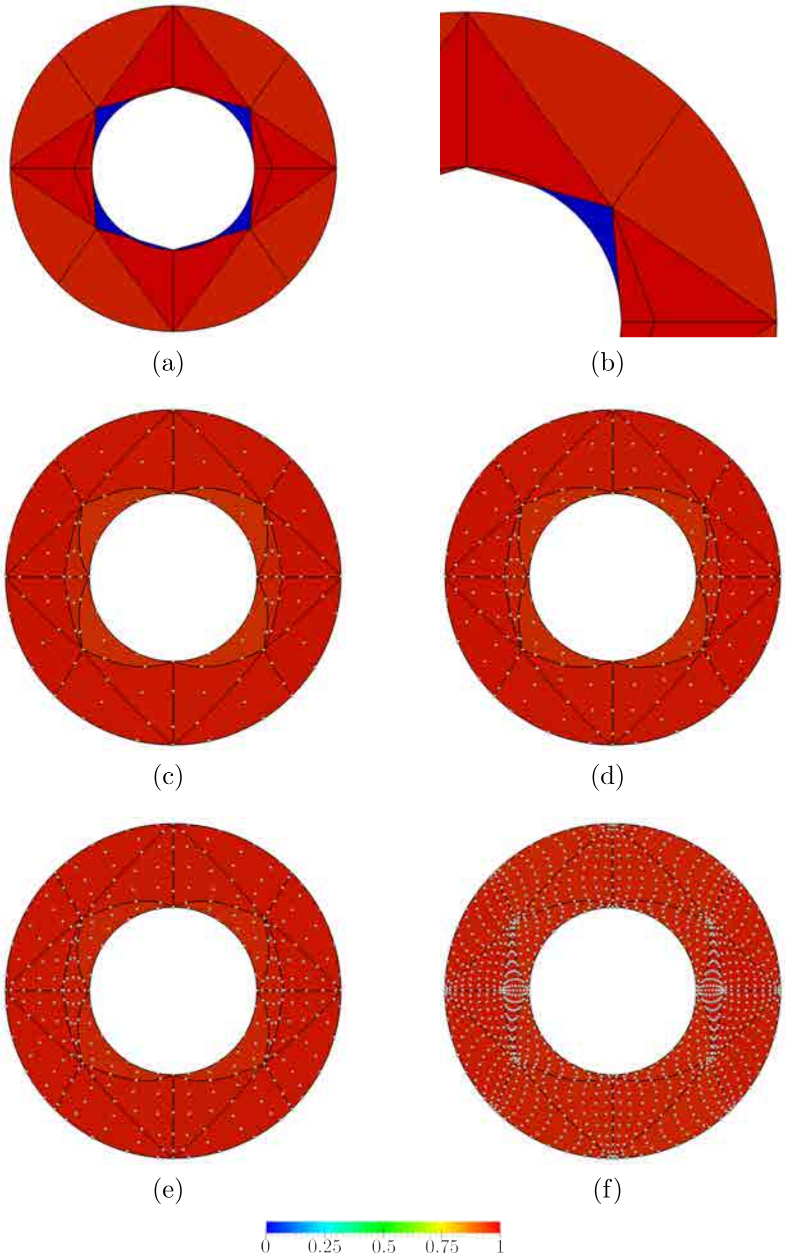

Figure D.1: High-order meshes for the ring: (a) and (b) the initial mesh ($p = 10$); and smoothed and untangled meshes for (c) $p = 3$, (d) $p = 4$, (e) $p = 5$, and (f) $p = 10$.

Figure D.1 shows the initial non-valid meshes and the final optimized meshes. Table D.1 shows the quality statistics for each one of the presented rings. Recall that the quality values of each ring are not comparable, since the definition of the quality

Figure	p	Min.	Max.	Mean	Std.Dev.	#inv
D.1(a)	3	0.00	0.96	0.70	0.31	4
D.1(c)	3	0.94	0.97	0.96	0.01	0
D.1(d)	4	0.94	0.97	0.96	0.01	0
D.1(e)	5	0.95	0.97	0.96	0.01	0
D.1(f)	10	0.95	0.97	0.96	0.01	0

Table D.1: Quality statistics for the circular ring presented in Figure D.1.

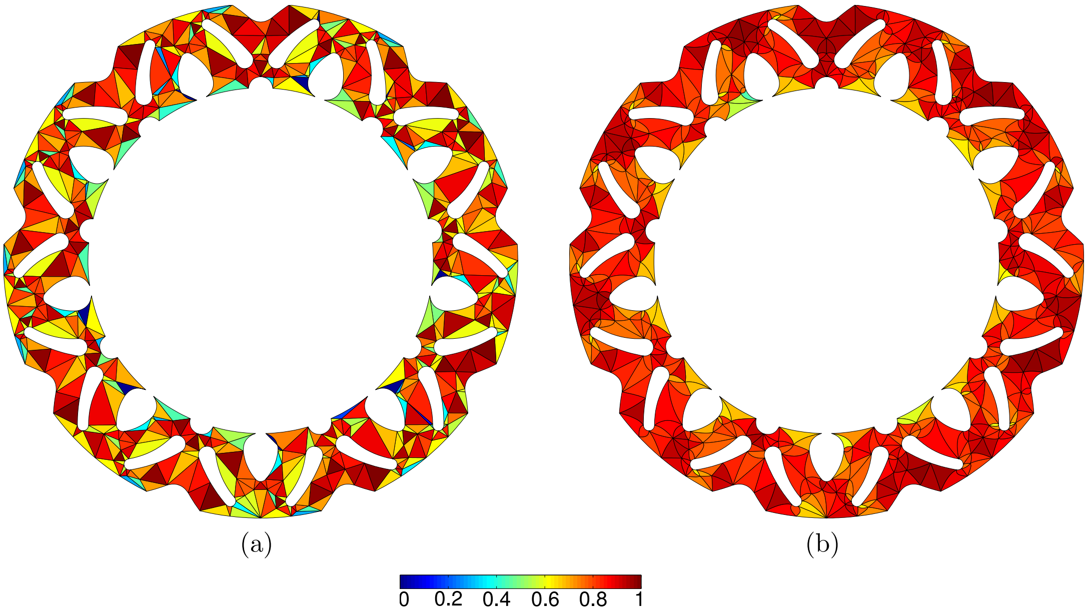
(a)

(b)

Figure D.2: Mesh of polynomial degree 2 composed by triangles for a component of a motorcycle brake: (a) initial mesh, and (b) smoothed meshes.

Meshes	Figure	Min. Q.	Max. Q.	Mean Q.	Std. Dev.	#inv. el.
Initial	D.2(a)	0.00	1.00	0.72	0.19	8
Smoothed	D.2(b)	0.45	0.98	0.83	0.09	0

Table D.2: High order triangular mesh of polynomial order two on a motorcycle brake, composed by 655 elements and 1645 nodes.

for each order changes. It is worth to notice, that for any order, the optimization procedure is able to untangle a degenerated mesh and obtain a high-quality final mesh.

Brake components of a motorcycle. In the second example, we present a planar geometry extracted from a CAD model of a break of a motorbike. We generate an initial linear triangular mesh composed by 655 elements. Next, we increase the polynomial order of the mesh and we curve the boundary to match the geometry, obtaining the initial curved mesh configuration, Figure D.2(a). We can observe that 8 tangled elements appear in the mesh after curving the boundary edges. We highlight that the defined measure detects the invalid elements on the boundary of the geometry. Finally, the regularized distortion measure is used to smooth and untangle the mesh, achieving a final configuration composed by valid elements of a quality over 0.5, Figure D.2(b).

D.2 Curved high-order quadrilateral meshes

In this section, we present the extension to quadrilaterals of the distortion and quality measures, and the corresponding optimization (smoothing and untangling) procedure. First, we analyze the behavior of the defined quality measure for the quadrilateral case. Next, using the proposed optimization procedure, we generate valid curved high-order quadrilateral meshes from planar CAD geometries.

Behavior of the high-order quality measure. In this section, we include for completeness of Section 3.3.1 an analysis of the behavior of the quality measure for a quadrilateral of polynomial degree two with vertices on $(-1,-1)$, $(1,-1)$, $(1,1)$ and $(-1,1)$. In Figure D.3 we plot for the two measures, the contour plots of the high-order quality in terms of a vertex, an edge, and a face node. Note that the behavior of each measure does hold the commentaries underlined for triangles in Section 3.3.1. Recall that differently than for linear elements, the same definition of distortion measure for a high-order element applies to either triangles or quadrilaterals. Moreover, from Figure D.3 we realize that the two displayed high-order measures for quadrilaterals also have the same feasible regions. The defined measure properly detects the validity of the elements, assigning zero quality for folded ones. Specifically, the boundary of the feasible region is the same for all the measures. In addition, the high-order measure also detects the same ideal configuration for the two selected linear distortion measures.

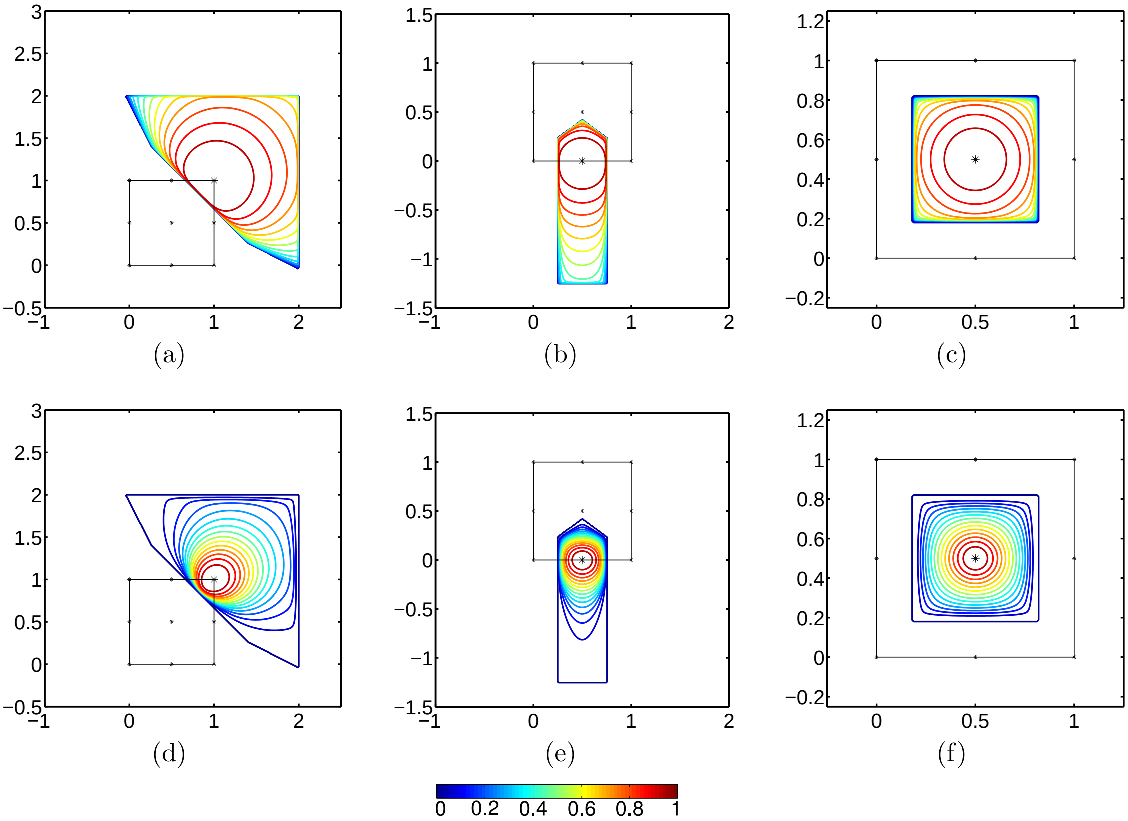

(a) (b) (c)

(d) (e) (f)

Figure D.3: Level sets for the two high-order quality measures (in rows: shape and Oddy) when the free node is: (a,d) the vertex node; (b,e) the edge node; and (c,f) the face node.

Mesh	Figure	Min. Q.	Max. Q.	Mean Q.	Std. Dev.	#inv. el.
Initial	D.4(a)	0.00	1.00	0.92	0.12	3
Smoothed	D.4(b)	0.67	1.00	0.94	0.05	0
Initial Mesh	D.4(c)	0.00	0.99	0.78	0.22	8
Smoothed Mesh	D.4(d)	0.62	0.99	0.83	0.09	0

Table D.3: Quadrilateral meshes of polynomial order 3 presented in Figure D.4.

Brake components of a motorcycle We present two geometries extracted from a CAD model of a break of a motorbike and we mesh them using quadrilaterals of two different polynomial orders. In the first case, the mesh presented is of polynomial order 3 and is composed by 534 elements and 5210 nodes, see Figures D.4(a) and D.4(b). In the second case, the mesh is of polynomial order 4 and composed by 200 elements and 3614 nodes, see Figures D.4(c) and D.4(d). For both geometries

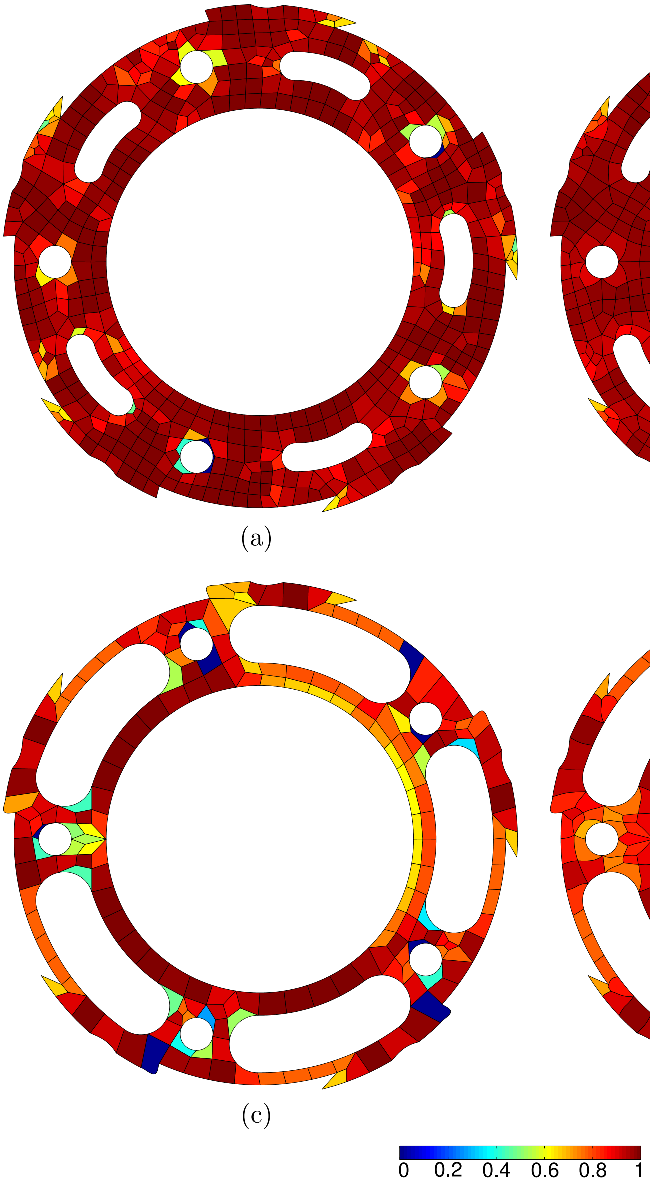

Figure D.4: Details of two quadrilateral meshes of polynomial order 3 and 4, respectively, for a two components of a motorcycle brake: (a,c) initial meshes, (b,d) smoothed meshes.

we have generated coarse linear meshes. Therefore, once the boundary is curved 3 tangled elements appear in first mesh and 8 more in the second one. We observe that the defined measure detects the invalid elements on the boundary of the geometry. In both cases the initial invalid curved mesh is untangled and smoothed, achieving a final configuration composed by all valid elements and quality over 0.5. In Tables

Mesh	Figure	Min. Q.	Max. Q.	Mean Q.	Std. Dev.	#inv. el.
Ideal	D.5(b)	1.00	1.00	1.00	0.00	0
Initial	D.5(c)	0.00	0.00	0.00	0.00	68
Smoothed	D.5(d)	0.96	1.00	0.99	0.005	0

Table D.4: Hexahedral meshes of polynomial order four presented in Figure D.5.

D.3 we present the quality statistics of the presented examples. It is important to point out that with the second geometry, it is necessary to use elements of polynomial order four in order to obtain a valid final configuration. Since the initial linear mesh is coarse, elements of 4th order are required to achieve a curved boundary and a valid mesh with high-quality and no foldings or auto-intersections.

D.3 Curved high-order hexahedral meshes

In this section, we illustrate the *a posteriori* mesh generation approach on hexahedral meshes. Given the CAD geometry presented in Figure D.5(a), we generate an initial linear mesh using the submapping method presented in Ruiz-Gironés and Sarrate (2010). Next, we increase the polynomial order to four and we set this straight-sided high-order mesh as ideal, see Figure D.5(b). Following, we curve the mesh to match the boundary geometry. In order to test the capability of the smoothing and untangling procedure to deal with meshes composed by a large number of inverted elements, we randomly perturb the location of the inner nodes. All the elements of the resulting high-order curved mesh are inverted, see Figure D.5(c). Next, we use the optimization procedure presented in Section 4 to obtain a final high-quality curved mesh, see Figure D.5(d). In Table D.4 we present the quality statistics of the tangled and the smoothed high-order hexahedral. We observe that the quality measure for hexahedral elements is also able to detect the invalid hexahedra, and to assign quality one to the ideal configuration.

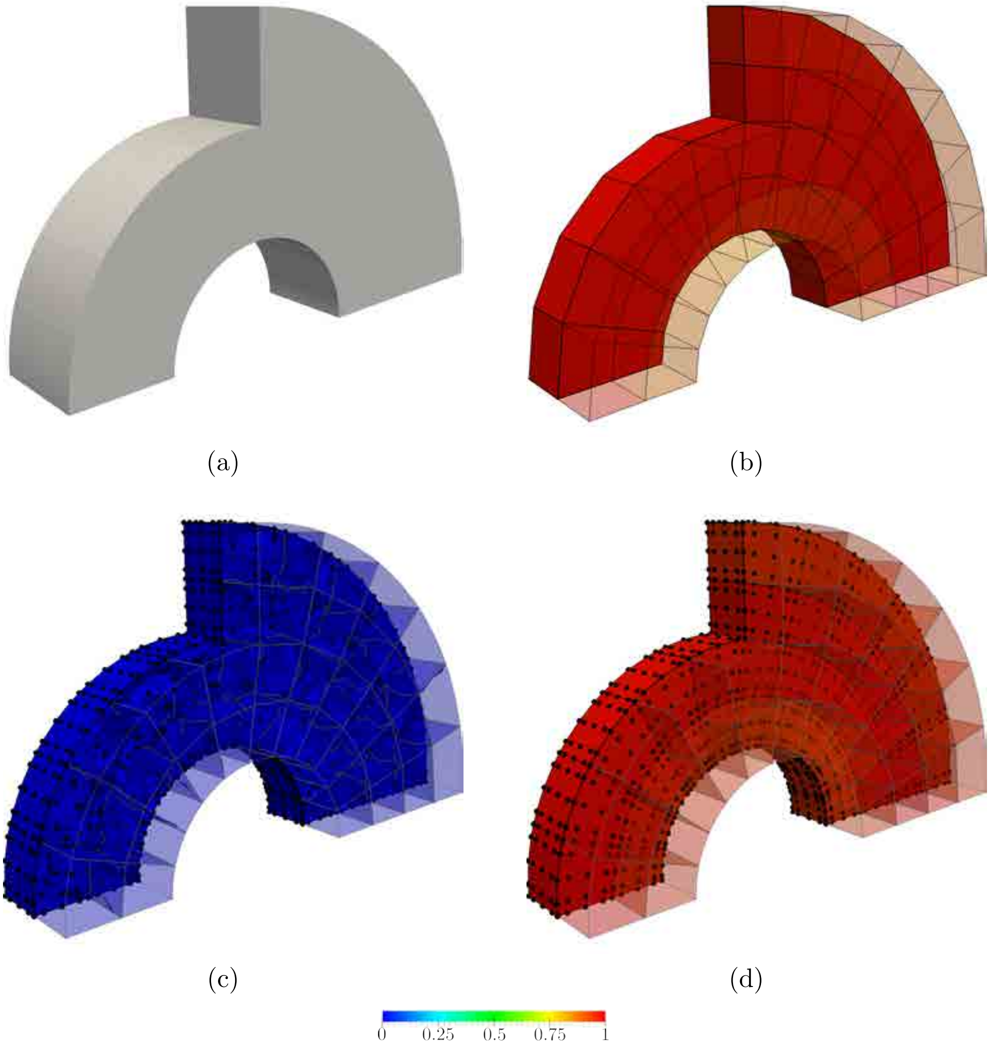

(a) (b)

(c) (d)

Figure D.5: (a) Target CAD geometry to discretize with hexahedra. Tetrahedral meshes of polynomial degree four: (b) ideal straight-sided (c) tangled, and (d) smoothed.

Appendix E

Nodal high-order elements on parameterized surfaces

In this section, we detail the selected element representation in $\boldsymbol{\mathcal{W}}$, see Eq. (5.10). Let E^P in $\mathcal{M}_P$ be a nodal high-order element of polynomial degree p determined by n_p nodes with coordinates $\mathbf{x}_i$ in $\Sigma_P \subset \mathbb{R}^3$, for $i = 1, \ldots, n_p$. Note that for triangular elements the number of nodes n_p is $\frac{1}{2}(p+1)(p+2)$. In addition, to improve the interpolation properties of the obtained high-order elements, we use a node distribution that provides a quasi-optimal Lebesgue constant (Warburton, 2006; Hesthaven and Warburton, 2007). Given a master element E^M with nodes $\boldsymbol{\xi}_j$ in $\mathbb{R}^2$, being $j = 1, \ldots, n_p$, we consider the basis $\{\bar{N}_i\}_{i=1,\ldots,n_p}$ of nodal interpolative shape functions (Lagrange interpolation) of degree p. Then, the high-order representation mapping from E^M to E^P, see Figure E.1, can be expressed as:

$$\begin{aligned} \boldsymbol{\phi}_P : E^M \subset \mathbb{R}^2 &\longrightarrow E^P \subset \mathbb{R}^3 \\ \boldsymbol{\xi} &\longmapsto \mathbf{x} = \boldsymbol{\phi}_P(\boldsymbol{\xi}) = \sum_{i=1}^{n_p} \mathbf{x}_i \bar{N}_i(\boldsymbol{\xi}). \end{aligned} \tag{E.1}$$

Note that $\boldsymbol{\phi}_P(\boldsymbol{\xi})$ can be written as $\boldsymbol{\phi}_P(\boldsymbol{\xi}; \mathbf{x}_1, \ldots, \mathbf{x}_{n_p})$, since it also depends on the node coordinates $\mathbf{x}_1, \ldots, \mathbf{x}_{n_p}$. Moreover, recall that the shape functions $\{\bar{N}_i\}_{i=1,\ldots,n_p}$ depend on the selection of $\boldsymbol{\xi}_j$, for $j = 1, \ldots, n_p$. In addition, they form a partition of the unity on E^M, and hold that $\bar{N}_i(\boldsymbol{\xi}_j) = \delta_{ij}$, for $i, j = 1, \ldots, n_p$.

Analogously, the mapping $\boldsymbol{\phi}_I$ between the master and the ideal elements is also determined using nodal high-order shape functions. Recall that, in this work, we set

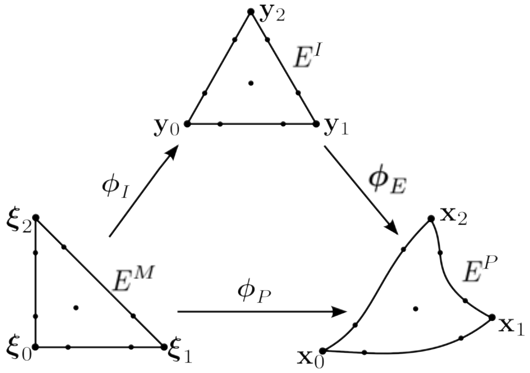

(a)

Figure E.1: Mappings between the master, the ideal and the physical high-order elements. Application to nodal high-order triangles.

the elements of the ideal mesh to be high-order, and straight-sided. Hence, we can write $\boldsymbol{\phi}_I$ as:

$$\begin{aligned} \boldsymbol{\phi}_I : E^M \subset \mathbb{R}^2 &\longrightarrow E^I \subset \mathbb{R}^3 \\ \boldsymbol{\xi} &\longmapsto \mathbf{y} = \boldsymbol{\phi}_I(\boldsymbol{\xi}) = \sum_{i=1}^{n_p} \mathbf{y}_i \bar{N}_i(\boldsymbol{\xi}). \end{aligned} \tag{E.2}$$

Note that, since E^I is straight-sided, $\boldsymbol{\phi}_I$ is an affine mapping with a constant Jacobian matrix.

Finally, the mapping between the ideal and physical elements can be written as:

$$\begin{aligned} \boldsymbol{\phi}_E : E^I \subset \mathbb{R}^3 &\longrightarrow E^P \subset \mathbb{R}^3 \\ \mathbf{y} &\longmapsto \mathbf{x} = \boldsymbol{\phi}_E(\mathbf{y}) = \boldsymbol{\phi}_P \circ \boldsymbol{\phi}_I^{-1}(\mathbf{y}) \\ &= \sum_{i=1}^{n_p} \mathbf{x}_i \bar{N}_i(\boldsymbol{\phi}_I^{-1}(\mathbf{y})) = \sum_{i=1}^{n_p} \mathbf{x}_i N_i(\mathbf{y}). \end{aligned} \tag{E.3}$$

where $N_i(\mathbf{y}) := \bar{N}_i(\boldsymbol{\phi}_I^{-1}(\mathbf{y}))$, is an interpolative shape function of polynomial degree p on E^I, since $\boldsymbol{\phi}_I$ is an affine mapping.

Note that $\boldsymbol{\phi}_E(\mathbf{y})$ can be written as $\boldsymbol{\phi}_E(\mathbf{y}; \mathbf{x}_1, \ldots, \mathbf{x}_{n_p})$, since it also depends on the node coordinates $\mathbf{x}_1, \ldots, \mathbf{x}_{n_p}$. Moreover, the nodes on the surface can be expressed in terms of the parametric coordinates by means of the surface parameterization $\boldsymbol{\varphi}$, see Equation (5.1). Hence, for a surface element, the mapping $\boldsymbol{\phi}_E$ can also be expressed in terms of the parametric coordinates of the element nodes as

$$\boldsymbol{\phi}_E(\mathbf{y}; \mathbf{x}_1, \ldots, \mathbf{x}_{n_p}) = \boldsymbol{\phi}_E(\mathbf{y}; \boldsymbol{\varphi}(\mathbf{u}_1), \ldots, \boldsymbol{\varphi}(\mathbf{u}_{n_p})).$$

In this manner, for optimization purposes, the nodes can be moved on the parametric space keeping the physical location always on the surface. Specifically, the mapping between the ideal and physical elements can be rewritten as:

$$\begin{aligned} \boldsymbol{\phi}_E : E^I \subset \mathbb{R}^3 &\longrightarrow E^P \subset \mathbb{R}^3 \\ \mathbf{y} &\longmapsto \mathbf{x} = \sum_{i=1}^{n_p} \boldsymbol{\varphi}(\mathbf{u}_i) N_i(\mathbf{y}), \end{aligned} \tag{E.4}$$

It is important to point out that $\boldsymbol{\phi}_E$ is in $\boldsymbol{\mathcal{W}}_{\boldsymbol{E^I}}$, see Equation (5.9). Specifically, we express ϕ_h element-wise as $\phi_{h|E^P} = \boldsymbol{\phi}_E$. Hence, the polynomial mesh representation ϕ_h is in $\boldsymbol{\mathcal{W}}$.

Appendix F

Behavior of the distortion and quality measures for high-order elements on parameterized surfaces

---

In this section, we illustrate the behavior of the proposed quality measure for high-order surface elements, presented in Equation (5.26). We compute the high-order quality measure for elements on parameterized surfaces using two different Jacobian-based distortion measures: the shape and the Oddy algebraic distortion measures presented in Equations (3.2) and (3.3), respectively. Specifically, we apply two tests to a triangle of polynomial degree three, Figures F.1 and F.3, and two tests to a quadrilateral of polynomial degree three, Figures F.2 and F.4. In each test, we consider three different free nodes: a vertex node, an edge node, and a face node. We keep all the nodes fixed in an ideal configuration, and we move the free node on the parametric space of the surface. In each figure, we compute the quality of the high-order element for each location of the free node, and we color each point of the surface with respect to the quality of the element when the free node is on that location. Moreover, for each figure, we display with a black line the boundary of the feasible region of the selected node, and we color in white the ideal element configuration.

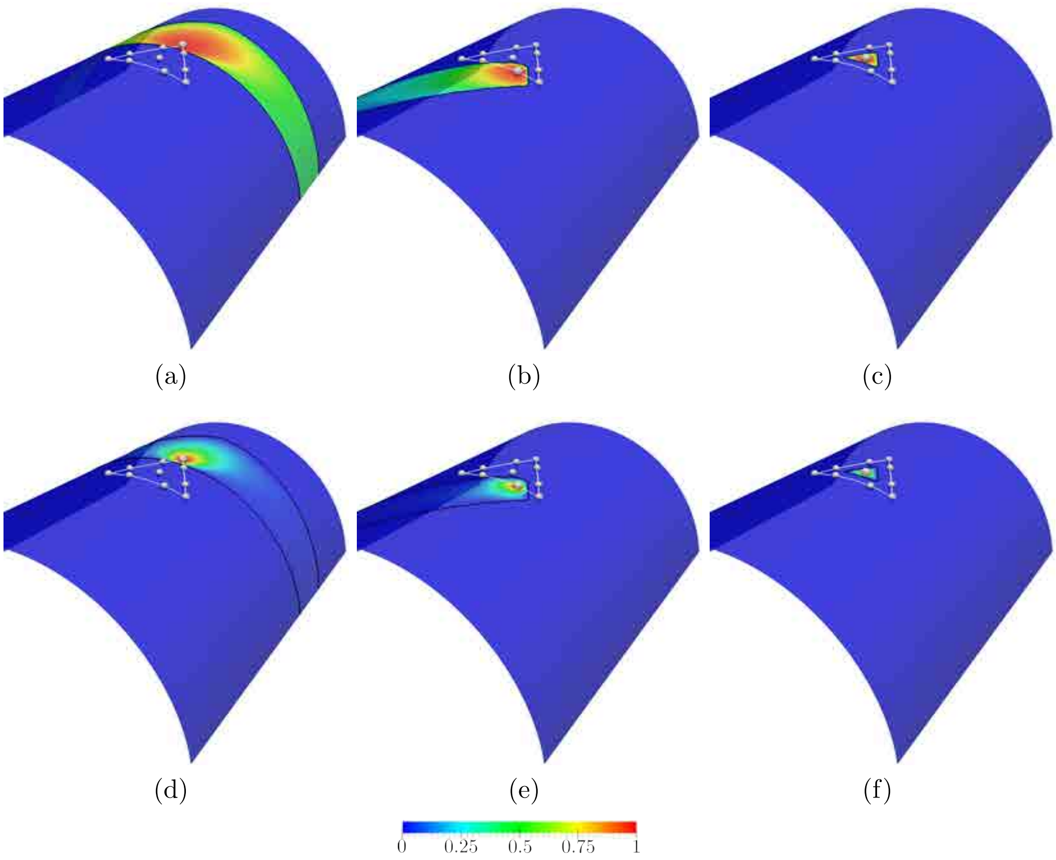

Figure F.1: Behavior of the quality measure for a high-order triangle of polynomial degree three on a cylinder. In columns, we select a different free node: (a,d) vertex, (b,e) edge, and (c,f) face. In rows, we change the Jacobian-based measure: (a-c) shape, and (d-f) Oddy.

First, we consider a triangle of interpolation degree three on a cylindrical surface. We select as ideal element the equilateral triangle, and we set a node distribution that provides a quasi-optimal Lebesgue constant (Warburton, 2006; Hesthaven and Warburton, 2007). Next, given each free node, we compute the quality of the surface element in terms of all the possible locations of the free node on the surface. In Figure F.1 we present the behavior of the quality measure. In columns, we present the behavior in terms of three different free nodes: a vertex node (first column), an edge node (second column) and a face node (third column). In rows, we present on the first row the shape distortion measure, whereas on the second row we present the Oddy distortion measure. We observe that both measures determine the same feasible region. Moreover, both quality measures detect the same ideal location, although the

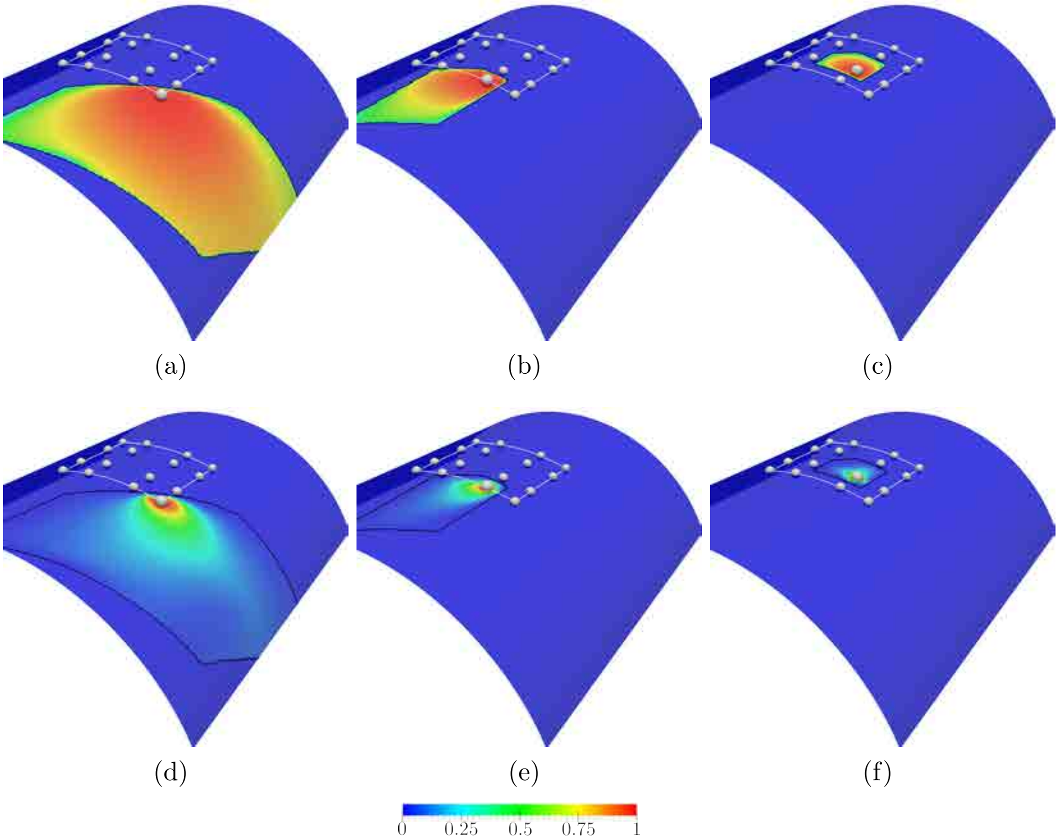

Figure F.2: Behavior of the quality measure for a high-order quadrilateral of polynomial degree three on a cylinder. In columns, we select a different free node: (a,d) vertex, (b,e) edge, and (c,f) face. In rows, we change the Jacobian-based measure: (a-c) shape, and (d-f) Oddy.

Oddy quality measure tends faster to zero.

Next, we change the function spaces in Equation (5.9) from triangles to quadrilaterals, and we extend the proposed measure to quadrilateral elements on surfaces. In addition, we consider a unit square as the ideal element with a node distribution obtained as the tensor product of a one-dimensional Legendre-Gauss-Lobatto node distribution. In Figure F.2 we present the behavior of the quality measure for a quadrilateral of polynomial degree three. Analogously to the triangle case, we observe that both measures detect the same feasible region and the same ideal configurations. Moreover, we observe that both quality measures are smooth functions that decrease as the node moves further from the ideal location.

Finally, in Figures F.3 and F.4 we present a high-order triangle and a high-order

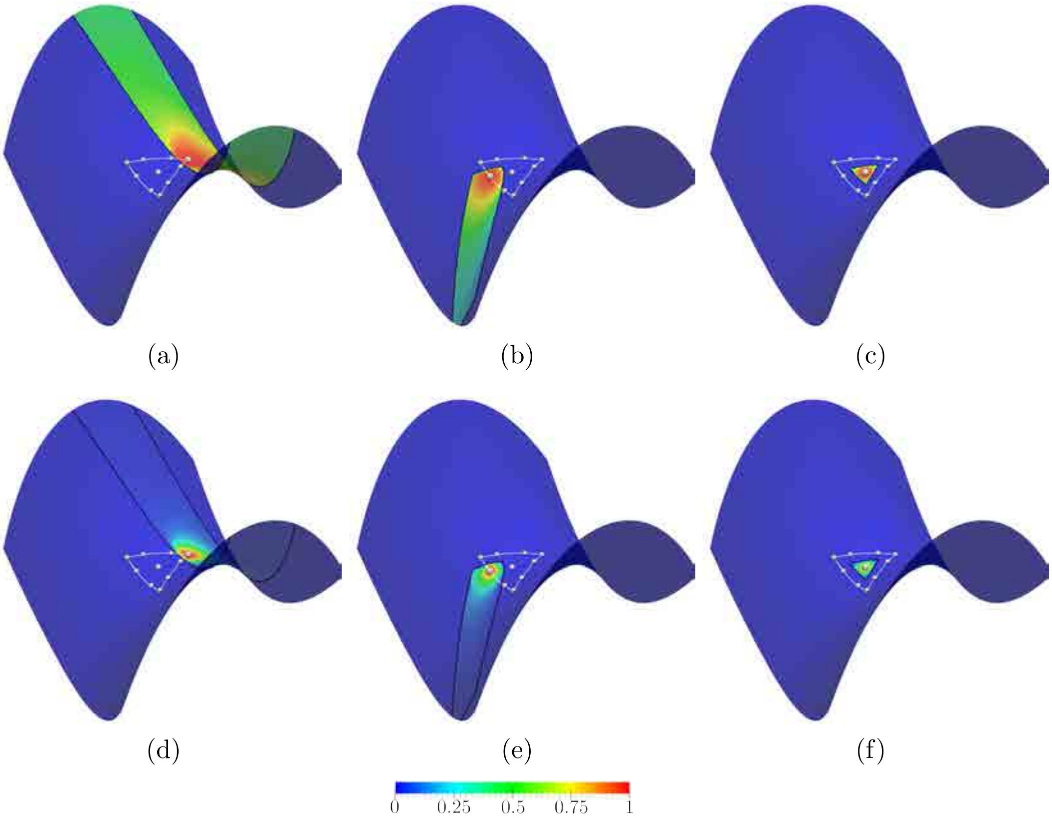

(a) (b) (c)

(d) (e) (f)

Figure F.3: Behavior of the quality measure for a high-order triangle of polynomial degree three on an hyperbolic paraboloid. In columns, we select a different free node: (a,d) vertex, (b,e) edge, and (c,f) face. In rows, we change the Jacobian-based measure: (a-c) shape, and (d-f) Oddy.

quadrilateral both of polynomial degree three on a hyperbolic paraboloid. Analogously to the cylinder case, we select an equilateral triangle as ideal for the triangle case, and a unit square for the quadrilateral case, and we set the corresponding node distribution. We observe that the behavior of the quality measure is similar to the cylinder case. In particular, we highlight that both the shape and Oddy quality measures detect the same feasible region and the same ideal configuration for both triangular and quadrilateral elements.

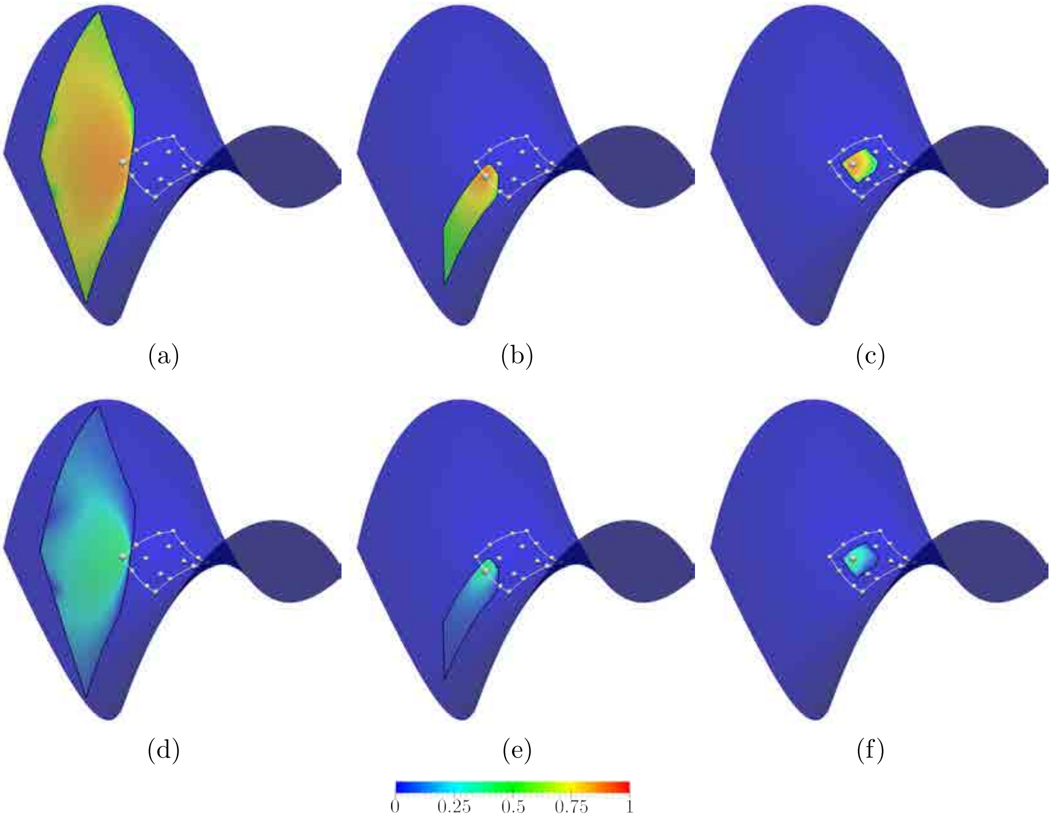
(a) (b) (c)

(d) (e) (f)

Figure F.4: Behavior of the quality measure for a high-order quadrilateral of polynomial degree three on an hyperbolic paraboloid. In columns, we select a different free node: (a,d) vertex, (b,e) edge, and (c,f) face. In rows, we change the Jacobian-based measure: (a-c) shape, and (d-f) Oddy.

Bibliography

Alliez, P., E. C. de Verdire, O. Devillers, and M. Isenburg (2003). Isotropic surface remeshing. In *Shape Modeling International, 2003*, pp. 49–58.

Alliez, P., G. Ucelli, C. Gotsman, and M. Attene (2005). Recent Advances in Remeshing of Surfaces. Technical report, EU network of excellence.

Baart, M. and E. Mulder (1987). A note on invertible two-dimensional quadratic finite element transformations. *Commun. Appl. Numer. M. 3*(6), 535–539.

Babuška, I. and B. Guo (1996). Approximation properties of the h-p version of the finite element method. *Comput. Meth. Appl. Mech. Engrg. 133*(3–4), 319 – 346.

Babuška, I. and B. Q. Guo (1988). The h-p version of the finite element method for domains with curved boundaries. *SIAM J. Num. Anal. 25*(4), 837–861.

Babuška, I., B. Szabo, and I. Katz (1981). The p-version of the finite element method. *SIAM J. Numer. Anal. 18*, 515–545.

Baker, T. J. (1987). Three dimensional mesh generation by triangulation of arbitrary point sets. In *8th Computational Fluid Dynamics Conference*, pp. 255–271.

Barth, T. J. (1998). *Simplified numerical methods for gas dynamics systems on triangulated domains.* Ph. D. thesis, Stanford University.

Bassi, F. and S. Rebay (1997). High-order accurate discontinuous finite element solution of the 2D Euler equations. *J. Comput. Phys. 138*(2), 251–285.

Branets, L. and G. Carey (2005). Extension of a mesh quality metric for elements with a curved boundary edge or surface. *J. Comput. Inf. Sci. Engrg. 5*(4), 302–308.

Cantwell, C., S. Sherwin, R. Kirby, and P. Kelly (2011a). From h to p efficiently: selecting the optimal spectral/hp discretisation in three dimensions. *Math. Model. Nat. Phenom. 6*(3), 84–96.

Cantwell, C., S. Sherwin, R. Kirby, and P. Kelly (2011b). From h to p efficiently: strategy selection for operator evaluation on hexahedral and tetrahedral elements. *Comput. Fluids 43*(1), 23–28.

CASCADE, O. (2012). Open CASCADE Technology, 3D modeling and numerical simulation. `www.opencascade.org`.

Clark, B., N. Ray, and X. Jiao (2013). Surface mesh optimization, adaption, and untangling with high-order accuracy. In X. Jiao and J.-C. Weill (Eds.), *Proc. 21st Int. Meshing Roundtable*, pp. 385–402. Springer Berlin Heidelberg.

Cockburn, B., B. Dong, J. Guzmán, M. Restelli, and R. Sacco (2009). A hybridizable discontinuous galerkin method for steady-state convection-diffusion-reaction problems. *SIAM J. Sci. Comput. 31*, 3827.

Cockburn, B. and C.-W. Shu (2002). Runge–kutta discontinuous galerkin methods for convection-dominated problems. *J. Sci. Comput. 16*(3), 173–261.

Deville, M. O., P. F. Fischer, and E. H. Mund (2002). *High-order methods for incompressible fluid flow*, Volume 9. Cambridge University Press.

Dey, S., R. O'Bara, and M. S. Shephard (2001a). Curvilinear mesh generation in 3D. *Computer-Aided Design 33*, 199–209.

Dey, S., R. O'Bara, and M. S. Shephard (2001b). Towards curvilinear meshing in 3D: the case of quadratic simplices. *Computer-Aided Design 33*(3), 199–209.

Dey, S., M. S. Shephard, and J. E. Flaherty (1997). Geometry representation issues associated with p-version finite element computations. *Comput. Meth. Appl. M. 150*(1–4), 39–55.

Escobar, J. M., R. Montenegro, E. Rodríguez, and G. Montero (2011). Simultaneous aligning and smoothing of surface triangulations. *Engrg. Comput. 27*(1), 17–29.

Escobar, J. M., G. Montero, R. Montenegro, and E. Rodríguez (2006). An algebraic method for smoothing surface triangulations on a local parametric space. *Int. J. Numer. Meth. Engrg. 66*(4), 740–760.

Escobar, J. M., E. Rodríguez, R. Montenegro, G. Montero, and J. M. González-Yuste (2003). Simultaneous untangling and smoothing of tetrahedral meshes. *Comput. Meth. Appl. Mech. Engrg. 192*(25), 2775–2787.

Field, D. (1983). Algorithms for determining invertible two-and three-dimensional quadratic isoparametric finite element transformations. *Int. J. Numer. Meth. Engrg. 19*(6), 789–802.

Field, D. (2000). Qualitative measures for initial meshes. *Int. J. Numer. Meth. Engrg. 47*(4), 887–906.

Freitag, L. A. and P. M. Knupp (2002). Tetrahedral mesh improvement via optimization of the element condition number. *Int. J. Numer. Meth. Engrg. 53*, 1377–1391.

Freitag, L. A. and P. Plassmann (2000). Local optimization-based simplicial mesh untangling and improvement. *Int. J. Numer. Meth. Engrg. 49*, 109–125.

Frey, P. J. and H. Borouchaki (1998). Geometric surface mesh optimization. *Comput. Visual. Sci. 1*(3), 113–121.

Gargallo-Peiró, A., X. Roca, J. Peraire, and J. Sarrate (2013a). Defining quality measures for mesh optimization on parameterized CAD surfaces. In *Proc. 21st Int. Meshing Roundtable*, pp. 85–102. Springer International Publishing.

Gargallo-Peiró, A., X. Roca, J. Peraire, and J. Sarrate (2013b). Inserting curved boundary layers for viscous flow simulation with high-order tetrahedra. In *Research Notes, 22nd Int. Meshing Roundtable.* Springer International Publishing.

Gargallo-Peiró, A., X. Roca, J. Peraire, and J. Sarrate (2014a). Defining quality measures for validation and generation of high-order tetrahedral meshes. In *Proc. 22nd Int. Meshing Roundtable*, pp. 109–126. Springer International Publishing.

Gargallo-Peiró, A., X. Roca, J. Peraire, and J. Sarrate (2014b). Distortion and quality measures for validating and generating high-order tetrahedral meshes. *Preprint*.

Gargallo-Peiró, A., X. Roca, J. Peraire, and J. Sarrate (2014c). Optimization of a regularized distortion measure to generate curved high-order unstructured tetrahedral meshes. *Preprint*.

Gargallo-Peiró, A., X. Roca, and J. Sarrate (2014). A surface mesh smoothing and untangling method independent of the CAD parameterization. *Comput. Mech. 53*(4), 587–609.

Garimella, R. and M. Shashkov (2004). Polygonal surface mesh optimization. *Engrg. Comput. 20*(3), 265–272.

Garimella, R., M. Shashkov, and P. M. Knupp (2004). Triangular and quadrilateral surface mesh quality optimization using local parametrization. *Comput. Meth. Appl. Mech. Engrg. 193*(9–11), 913–928.

George, P., F. Hecht, and E. Saltel (1988). Constraint of the boundary and automatic mesh generation. In *Numerical grid generation in computational fluid mechanics*, pp. 589–597.

George, P. L. and H. Borouchaki (2012). Construction of tetrahedral meshes of degree two. *Int J Numer Meth Eng 90*(9), 1156–1182.

Giorgiani, G., D. Modesto, S. Fernández-Méndez, and A. Huerta (2013). High-order continuous and discontinuous Galerkin methods for wave problems. *Int. J. Numer. Methods Fluids 73*(10), 883–903.

Hesthaven, J. and T. Warburton (2007). *Nodal Discontinuous Galerkin Methods: Algorithms, Analysis, and Applications.* Texts in Applied Mathematics. Springer.

Höllig, K., J. Hörner, and A. Hoffacker (2012). Finite element analysis with b-splines: Weighted and isogeometric meth. In *Curves and Surfaces*, Volume 6920 of *Lecture Notes in Computer Science*, pp. 330–350. Springer Berlin Heidelberg.

Huerta, A., A. Angeloski, X. Roca, and J. Peraire (2013). Efficiency of high-order elements for continuous and discontinuous Galerkin methods. *Int. J. Numer. Meth. Engrg. 96*, 529–560.

Huerta, A., G. Giorgiani, and D. Modesto (2011). Adaptive cdg and hdg computations. In *16th FEF.*

Huerta, A., X. Roca, A. Angeloski, and J. Peraire (2012). Are high-order and hybridizable discontinuous Galerkin methods competitive? *Oberwolfach Reports 9*(1), 485 – 487.

Hughes, T., J. Cottrell, and Y. Bazilevs (2005). Isogeometric analysis: CAD, finite elements, NURBS, exact geometry and mesh refinement. *Comput. Meth. Appl. Mech. Engrg. 194*(39–41), 4135 – 4195.

Jiao, X. and D. Wang (2012). Reconstructing high-order surfaces for meshing. *Engrg. Comput. 28*(4), 361–373.

Jiao, X., D. Wang, and H. Zha (2011). Simple and effective variational optimization of surface and volume triangulations. *Engrg. Comput. 27*, 81–94.

Johnen, A., J.-F. Remacle, and C. Geuzaine (2012). Geometrical validity of curvilinear finite elements. In *Proc. 20th Int. Meshing Roundtable*, pp. 255–271. Springer International Publishing.

Johnen, A., J.-F. Remacle, and C. Geuzaine (2013). Geometrical validity of curvilinear finite elements. *J. Comput. Phys. 233*, 359 – 372.

Karniadakis, G. and S. Sherwin (2013). *Spectral/hp element methods for computational fluid dynamics.* Oxford University Press.

Kirby, R., S. Sherwin, and B. Cockburn (2012). To CG or to HDG: a comparative study. *J. Sci. Comput. 51*(1), 183–212.

Knupp, P. M. (2001a). Algebraic mesh quality metrics. *SIAM J. Numer. Anal. 23*(1), 193–218.

Knupp, P. M. (2001b). Hexahedral and tetrahedral mesh untangling. *Engrg. Comput. 17*(3), 261–268.

Knupp, P. M. (2003a). Algebraic mesh quality metrics for unstructured initial meshes. *Finite Elem. Anal. Des. 39*(3), 217–241.

Knupp, P. M. (2003b). A method for hexahedral mesh shape optimization. *Int. J. Numer. Meth. Engrg. 58*(2), 319–332.

Knupp, P. M. (2009). Label-invariant mesh quality metrics. In *Proc. 18th Int. Meshing Roundtable*, pp. 139–155. Salt Lake City: Springer Berlin Heidelberg.

Leng, J., Y. Zhang, and G. Xu (2012). A novel geometric flow-driven approach for quality improvement of segmented tetrahedral meshes. In *Proc. 20th Int. Meshing Roundtable*, pp. 347–364. Springer Berlin Heidelberg.

Löhner, R. (2011). Error and work estimates for high-order elements. *Int. J. Numer. Meth. Fluids 67*(12), 2184–2188.

Löhner, R. (2013). Improved error and work estimates for high-order elements. *Int. J. Numer. Meth. Fluids 72*, 1207–1218.

Löhner, R., K. Morgan, J. Peraire, and O. C. Zienkiewicz (1985). Finite element methods for high speed flows. In *7th Computational Fluid Dynamics Conference*, pp. 403–410.

Löhner, R. and P. Parikh (1988). Generation of three-dimensional unstructured grids by the advancing-front method. *Int. J. Numer. Meth. Fluids 8*(10), 1135–1149.

López, E. J., N. M. Nigro, and M. A. Storti (2008). Simultaneous untangling and smoothing of moving grids. *Int. J. Numer. Meth. Engrg. 76*(7), 994–1019.

Luo, X. (2005). *An automatic adaptive directional variable p-version method in 3D curved domains.* Ph. D. thesis, Rensselaer Polytechnic Institute.

Luo, X., M. S. Shephard, R. O'Bara, R. Nastasia, and M. Beall (2004). Automatic p-version mesh generation for curved domains. *Engrg. Comput. 20*(3), 273–285.

Luo, X., M. S. Shephard, and J.-F. Remacle (2002). The influence of geometric approximation on the accuracy of higher order methods. In *8th Int. Conf. Numerical Grid Generation in Computational Field Simulations.*

Luo, X., M. S. Shephard, J.-F. Remacle, R. O'Bara, M. Beall, B. Szabó, and R. Actis (2002). P-version mesh generation issues. In *Proc. 11th Int. Meshing Roundtable*, pp. 343–354. Springer Berlin Heidelberg.

Mitchell, A., G. Phillips, and E. Wachspress (1971). Forbidden shapes in the finite element method. *IMA J. Appl. Math. 8*(2), 260.

Mullen, P., Y. Tong, P. Alliez, and M. Desbrun (2008). Spectral Conformal Parameterization. *Comput. Graph. Forum 27*(5), 1487–1494.

Nguyen, N., J. Peraire, and B. Cockburn (2009a). An implicit high-order hybridizable discontinuous Galerkin method for linear convection-diffusion equations. *J. Comput. Phys. 228*, 3232–3254.

Nguyen, N., J. Peraire, and B. Cockburn (2009b). An implicit high-order hybridizable discontinuous Galerkin method for nonlinear convection-diffusion equations. *J. Comput. Phys. 228*, 8841–8855.

Nielsen, E. J. and W. K. Anderson (2002). Recent improvements in aerodynamic design optimization on unstructured meshes. *AIAA journal 40*(6), 1155–1163.

Nocedal, J. and S. Wright (1999). *Numerical optimization.* Springer verlag.

Oddy, A., J. Goldak, M. McDill, and M. Bibby (1988). A distortion metric for isoparametric elements. *Trans. Canad. Soc. Mech. Engrg. 12*, 213–217.

Oliver, T. (2008). *A high-order, adaptive, discontinuous Galerkin finite element method for the Reynolds-Averaged Navier-Stokes equations.* Ph. D. thesis, Massachusetts Institute of Technology.

Peraire, J., N. Nguyen, and B. Cockburn (2010). A hybridizable discontinuous Galerkin method for the compressible Euler and Navier-Stokes equations. In *Proceedings of the 48th AIAA Aerospace Sciences Meeting and Exhibit*, pp. AIAA Paper 2010–363.

Peraire, J., J. Peiro, L. Formaggia, K. Morgan, and O. C. Zienkiewicz (1988). Finite element euler computations in three dimensions. *Int. J. Numer. Meth. Engrg. 26*(10), 2135–2159.

Peraire, J., M. Vahdati, K. Morgan, and O. C. Zienkiewicz (1987). Adaptive remeshing for compressible flow computations. *J. Comp. Physics 72*(2), 449–466.

Persson, P.-O. and J. Peraire (2009). Curved mesh generation and mesh refinement using lagrangian solid mechanics. In *Proc. 47th AIAA*.

Remacle, J.-F., T. Toulorge, and J. Lambrechts (2013). Robust untangling of curvilinear meshes. In *Proc. 21st Int. Meshing Roundtable*, pp. 71–83. Springer International Publishing.

Roca, X. (2009). *Paving the path towards automatic hexahedral mesh generation.* Ph. D. thesis, Universitat Politècnica de Catalunya.

Roca, X., A. Gargallo-Peiró, and J. Sarrate (2012). Defining quality measures for high-order planar triangles and curved mesh generation. In *Proc. 20th Int. Meshing Roundtable*, pp. 365–383. Springer International Publishing.

Roca, X., N. Nguyen, and J. Peraire (2013). Scalable parallelization of the hybridized discontinuous Galerkin method for compressible flow. In *43rd AIAA Fluid Dynamics Conference and Exhibit*.

Roca, X., E. Ruiz-Gironés, and J. Sarrate (2010). EZ4U: Mesh generation environment. `www-lacan.upc.edu/ez4u.htm`.

Roca, X., J. Sarrate, and A. Huerta (2004). Surface mesh projection for hexahedral mesh generation by sweeping. In *Proc. 13th Int. Meshing Roundtable*, pp. 169–179. Springer Berlin Heidelberg.

Roca, X., J. Sarrate, and A. Huerta (2006). Mesh projection between parametric surfaces. *Commun. Numer. Met. Engrg. 22*(6), 591–603.

Roca, X., J. Sarrate, and E. Ruiz-Gironés (2007). A graphical modeling and mesh generation environment for simulations based on boundary representation data. In *Communications in Num. Meth. Engrg.*, Porto.

Ruiz-Gironés, E. (2011). *Automatic Hexahedral Meshing Algorithms: From Structured to Unstructured Meshes*. Ph. D. thesis, Universitat Politècnica de Catalunya.

Ruiz-Gironés, E. and J. Sarrate (2010). Generation of structured hexahedral meshes in volumes with holes. *Finite Elem. Anal. Des. 46*(10), 792–804.

Sahni, O., X. Luo, K. Jansen, and M. Shephard (2010). Curved boundary layer meshing for adaptive viscous flow simulations. *Finite Elem. Anal. Des. 46*(1), 132–139.

Salem, A., S. Canann, and S. Saigal (1997). Robust distortion metric for quadratic triangular 2D finite elements. *Appl. Mech. Div. ASME. 220*, 73–80.

Salem, A., S. Canann, and S. Saigal (2001). Mid-node admissible spaces for quadratic triangular arbitrarily curved 2D finite elements. *Int. J. Numer. Meth. Engrg. 50*(2), 253–272.

Salem, A., S. Saigal, and S. Canann (2001). Mid-node admissible space for 3D quadratic tetrahedral finite elements. *Engrg. Comput. 17*(1), 39–54.

Sastry, S., S. Shontz, and S. Vavasis (2012a). A log-barrier method for mesh quality improvement. In *Proc. 20th Int. Meshing Roundtable*, pp. 329–346. Springer International Publishing.

Sastry, S., S. Shontz, and S. Vavasis (2012b). A log-barrier method for mesh quality improvement and untangling. *Engrg. Comput.*.

Schwab, C. (1998). *p-and hp-finite element methods: Theory and applications in solid and fluid mechanics*. Clarendon Press Oxford.

Sevilla, R., S. Fernández-Méndez, and A. Huerta (2011). NURBS–Enhanced Finite Element Method (NEFEM): a seamless bridge between CAD and FEM. *Arch. Comput. Meth. Engrg. 18*(4), 441–484.

Shephard, M. and M. Georges (1991). Automatic three-dimensional mesh generation by the finite octree technique. *Int. J. Numer. Meth. Engrg. 32*(4), 709–749.

Shephard, M. S., J. E. Flaherty, K. Jansen, X. Li, X. Luo, N. Chevaugeon, J.-F. Remacle, M. Beall, and R. O'Bara (2005). Adaptive mesh generation for curved domains. *Appl. Numer. Math. 52*(2-3), 251–271.

Sherwin, S. and J. Peiró (2002). Mesh generation in curvilinear domains using high-order elements. *Int. J. Numer. Meth. Engrg. 53*(1), 207–223.

Shewchuk, J. (2002). What is a good linear finite element? interpolation, conditioning, anisotropy, and quality measures (preprint). *Preprint*.

Shivanna, K., N. Grosland, and V. Magnotta (2010). An analytical framework for quadrilateral surface mesh improvement with an underlying triangulated surface definition. In *Proc. 19th Int. Meshing Roundtable*, pp. 85–102. Chattanooga: Springer Berlin Heidelberg.

Szabo, B. and I. Babuška (1991). *Finite Element Analysis.* John Wiley & Sons New York.

Toulorge, T., C. Geuzaine, J.-F. Remacle, and J. Lambrechts (2013). Robust untangling of curvilinear meshes. *J. Comput. Phys. 254*, 8 – 26.

Vartziotis, D., T. Athanasiadis, I. Goudas, and J. Wipper (2008). Mesh smoothing using the geometric element transformation method. *Comput. Meth. Appl. Mech. Engrg. 197*, 3760–3767.

Vos, P. E., S. Sherwin, and R. Kirby (2010). From h to p efficiently: implementing finite and spectral/*hp* element methods to achieve optimal performance for low- and high-order discretisations. *J. Comput. Phys. 229*(13), 5161–5181.

Wang, Z., K. Fidkowski, R. Abgrall, F. Bassi, D. Caraeni, A. Cary, H. Deconinck, R. Hartmann, K. Hillewaert, H. Huynh, et al. (2013). High-order cfd methods: current status and perspective. *Int. J. Numer. Meth. Fluids 72*(8), 811–845.

Warburton, T. (2006). An explicit construction of interpolation nodes on the simplex. *J. Engrg. Math. 56*(3), 247–262.

Xie, Z., R. Sevilla, O. Hassan, and K. Morgan (2012). The generation of arbitrary order curved meshes for 3D finite element analysis. *Comput. Mech. 51*, 361–374.

Xue, D. and L. Demkowicz (2005). Control of geometry induced error in *hp* finite element (FE) simulations. I. Evaluation of FE error for curvilinear geometries. *Internat. J. Numer. Anal. Model. 2*(3), 283–300.

Yano, M. et al. (2012). *An optimization framework for adaptive higher-order discretizations of partial differential equations on anisotropic simplex meshes.* Ph. D. thesis, Massachusetts Institute of Technology.

Yerry, M. and M. Shephard (1984). Automatic three-dimensional mesh generation by the modified-octree technique. *Int. J. Numer. Meth. Engrg. 20*(11), 1965–1990.

Yuan, K., Y. Huang, and T. Pian (1994). Inverse mapping and distortion measures for quadrilaterals with curved boundaries. *Int. J. Numer. Meth. Engrg. 37*(5), 861–875.

Zhang, Y., C. Bajaj, and G. Xu (2009). Surface smoothing and quality improvement of quadrilateral/hexahedral meshes with geometric flow. *Communications in Numerical Meth. in Engrg. 25*(1), 1–18.